



UFZ Centre for Environmental Research
Leipzig-Halle
in the Helmholtz-Association

PhD Dissertation 08/2006

Direct Oxygen Injection Experiments and Investigation of Multi-Component Mass Transfer Processes

Annika Beckmann

ISSN 1860-0387

**Direct Oxygen Injection Experiments and Investigation
of Multi-Component Mass Transfer Processes**

Von der Fakultät für Geowissenschaften, Geotechnik und Bergbau
der Technischen Universität Bergakademie Freiberg

genehmigte

DISSERTATION

zur Erlangung des akademischen Grades

Doctor rerum naturalium

Dr. rer. nat.,

vorgelegt

von Dipl.-Geol. Annika Beckmann

geboren am 14.01.1974 in Walsrode

Gutachter: Prof. Dr. Broder J. Merkel, Freiberg
Prof. Dr. Helmut Geistlinger, Halle
Prof. Dr. Kevin W. Biggar, Edmonton (Kanada)

Tag der Verleihung: 17.03.2006

“The greatest obstacle to discovery is not ignorance - it is the illusion of knowledge.”

Daniel J. Boorstin

Abstract

The aim of this thesis was to investigate the impact of a direct oxygen injection as a potential remediation strategy for contaminated aquifers on a bench scale. The mass transfer between a multi-component trapped gas phase and a mobile water phase was studied. Column experiments with dynamically compressed sediments and a direct gas injection of pure oxygen gas were performed. In addition, a new developed kinetic multi-component model was used to describe the experiments.

The amount of gas that could be captured in the pore space during direct oxygen injection and the time needed for a complete dissolution of the trapped gas phase were determined. Varying influences of different gases already dissolved in the mobile water phase on the dissolution process of a trapped oxygen gas phase were described for different flow regimes and confirmed by the model results. Finally, on the basis of the experimental and model results obtained in this thesis, predictions for an application of a direct oxygen injection in the field were discussed.

Zusammenfassung

Ziel dieser Arbeit war die Untersuchung im Labormaßstab von Auswirkungen einer direkten Sauerstoffgasinjektion als mögliche Sanierungsstrategie für kontaminierte Grundwasserleiter. Darüber hinaus wurde der Massentransfer zwischen einer residualen Mehrkomponenten-Gasphase und der mobilen Wasserphase untersucht. Hierfür wurden in Säulenexperimenten mit dynamisch eingespannten Sedimenten direkte Gasinjektionen mit reinem Sauerstoff durchgeführt. Zusätzlich wurde ein neu entwickeltes kinetisches Mehrkomponenten-Modell zur Beschreibung der experimentellen Ergebnisse verwendet.

Das Gasvolumen, welches bei einer direkten Sauerstoffgasinjektion im Porenraum zurückgehalten werden konnte, sowie die benötigte Zeitdauer für die vollständige Auflösung der Gasphase wurden bestimmt. Zudem wurde ein unterschiedlicher Einfluss von bereits in der mobilen Wasserphase gelösten Gasen auf den Auflösungsprozess einer residualen Sauerstoff-Gasphase unter verschiedenen Fließbedingungen festgestellt und durch die Modellergebnisse bestätigt. Schließlich wurden mögliche Voraussagen für die Anwendung einer direkten Sauerstoffgasinjektion im Feld basierend auf den Ergebnissen dieser Arbeit diskutiert.

Table of Contents

List of Figures	III
List of Tables.....	VIII
List of Symbols	IX
1. Introduction	1
2. Direct Oxygen Injection	5
2.1 Overview on In Situ Remediation Strategies to Increase the Dissolved Oxygen Concentration.....	5
2.2 Basic Mechanisms Influencing Gas Trapping and Achievable Gas Saturation	9
2.3 Mass Transfer between Gas and Water Phase	14
2.4 Hydraulic Conductivity.....	16
3. Conceptual Models.....	17
3.1 Modeling of Mass Transfer between Gas and Water Phase	17
3.1.1 Equilibrium Approach.....	17
3.1.2 Kinetic Approach	19
3.1.2.1 Estimates for the Effective Gas-Water Interface.....	20
3.1.2.2 Conceptual Models of the Mass Transfer Coefficient	22
3.2 Transport of Dissolved Gases and Contaminants.....	26
3.3 Comparison of Different Kinetic Models used for Inverse Modeling.....	29
4. Laboratory Experiments	33
4.1 Design of the Laboratory Column.....	34
4.1.1 Dimension of the Column and Sand Properties	34
4.1.2 Dynamical Compression of the Sediment	35
4.2 Experimental Setup	37
4.3 Measurement and Control Technology	39
4.3.1 Gravimetric Measurements	39
4.3.2 Oxygen Measurements	42
4.3.3 Hydraulic Conductivity Measurements.....	44
4.3.4 Bromide Measurements and Bromide Tracer Tests.....	45
4.3.5 Peristaltic Pump.....	47
4.3.6 Data Acquisition.....	47
4.4 Experimental Procedure.....	49

5. Experimental Results.....	51
5.1 Test Series 1: Influence of Different Dissolved Gases on the Dissolution of a Trapped Oxygen Gas Phase	51
5.1.1 Helium as Flushing Gas	51
5.1.2 Nitrogen as Flushing Gas	56
5.1.3 Argon as Flushing Gas	62
5.2 Test Series 2: Velocity Modifications.....	67
5.2.1 Experiments at a Water Flow Velocity of 9 m/d.....	67
5.2.2 Experiments at a Water Flow Velocity of 4 m/d.....	73
5.3 Discussion of the Experimental Results	78
6. Model Results.....	88
6.1 Sensitivity Analysis.....	88
6.2 Comparison of Measured Data and Model Results.....	90
6.3 Discussion of the Model Results	92
6.4 Additional Model Calculations.....	94
7. Summary and Conclusions.....	100
8. Outlook.....	104
References	108
Acknowledgement.....	119
Appendix	120
Lebenslauf.....	A
Versicherung.....	B

List of Figures

FIGURE 1: Conceptual model of an oxygen bubble wall: a) macro and b) micro scale. The red dots symbolize the oxygen bubbles; the blue arrows denote the water flow direction (after Fry et al., 1997).	8
FIGURE 2: Interfacial tensions between a solid surface S, a wetting fluid L, and a non-wetting fluid G (after Fetter, 1993).	9
FIGURE 3: a) Pressure distribution in a gas filled capillary. b) Trapped gas bubbles after the injection pulse.	12
FIGURE 4: Balance of forces acting on a gas bubble (after Weber, 2000).	13
FIGURE 5: Conceptual model: Dissolution of the gas bubble.	15
FIGURE 6: Stagnant film model (after Cussler, 1997).	23
FIGURE 7: Conceptual sketches of surface renewal on the water side of the inter-face (above) and of the film thickness at one location over time (below) as assumed by the surface renewal theory (after Gulliver, 1990).	24
FIGURE 8: Velocity dependency of the mass transfer coefficient for different gases according to the empirical Sherwood correlation (Equ. 33 and 34).	25
FIGURE 9: Van Genuchten parameterization of the relative permeability (Equation 44). Thick solid line: Fit to own experiments 1, 3, and 7 (van Genuchten parameter $n = 3.43$); thin solid line: Fit to the experimental values from Fry et al. (1996) ($n = 12$), DGI = direct gas injection, SSH ₂ O = injection of supersaturated water, H ₂ O ₂ = injection of hydrogen peroxide solution; dashed line: Typical sand after Carsel & Parrish (1988) ($n = 2.68$) (after Geistlinger et al., 2005).	28
FIGURE 10: Comparison of the CVM- and VVM-elution curves for the dissolution of a trapped oxygen gas phase (after Geistlinger et al., 2005).	30
FIGURE 11: Channelling that has arisen in uncompressed sediments during direct gas injection.	36
FIGURE 12: Schematic construction of the column. An axial compression is applied on the column ends through a clamping device.	37
FIGURE 13: Experimental set up. The gravimetric measuring system contains three balances: One inflow-balance and two outflow-balances. A phase blender regulates a specified gas-water flow. The column is dynamically compressed through a clamping device. The inflow column cap contains a bromide sensor and a	

pressure transducer. The outflow column cap additionally contains an oxygen sensor.	38
FIGURE 14: Sand-filled, dynamically compressed symmetrical column (left), computer based data recording in the outlet of the column (right).	39
FIGURE 15: Gas volume in the column calculated from gravimetric measurements versus time shown for experiment 5 a) before corrections b) after corrections of the linear drift between the balances.....	41
FIGURE 16: Flow-through cell with integrated oxygen sensor (optode).....	42
FIGURE 17: Installation of the bromide electrodes in the column cap.	45
FIGURE 18: Automated parameter estimation: Exemplary bromide breakthrough curve. Black line: Experimental bromide tracer curve; red line: Analytical Dirac solution.....	46
FIGURE 19: Graphical user interface with digital readouts (DasyLab 6.0).....	48
FIGURE 20: Procedure of the gas injection. The experiment started by the injection of oxygen gas at the bottom of the column. The gas injection was stopped when a first steady-state flow condition was reached. The gas volume in the column decreased until a second steady-state flow condition was established and the column feed was switched to the low oxygen solution (start of the dissolution of the trapped oxygen gas phase).	50
FIGURE 21: Gas volume in the column determined by gravimetric measurements before the start of the dissolution experiment for a) experiment 1 and b) experiment 2. The water flow rate for experiment 1 was 1.58 cm ³ /min and the gas flow rate was 0.64 cm ³ /min. For experiment 2 a water flow rate of 1.59 cm ³ /min was applied and a gas flow rate of 0.92 cm ³ /min. In both experiments helium was used as flushing gas. For both experiments no bromide tracer test was conducted during the second steady-state flow condition.	53
FIGURE 22: Dissolved oxygen concentration versus saturated pore volumes recorded at the column outlet during the dissolution of the injected oxygen gas phase for experiment 1 (dark blue triangles) and 2 (yellow squares). The water flow velocity determined from the gravimetric measurements was 16.7 m/d for experiment 1 and 16.9 m/d for experiment 2. In both experiments helium was used as flushing gas.....	54
FIGURE 23: Normalized hydraulic conductivity plotted versus the saturated pore volumes for experiment 1 (dark blue triangles) and 2 (yellow squares) (helium used as flushing gas).....	55

- FIGURE 24: Longitudinal dispersivity, effective porosity and corresponding gas saturation determined by bromide tracer test during dissolution experiment 1 (dark blue triangles) and 2 (yellow squares). Helium was used as flushing gas. 56
- FIGURE 25: Gas volume in the column determined by gravimetric measurements before the start of the dissolution experiment for a) experiment 3 and b) experiment 4. The water flow rate for experiment 3 was $1.56 \text{ cm}^3/\text{min}$ and the gas flow rate was $0.80 \text{ cm}^3/\text{min}$. For experiment 4 a water flow rate of $1.64 \text{ cm}^3/\text{min}$ was applied and a gas flow rate of $0.54 \text{ cm}^3/\text{min}$. In both experiments nitrogen was used as flushing gas. For experiment 3 a bromide tracer test was conducted at the second steady-state flow condition. 58
- FIGURE 26: Dissolved oxygen concentration recorded at the column outlet versus saturated pore volumes for experiment 3 (orange squares) and 4 (light green triangles). The water flow velocity determined from the gravimetric measurements was 16.6 m/d for experiment 3 and 17.4 m/d for experiment 4. In both experiments nitrogen was used as flushing gas. 59
- FIGURE 27: Normalized hydraulic conductivity plotted versus the saturated pore volumes for experiment 3 (orange squares) and 4 (light green triangles) (nitrogen used as flushing gas). 60
- FIGURE 28: Longitudinal dispersivity, effective porosity and corresponding gas saturation determined by bromide tracer test during dissolution experiment 3 (orange squares) and 4 (light green triangles). For both experiments nitrogen was used as flushing gas. 61
- FIGURE 29: Gas volume in the column determined by gravimetric measurements before the start of the dissolution experiment for a) experiment 5 and b) experiment 6. The water flow rate for experiment 5 was $1.58 \text{ cm}^3/\text{min}$ and the gas flow rate was $1.30 \text{ cm}^3/\text{min}$. For experiment 6 a water flow rate of $1.54 \text{ cm}^3/\text{min}$ was applied and a gas flow rate of $1.50 \text{ cm}^3/\text{min}$. In both experiments argon was used as flushing gas and a bromide tracer test was conducted at the second steady-state condition. 62
- FIGURE 30: Dissolved oxygen concentration versus saturated pore volumes recorded at the column outlet during the dissolution of the injected oxygen gas phase for experiment 5 (light blue dots) and 6 (purple triangles). The water flow velocity determined from the gravimetric measurements was 16.9 m/d for experiment 5 and 16.4 m/d for experiment 6. In both experiments argon was used as flushing gas. 64
- FIGURE 31: Normalized hydraulic conductivity plotted versus the saturated pore volumes for experiment 5 (light blue dots) and 6 (purple triangles) (argon used as flushing gas). 65
- FIGURE 32: Longitudinal dispersivity, effective porosity and corresponding gas saturation determined by bromide tracer test during dissolution experiment 5 (light blue dots) and 6 (purple triangles). Argon was used as flushing gas. 66

- FIGURE 33: Gas volume in the column determined by gravimetric measurements before the start of the dissolution experiment for a) experiment 7 and b) experiment 8. The water flow rate for experiments 7 and 8 was $0.8 \text{ cm}^3/\text{min}$. The gas flow rate for experiment 7 was $0.37 \text{ cm}^3/\text{min}$ and for experiment 8 $0.41 \text{ cm}^3/\text{min}$. In both experiments nitrogen was used as flushing gas and a bromide tracer test was conducted at the second steady-state condition. 69
- FIGURE 34: Dissolved oxygen concentration recorded at the column outlet versus saturated pore volumes for experiment 7 (red triangles) and 8 (green hexagons). The water flow velocity determined from the gravimetric measurements was 8.5 m/d for both experiments. Nitrogen was used as flushing gas. 70
- FIGURE 35: Trend of the normalized hydraulic conductivity plotted versus the saturated pore volumes for experiment 7 (red triangles) and 8 (green hexagons). For both experiments nitrogen was used as flushing gas. 71
- FIGURE 36: Longitudinal dispersivity, effective porosity and corresponding gas saturation determined by bromide tracer test during dissolution experiment 7 (red triangles) and 8 (green hexagons). Nitrogen was used as flushing gas..... 72
- FIGURE 37: Gas volume in the column determined by gravimetric measurements before the start of the dissolution experiment for a) experiment 9 and b) experiment 10. The water flow rate for experiment 9 was $0.40 \text{ cm}^3/\text{min}$ and the gas flow rate was $0.11 \text{ cm}^3/\text{min}$. For experiment 10 a water flow rate of $0.41 \text{ cm}^3/\text{min}$ was applied and a gas flow rate of $0.20 \text{ cm}^3/\text{min}$. In both experiments nitrogen was used as flushing gas and a bromide tracer test was conducted at the second steady-state condition..... 73
- FIGURE 38: Dissolved oxygen concentration versus saturated pore volumes recorded at the column outlet during the dissolution of the injected oxygen gas phase for experiment 9 (brown pentagons) and 10 (lilac stars). The water flow velocity determined from the gravimetric measurements was 4.2 m/d for experiment 9 and 4.3 m/d for experiment 10. In both experiments nitrogen was used as flushing gas. 76
- FIGURE 39: Longitudinal dispersivity, effective porosity and corresponding gas saturation determined by bromide tracer test during dissolution experiment 9 (brown pentagons) and 10 (lilac stars). Nitrogen was used as flushing gas..... 77
- FIGURE 40: Effluent dissolved oxygen concentration curves for the experiments performed with nitrogen as flushing gas (water flow velocities are given in the legend)... 80
- FIGURE 41: Effluent dissolved oxygen concentration versus saturated pore volumes for experiment 1 (dark blue triangles), experiment 4 (light green triangles) and experiment 5 (light blue dots) (flushing gases used to produce the low oxygen solution are given in the legend)..... 81
- FIGURE 42: Normalized hydraulic conductivity versus saturated pore volumes for experiment 1 (dark blue triangles), experiment 4 (light green triangles) and

experiment 5 (light blue dots) (flushing gases used to produce the low oxygen solution are given in the legend). The water flow velocity determined from the gravimetric measurements was 17 m/d for all three experiments.....	84
FIGURE 43: Sensitivity analysis for the oxygen concentration curve considering experiment 3 as example. The varied parameters are given in the legend. Besides the dissolved oxygen curves where S_g (dashed red and dark blue line), q_w (thin orange and green line) and r_b (grey and purple lines) was varied, all other curves overlay the dissolved oxygen curve calculated with the mean values (thick black line).	89
FIGURE 44: Comparison between experimental data (data points), kinetic theory (thick red line) and local equilibrium theory (thin black line). a) Experiment 1 (helium as flushing gas, water flow velocity: 17 m/d), b) experiment 4 (nitrogen as flushing gas, water flow velocity: 17 m/d), c) experiment 5 (argon as flushing gas, water flow velocity: 17 m/d), d) experiment 7 (nitrogen as flushing gas, water flow velocity: 9 m/d), e) experiment 10 (nitrogen as flushing gas, water flow velocity: 4 m/d).	91
FIGURE 45: Gas saturation within the column at time $t = 0.1$ days (exchange of 1.82 pore volumes) predicted by the VVM for different flushing gases. The initial gas saturation of 0.08 is illustrated through the thin horizontal line.	96
FIGURE 46: Gas saturation within the column at time $t = 0.2$ days (exchange of 3.64 pore volumes) predicted by the VVM for different flushing gases. The initial gas saturation of 0.08 is illustrated through the thin horizontal line.	97
FIGURE 47: Dissolution of a gas bubble near the column inlet ($L = 0.1$ m) predicted by the VVM: Bubble radius versus time for three different two-component gas phases.	98
FIGURE 48: Principle of controlled direct gas injection (lateral view).	105

List of Tables

TABLE 1: Achievable dissolved oxygen concentration range and estimated cost of oxygen \$/Pound (from Fields et al., 2002).....	6
TABLE 2: Significance of dimensionless numbers for typical groundwater conditions: $u = 1 - 10$ m/d and bubble diameter $d_b = 0.1 - 1.0$ mm (after Cussler, 1997).....	26
TABLE 3: Summary of the dissolution experiments.	33
TABLE 4: Relevant parameter of the sediment-filled column generally applicable to all experiments.	35
TABLE 5: Parameters and results of experiments 1 and 2 (helium as flushing gas).....	52
TABLE 6: Parameters and results of experiments 3 and 4 (nitrogen as flushing gas).....	57
TABLE 7: Parameters and results of experiments 5 and 6 (argon as flushing gas).....	63
TABLE 8: Parameters and results of experiments 7 and 8 (nitrogen as flushing gas).....	68
TABLE 9: Parameters and results of experiments 9 and 10 (nitrogen as flushing gas).....	74
TABLE 10: Summary of parameters and results for all experiments.	78
TABLE 11: Physico-chemical properties for oxygen and flushing gases.	82
TABLE 12: Experimental fitting parameters and theoretical parameters derived by inverse modeling.	90
TABLE 13: Parameter set for theoretical calculations with the kinetic model.....	95

List of Symbols

(the index i for a component is omitted in this list)

A_b	surface of a single bubble
A_b^m	surface area of a single bubble of class m
A_{col}	cross-sectional area of the column
A_i	specific surface
A_g	gas-water interfacial area
$(A_g/V)^*$	effective gas-water interface
C_H	empirical coefficient after Hazen
C	total concentration
C_g	concentration in the gas phase
C_w	concentration in the water phase
$C_{O_2,g}$	oxygen concentration in the gas phase
$C_{O_2,w}^{ini}$	oxygen concentration in flushing solution
$C_{O_2,w}$	oxygen concentration in the water phase
d_{10}	particle size, relative to which 10 percent of the sample is finer
d_{50}	medium grain diameter
d_{60}	particle size, relative to which 60 percent of the sample is finer
d_b	bubble diameter
d_c^{min}	minimal pore channel diameter
d_{col}	column diameter
d_{crit}	critical diameter
d_{eff}	effective film thickness
d_w	thickness of water film
D	diffusion coefficient
Da	Damkoehler number
D_w	diffusion coefficient in water
F_B	Buoyancy force
F_C	Capillary force
F_V	Viscous force
g	acceleration due to gravity
h	hydraulic head
h_a	artificial hydrostatic pressure
h_o	depth/thickness of overburden

h_w	pressure head in the water phase
$h_{w,in}$	hydraulic head at the column inlet
$h_{w,out}$	hydraulic head at the column outlet
H	dimensionless Henry's law constant
H_{O_2}	dimensionless Henry's law constant of oxygen
j	mass flux
k	rate constant
K_f	hydraulic conductivity
K_{f0}	saturated hydraulic conductivity
K_H	Henry's law constant
K_i	intrinsic permeability
K_{rw}	relative permeability with respect to water
K_f^{\max}	maximum hydraulic conductivity
$K_f^{Sg=\max}/K_f^{Sg=0}$	relative hydraulic conductivity
K_{SV}	Stern-Volmer constant
L	column length
m_{tot}	total water mass
$m_{w,in}$	mass of water flowing into the column
$m_{w,out}$	mass of water flowing out of the column
M_s	dry mass of sand
n	van Genuchten parameter
N_b	number of bubbles
N_B	bond number
N_C	capillary number
N_g	mol number in the gas phase
N_w	mol number in the water phase
p	partial pressure
p_{atm}	atmospheric pressure
p_c	capillary pressure
p_g	gas pressure
\tilde{p}_g	reduced gas pressure
p_h	hydrostatic pressure
p_{H_2O}	water vapour pressure
$p_{hyd,out}$	artificially applied hydrostatic pressure at column outflow
p_l	lithostatic pressure
p_{nw}	pressure of a nonwetting fluid

p_w	pressure of a wetting fluid/water phase pressure
Pe	Peclet number
q_w	water flux/Darcy velocity
q_w^{exp}	experimentally determined water flux
q_w^{num}	numerically determined water flux
Q_g	volumetric flow rate of gas
$Q_{g,\text{out}}$	volumetric flow rate of gas out of the column
Q_w	volumetric flow rate of water
$Q_{w,\text{in}}$	volumetric flow rate of water into the column
$Q_{w,\text{out}}$	volumetric flow rate of water out of the column
r_b	bubble radius
r_c	radius of capillary
r_p	particle radius
R	retardation factor
Re	Reynolds number
R_w	specific mass transfer rate in the water phase
R_g	universal gas constant
Sc	Schmidt number
S_e	effective saturation
Sh	Sherwood number
S_g	gas saturation
S_g^{exp}	experimentally determined gas saturation
S_g^{max}	maximum gas saturation
S_g^{num}	numerically determined gas saturation
$S_{g,\text{grav}}$	gas saturation determined by gravimetric measurements
$S_{g,\text{tracer}}$	gas saturation determined by bromide tracer tests
S^{max}	maximum saturation
S_r	residual saturation
t	time
T	temperature
u	flow velocity
u_w	water flow velocity
u_w^{max}	water flow velocity at complete water saturation
U	uniformity coefficient
V_b	volume of a single bubble
V_{col}	volume of the column

XII List of Symbols

V_g	volume of trapped gas phase
$V_{g,out}$	volume of gas flowing out of the column
V_g^{\max}	maximum residual gas volume
$V_{p,tot}$	total pore volume
V_w	volume of water phase
$V_{w,in}$	water volume flowing into the column
$V_{w,out}$	water volume flowing out of the column
x	depth/distance

Greek Letters

α_l	longitudinal dispersivity
β	mass transfer coefficient
δ	interface angle
ϕ	porosity
ϕ_{eff}	effective porosity
ϕ_{eff}^{\max}	maximum effective porosity
ϕ_{eff}^{\min}	minimal effective porosity
ϕ_{tot}	total porosity
Φ	phase angle
Φ_0	phase angle of oxygen-free water
η	dynamical viscosity
θ_g	volumetric gas content
θ_g^{\max}	maximum volumetric gas content
θ_w	volumetric water content
κ	fraction of bubble surface area exposed to mobile water
μ_g	chemical potential in the gas phase
μ_w	chemical potential in the water phase
ν	kinematic viscosity
ρ	fluid density
ρ_b	bulk density
ρ_s	particle density/rock density
ρ_w	density of water
σ	interfacial tension
$\sigma_{w,nw}$	interfacial tension between wetting and nonwetting phase
σ_{SG}	interfacial tension between solid and fluid G

σ_{SL}	interfacial tension between solid and fluid L
τ	contact time
$\tau_{l,0}$	luminescence decay time of oxygen-free water
τ_l	measured luminescence decay time

1. Introduction

In the industrial production large amounts of organic compounds which do not occur in nature (xenobiotics) are synthesized. Through leaks and spills (for example of fuel tanks), from chemical production processes, as well as from landfill leachates, these compounds gain access to the groundwater. In many cases, the groundwater contains a mixture of organic contaminants, for example petroleum hydrocarbons, aromatics like benzene, toluene, ethyl benzene and xylenes (commonly referred to as BTEX compounds), polycyclic aromatic hydrocarbons (PAH) or chlorinated hydrocarbons like chlorobenzene. Many organic contaminants are hazardous to human health and the environment. They therefore pose a significant threat to natural ecosystems and groundwater, especially since groundwater is an important resource for drinking water supply in many European regions.

For the clean up of groundwater contaminated with those organic compounds several in situ groundwater remediation approaches have been proposed (Semprini et al., 1990; Lee & Raymond, 1991; Johnson et al., 1993; Wilson et al., 1997; Schirmer, 2001). Especially for sites with high and widespread contaminations, active in situ techniques represent a cost-efficient remediation alternative. Recently, natural attenuation using the self-purification potential of the aquifer gained acceptance throughout North America and Europe (National Research Council, 1993; Norris et al., 1994; MacDonald, 2000; Cunningham et al., 2001). At this remediation process, the contaminant concentration is decreased by physically, chemically and microbiologically controlled processes, for example dilution, dispersion, precipitation, ion-exchange, unspecific sorption and biodegradation (Barker et al., 1987; MacDonald, 2000). Biodegradation is a very important process, since it can result in a complete mineralization of the contaminants, which means an irreversible transformation of the toxic contaminants to non-toxic compounds (Norris et al., 1994; Beek, 2001; Chapelle, 2001). It has to be considered though, that incomplete biodegradation can sometimes lead to even more toxic metabolites compared to the source compounds.

Numerous studies have shown that indigenous microbial communities are capable of acclimating to a variety of chemical stresses imposed by human activity. In the process of acclimating themselves to these stresses, microorganisms often accelerate the natural degradation of the chemicals involved (Chapelle, 2001). In general, microorganisms are able to degrade a multitude of contaminants (Borden & Bedient, 1986; Fritsche, 1990; Pardieck et al., 1992; Reineke, 2001). Contaminants in groundwater can be metabolized by microorganisms as primary substrates or via cometabolism. Cometabolism is a process where

microbes do not consume contaminants primary, but live on an alternate food source instead and accidentally create conditions that trigger the degradation of the contaminants (Madigan et al., 2000).

Many of these microorganisms able to degrade contaminants are aerobic, that means they are using oxygen as the terminal electron acceptor (Bae et al., 1995; Fry et al., 1996; Donaldson et al., 1997). Furthermore, some important contaminants like the gasoline additive methyl tert-butyl ether (MTBE) are relatively persistent under anaerobic conditions and can only be degraded reasonably with the help of aerobic bacteria (Finneran & Lovely, 2001; Nyer et al., 2002). At a large number of natural attenuation test sites, the absence of oxygen is the actual limiting factor for the degradation process (Borden & Bedient, 1986; Barker et al., 1987; Chiang et al., 1989; Hoepfel et al., 1991; Johnson et al., 1993; Teutsch et al., 1997). Typical dissolved oxygen concentrations in uncontaminated groundwater are less than 4 mg/l and, under conditions induced by the natural degradation of the contaminants, are often less than 0.5 mg/l or anoxic (Nyer et al., 1996). Thus, the naturally occurring attenuation process can be enhanced by adding oxygen to switch the metabolic pathways from anaerobic to aerobic conditions. This is referred to as enhanced natural attenuation.

During the last years, various strategies for increasing the dissolved oxygen concentration have been developed to enhance aerobic in situ bioremediation. An effective and cost-efficient option is a special method of direct gas injection (in the following referred to as direct oxygen injection). This method is intended to create a broad wall or zone of trapped oxygen gas bubbles in the pore space and allow time for the gas to dissolve and increase the oxygen concentration in the groundwater flowing through (Fry et al., 1997; Carter, 1998). Thereby, the aquifer is acting as a gas deposit using the ability of the porous media to store a residual non-wetting fluid phase of approximately 14 – 17 % of the pore space (Fry et al., 1997). The immobile gas phase acts hydraulically and biologically as a reactive bubble wall. Gas emission into the unsaturated zone shall be limited to achieve a high efficiency of the gas entry (Weber, 2000). By the use of pure oxygen gas, dissolved oxygen concentrations of more than 50 mg/l can be achieved at typical aquifer temperatures (instead of approximately 11 mg/l when using air). The success of this remediation technique depends on the transfer of oxygen between the gas and water phase whereby the oxygen releasing process is governed by mass transfer kinetics.

Mass transfer reactions between water and gas phase play an important role for a variety of applications. For example, many other in situ remediation technologies make use of the mass transfer from a gas phase to an adjacent water phase. A common example is air sparging at

which contaminants are volatilized through a continuous gas flow. Moreover, the injection of reactive gases like H_2 , CH_4 , NH_3 , CO_2 and others are used in order to initiate, stimulate and control microbial oxidative and reductive degradation processes of organic contaminants (Fry et al., 1997, Luckner, 2001; Geistlinger et al., 2003). Besides the wide application field of continuous or discontinuous gas injection for in situ remediation, interphase mass transfer reactions are also important for the use of partitioning gas tracers (Bruce et al., 2001; Vulava et al., 2002). Partitioning gas tracers are dissolved gases (for example SF_6 , Kr or He) that are injected into groundwater and are retarded in unsaturated aquifers due to a partitioning into the gas phase. Thus these tracers can be used to determine hydrogeological parameters like the volume of gas-filled areas or partitioning rates (Vulava et al., 2002). Another application is the paleotemperature reconstruction from noble gases in groundwater (Aeschbach-Hertig et al., 2000; Holoher et al., 2003). The main problem is the so called “excess-air” phenomena, i.e. the gas concentration in the groundwater does not obey the equilibrium partition. Supersaturation of air in water may occur due to dissolution of air bubbles, resulting in “excess air”. Air bubbles are trapped when the water table is rising and are completely dissolved by the increasing hydrostatic pressure. In all cases a comprehension of the dissolution process of multi-component gas phases in a mobile water phase containing a variety of dissolved gases or volatile organics is necessary (Geistlinger et al., 2005). However, the scientific basics of the dissolution of gas bubbles in porous media and their effects on aquifer properties are not well understood.

The aim of this work is to investigate the important processes that determine the effectiveness of direct oxygen injection and the subsequent dissolution of the gas phase on a bench scale. In addition to the static characterization of the gas injection method (gas phase distribution, gas storage capacity), a dynamic process description is needed for ongoing processes in the subsurface, particularly the temporal evolution of volumetric gas content and its effect on hydraulic conductivity. Above all, the basic phenomena of the behaviour of oxygen in the aquifer shall be examined, particularly the interphase mass transfer between a trapped gas phase and a mobile water phase containing dissolved gases. Knowledge of oxygen transfer rates is especially important, since they can be used to estimate remediation time scales. Oxygen is most widely needed for bioremediation of contaminated aquifers but other gases such as hydrogen and methane, proved to be effective for some remediation cases (Roberts et al., 1990; Semprini et al., 1990; Wilson & Mackay, 2002), could be used as well.

The main questions are:

1. What amount of gas can be captured in the pore space during direct oxygen injection?
2. How fast can the trapped gas be dissolved and what is the resulting dissolved oxygen concentration in the water phase?
3. How do other gases already dissolved in the groundwater affect the dissolution of a trapped oxygen gas phase?
4. How does the trapped gas phase influence the hydraulic conductivity?

To answer these questions laboratory column experiments were conducted with dynamically compressed sediments and a direct gas injection of pure oxygen gas. The effect of various gases (argon, nitrogen, helium) already dissolved in the mobile water phase on the dissolution process was evaluated under different flow regimes. Since gas partitioning occurs between the mobile aqueous phase and a stationary trapped gas phase (Gupta et al., 1994; Fry et al., 1995; Donaldson et al., 1997; Bruce et al., 2001; Vulava et al., 2002), these dissolved gases tend to transfer into the oxygen gas bubbles and therefore have an effect on the oxygen mass transfer by changing the partial pressure of oxygen in the gas phase (Bae et al., 1995). Furthermore, the changes in hydraulic conductivity during gas injection and the dissolution process were investigated. Thereby, the saturation state of the column was characterized by three independent methods: By gravimetric measurements, by bromide tracer tests, and by hydraulic conductivity measurements.

A new developed kinetic multi-component model (variable gas volume, saturation-dependent rate constant, velocity-dependent mass transfer coefficient) (Lazik et al., 2002; Geistlinger et al., 2005) was used to describe the experiments and validated through integral information. The model is referred to in the following as variable volume model (VVM). The rate of interphase mass transfer was investigated in a two-component system as a function of aqueous phase velocity for the upper range of typical groundwater velocities, volumetric water and gas contents, and porous media characteristics. Moreover, the numerical solution of the VVM was compared to a semi-analytical solution of a model based on a local equilibrium approach (Cirpka & Kitanidis, 2001). Good estimated values of the mass transfer rate and the mass transfer coefficient provide a basis for the development of prognosis models for the computer simulation of field experiments.

2. Direct Oxygen Injection

2.1 Overview on In Situ Remediation Strategies to Increase the Dissolved Oxygen Concentration

Several strategies for increasing the dissolved oxygen concentration in groundwater to enhance natural attenuation processes are described in the literature. One option is the injection of water sparged with pure oxygen combined with a groundwater extraction at a second well downgradient of the injection well (Thomas & Ward, 1989; Semprini et al., 1990; Hoepfel et al., 1991; Luckner et al., 2001). Though this method may be relatively straightforward, its effectiveness is limited due to the low solubility of oxygen in water. Moreover, the water containing the dissolved oxygen will be diluted quickly. Consequently, the mass of oxygen delivered to the contaminated aquifer is relatively small (Fry et al., 1997). Furthermore, problems can arise regarding the handling of the injection of oxygen enriched water due to bubble nucleation. Oxygen bubbles can exsolve out of the water phase if the gas dissolved in the water is supersaturated. Supersaturation can occur if there is a decrease in pressure or an increase in temperature during the injection.

To avoid the problems arising during the injection of oxygen saturated water, several methods have been proposed for transferring oxygen into groundwater directly in the well. For example Bae et al. (1995) developed an apparatus for down-well oxygen transfer consisting of a restriction section for gas addition and a gas transfer section. Water is mixed with oxygen gas in the restriction section and then pressed through small holes into a cone – the gas transfer section – at high velocities. The oxygen partially degasses, whereby the gas bubbles are trapped in the cone. Due to the high water velocities, vigorous turbulent mixing occurs in the gas transfer section, further enhancing gas transfer between the water and a fine bubble swarm trapped in the cone. Wilson & Mackay (2002) developed a device that provides a uniform oxygen transfer into groundwater in wells by diffusion from pressurized polymeric tubing. Thereby, they tested four readily available tubing materials. Both methods have the disadvantage that the radius of influence is comparatively small. The dissolved oxygen has to be transported from the well with the groundwater flow. Therefore, the deliverance of oxygen may be limited to the immediate vicinity of the well at sites with low flow velocities.

Another option to increase the dissolved oxygen concentration in contaminated aquifers is the injection of water containing dissolved hydrogen peroxide, which decomposes to oxygen and water (Barenschee et al., 1991; Huling et al., 1991; Pardieck et al., 1992; Fry et al., 1997). The rate at which hydrogen peroxide decomposes to oxygen can be controlled using additives

(Huling et al., 1991). However, hydrogen peroxide can be toxic to microorganisms at higher concentrations (Atlas, 1991; Pardieck et al., 1992). Furthermore, the use of hydrogen peroxide is quite cost-intensive (Prosen et al., 1991; Fetter, 1993). Following a comparison of costs from Fields et al. (2002), the use of solid peroxide compared to pure oxygen for example differs at an expense factor of approximately 10^2 at a comparable achievable oxygen concentration from around 50 mg/l (Table 1).

TABLE 1: Achievable dissolved oxygen concentration range and estimated cost of oxygen \$/Pound (from Fields et al., 2002).

Oxygen source	Achievable oxygen concentration range [mg/l]	Estimated cost of oxygen [\$/Pound]
Air	8 – 10	0.01
Pure liquid oxygen (LOX)	40 – 50	0.1
Pure oxygen (generated)	40 – 50	1
Liquid H ₂ O ₂	25 – 50	10
Solid peroxide	25 – 50	100

A relatively new approach is the use of oxygen releasing material (ORM) such as ORC[®] (Regenesis Bioremediation Products) and PermeOx[®] (FMC Corporation). ORMs consist of mild oxidants (ORC[®]: Magnesium peroxide, PermeOx[®]: Calcium peroxide) manufactured in a solid form (powder or granular) that hydrolyze into molecular oxygen when saturated with water (Koenigsberg & Sandefur, 2001; Nyer et al., 2002). These compounds can be used either in passive remediation strategies like permeable reactive barriers or in active remediation technologies by pressure injection into the subsurface using boreholes or a direct-push probing rig, whereby the ORMs are mixed with water to form an injectable slurry (Koenigsberg & Sandefur, 2001; MacEwen et al., 2001; Nyer et al., 2002). The slurry injection method has proven to be lower in cost and faster acting compared to passive barrier methods (Koenigsberg & Sandefur, 2001). ORMs release oxygen at a slow rate over a relatively long period of time. However, the release rates of the ORMs are not constant over the lifespan of the material. This makes matching the oxygen supply to the plume demand more complicated over the long term (Wilson et al., 1997). Nevertheless, ORMs can increase the dissolved oxygen levels in groundwater up to five times greater than using atmospheric air, though the oxygen transfer efficiency ranges from 25 % to 50 % only (Nyer et al., 2002). Consequently, a rather large amount of ORM is needed to deliver the required amount of oxygen to the aquifer. Moreover, comparable to the down-well oxygen transfer methods, the

radius of influence is quite small. The ORMs similarly have to be transported from the injection point with the groundwater flow limiting the deliverance of oxygen to the immediate vicinity of the injection point. Following Koenigsberg & Sandefur (2001), the technology is best applied to dissolved phase plumes and moderate levels of residual contaminants, once the majority of the source is removed by more effective remediation methods.

A more effective method includes the direct injection of gas containing oxygen. Twenty-eight times more oxygen per volume can be stored in the gas phase than can be dissolved in water, assuming equilibrium based on Henry's law at 15°C (Fry et al., 1997). Regarding the direct injection of gases, two different strategies can be distinguished: One example is air sparging, which is mainly aimed at the volatilization of volatile organic compounds (VOCs) through a continually gas flow using an injection well and an air compressor (Johnson et al., 1993; Adams & Reddy, 1999; Aelion & Kirtland, 2000; Adams & Reddy, 2003). In most cases, air sparging is combined with a soil vapor extraction (SVE) to remove the stripped contaminants (Bruce et al., 2001; Peterson & Murray, 2003). To achieve a uniform distribution of the gas in the porous medium Johnson et al. (1993) suggest high gas flow rates.

Air sparging is potentially effective in homogeneous, highly permeable aquifers and with compounds that are easy to volatilize, for example BTEX (Nyer et al., 1996; Schirmer, 2001). The main mechanisms responsible for contaminant removal during the operation of an air sparging system are: In situ stripping of dissolved VOCs, volatilization of trapped and sorbed phase contaminants below the water table and in the capillary fringe, and aerobic biodegradation of contaminants that is enhanced by oxygen supply (Nyer et al., 1996). Air sparging aimed at enhancing biodegradation is often referred to as biosparging (Adams & Reddy, 2003). However, the primary remediation process of air sparging is volatilization, particularly at sites where dissolved contaminant concentrations are greater than 1 mg/l (Johnson, 1998). Moreover, the effectiveness of air sparging to increase the dissolved oxygen concentration in an aquifer is uncertain. Following Nyer et al. (1996), the dissolved oxygen levels can be raised by air sparging to no more than 6 to 10 mg/l under equilibrium conditions.

This is in contrast to the direct oxygen injection intended to create a broad oxygen bubble wall. By this method, a dissolved oxygen concentration of approximately 50 mg/l can be attained in the groundwater. Fry et al. (1997) proposed the following procedure: Applying discontinuous gas injection, stopping the injection shortly after the breakthrough in the unsaturated zone and using the ability of the porous media to store a residual non-wetting fluid. Thereby, sediment boundaries can be used as hydraulic barriers against vertical gas flow

to increase the lateral extension of the gas phase. In this manner a large radius of influence can be achieved. After almost complete dissolution and consumption through biotic or abiotic processes, a new gas pulse is injected. The oxygen gas phase is assumed to be trapped in the sediment in terms of discontinuous immobile gas bubbles (Faybishenko, 1995) (Figure 1). The size of the single gas bubbles shall be small to increase the gas-water interfacial area A_g [m^2]. A greater interfacial area results in an increased specific mass transfer rate R_i^w [$kg/l s$], which means that more oxygen can be transferred from the gas to the water phase in shorter time. A larger number of small gas bubbles will therefore dissolve faster than a small amount of large bubbles, even if the sum of the gas volume of all bubbles is the same (Holocher et al., 2003). The trapped gas bubbles will act as a significant source of oxygen for the groundwater flowing through the bubble wall and dissolving the gas phase.

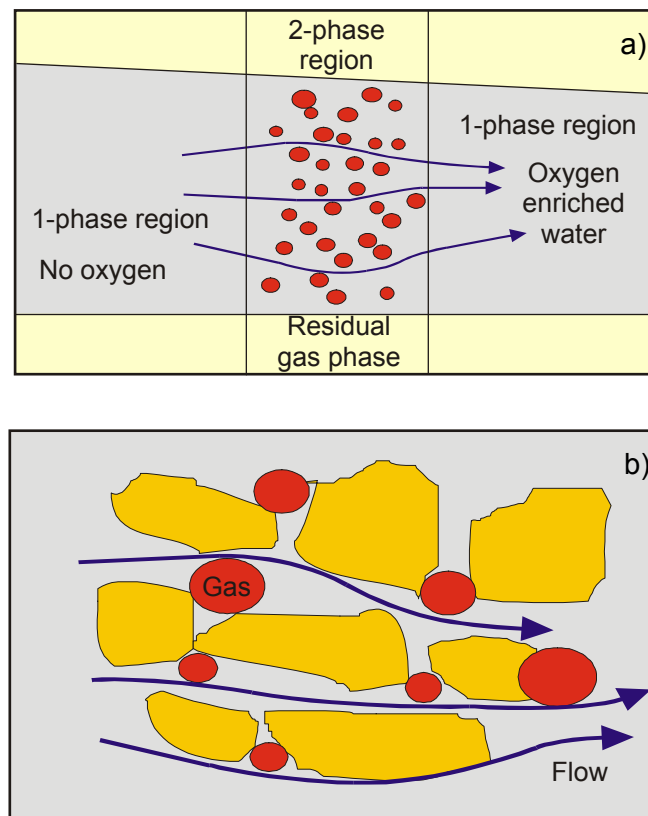


FIGURE 1: Conceptual model of an oxygen bubble wall: a) macro and b) micro scale. The red dots symbolize the oxygen bubbles; the blue arrows denote the water flow direction (after Fry et al., 1997).

Figure 1 shows the occurrences at the macro and micro scale within an oxygen bubble wall. The grey colored area in Figure 1a) denotes the saturated aquifer, the red dots symbolize the oxygen bubbles. Upstream of the bubble wall there is a one-phase region filled with water that

contains none to very little oxygen. The bubble wall itself can be considered as a two-phase region with an aqueous and a gaseous phase. During the passage of the groundwater through the oxygen bubble wall, there is a permanent supply of oxygen from the trapped gas phase. Downstream of the oxygen bubble wall, we finally find a one-phase region again, hence filled with oxygen enriched water. Figure 1b) shows how the bubbles are captured in the aquifer with the water passing by (blue arrows).

The direct oxygen injection has the advantage of being cost-efficient compared to conventional in situ air sparging methods at optimal control of the injection, since the soil vapor extraction and treatment of the extracted gas is omitted. Furthermore, it is also relevant for sites with non-volatile organic compounds. At the same time, the direct oxygen injection provides a considerable quantity of dissolved oxygen for the bioremediation of contaminated groundwater since pure oxygen is used. By an accurate dimensioning of the oxygen bubble wall regarding its length and the gas distribution, a deliverance of oxygen meeting the stoichiometric requirements for complete contaminant degradation can be achieved.

2.2 Basic Mechanisms Influencing Gas Trapping and Achievable Gas Saturation

To perform a direct oxygen injection with the objective of creating an oxygen bubble wall, the mechanisms leading to a trapping of a residual gas phase in the water-filled sediment have to be understood.

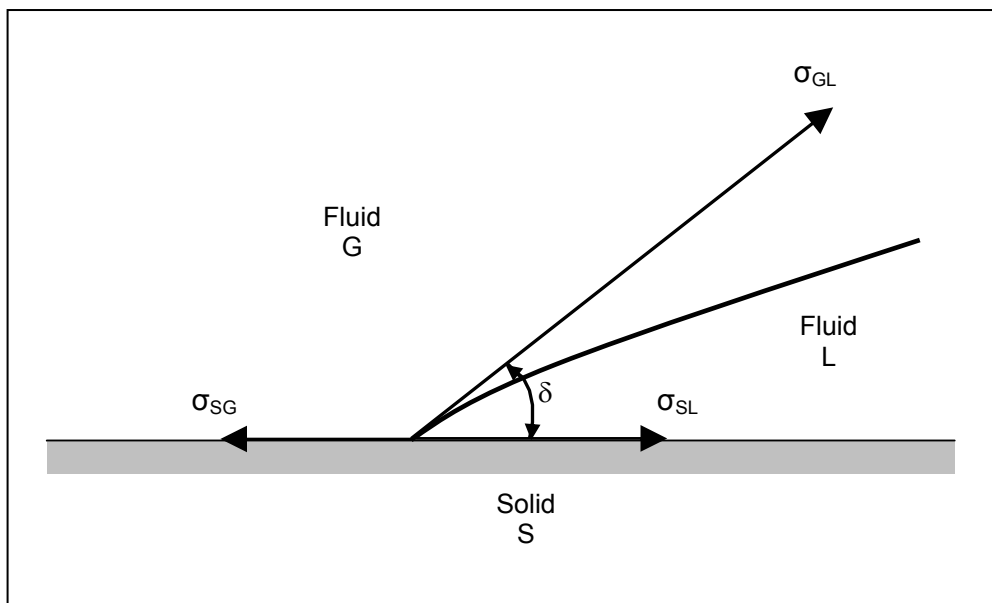


FIGURE 2: Interfacial tensions between a solid surface S, a wetting fluid L, and a non-wetting fluid G (after Fetter, 1993).

A liquid in contact with another substance, which can be a solid, an immiscible liquid, or gas, possesses interfacial energy (Fetter, 1993). This energy is the result of the difference in the degree of attraction for the molecules of the liquid at the interface to each other compared with their degree of attraction for molecules of the other substance. The amount of work necessary to separate a unit area of one substance from another is defined as interfacial tension σ [N/m]. Figure 2 shows the interfacial tension between two fluid phases, G and L, and a solid surface S. The interface angle between the two fluids is indicated by δ [-]. Equation 1 gives the relationship between δ and the interface tensions for the three interfaces: fluid G/solid S, fluid L/solid S, and fluid G/fluid L (Fetter, 1993):

$$\cos \delta = \frac{\sigma_{SG} - \sigma_{SL}}{\sigma_{GL}}. \quad (1)$$

Normally, δ is measured through the denser fluid. In general, one of the fluids will preferentially spread over (wet) the entire solid surface. If δ is less than 90° , then fluid L will preferentially wet the surface. If δ is more than 90° , then fluid G will preferentially wet the surface. Thus, if two fluid phases are competing for a surface, one dominates and coats the solid surface. This phase is characterized as the wetting phase, the displaced one as the nonwetting phase (Wardlaw, 1982; Busch et al., 1993). Consequently, the interface angle between the wetting/nonwetting phase interface and the solid surface characterizes the wettability. In this work, gas is the nonwetting phase and water the wetting phase.

If a nonwetting phase like gas shall displace water in a porous medium, then a capillary pressure p_c [Pa] has to be overcome. If p_w [Pa] is the pressure of the wetting fluid and p_{nw} [Pa] is the pressure of the nonwetting fluid, then the capillary pressure can be expressed by:

$$p_c = p_w - p_{nw}. \quad (2)$$

This means that the capillary pressure is a function of the properties of the two fluids present. Moreover, it is dependent on the geometry of the porous media. According to Laplace's law, the capillary pressure depends on the interfacial tension between wetting and nonwetting phase $\sigma_{w,nw}$, the interfacial angle of this interface to the capillary wall and on the radius r_c [m] of the capillary itself:

$$p_c = \frac{2 \cdot \sigma_{w,nw} \cdot \cos \delta}{r_c}. \quad (3)$$

In the case that gas is the nonwetting phase and water the wetting phase in siliceous sediment, the interfacial angle can be approximated to be 0° . Then a special form of Laplace's law is valid:

$$p_c = \frac{2 \cdot \sigma_{w,g}}{r_c}. \quad (4)$$

To inject oxygen gas in a depth x under the groundwater surface, the injection pressure that has to be overcome is thus given by the sum of the capillary pressure p_c resulting from the interfacial tension, and the hydrostatic pressure p_h [Pa] given by the depth of the injection point in the body of water (Holoher et al., 2003). The flow of the oxygen gas through the porous medium is dependent upon the densities, viscosities and interfacial tensions of the fluids in the system. Moreover, sediment characteristics as pore size distribution and packing density are important factors, which determine the dynamic coherent gas phase distribution during gas injection. Experimental investigations of gas flow in porous media (Ji et al., 1993; Adams & Reddy, 1997; Brooks et al., 1999; Peterson et al., 1999) demonstrated that different gas flow patterns were yielded in dependency of the grain size. For fine to coarse gravels (grain size > 2 mm), the flow regime was characterized by discrete gas bubbles that migrated through the pores under the influence of the buoyancy force (bubbly flow). For sand and silt (grain sizes < 2 mm), areas with continuous pore-scale gas channels were developed within the porous medium (channel flow). Following Elder & Benson (1999), these channels are narrower, more tortuous and more closely spaced in coarse sand than in fine to medium sand. The horizontal extension of the gas flow is larger in fine to medium sand than in coarse sand (Clayton, 1998; Elder & Benson, 1999; Peterson et al., 2001). Peterson & Murray (2003) investigated the effect of grain-size heterogeneity and sediment stratification on gas flow patterns and describe an increase in the extent of the sediment area affected by gas in coarsening-upward sequences.

The pressure distribution in a flowing gas channel through a porous medium is represented in Figure 3a). Upon completion of injection, the coherent phase boundary area collapses into incoherent immobile gas phases of different shapes and sizes (Elder & Benson, 1999) (Figure 3b). The conceptual model applied in this work regards these incoherent gas phases to exist as trapped spherical gas bubbles distributed spatially uniform throughout the porous medium.

Gas bubbles trapped in saturated porous media are, in general, thermodynamically unstable since their removal reduces the total interfacial area and thereby the interfacial energy (Peck, 1969). The bubble form is preferred as it is the minimal energetic state for the gas phase. Larger irregular gas volumes (aggregates) are unable to maintain a stable mechanical equilibrium state over the whole phase boundary area due to snap-off effects and the inhomogeneous pressure distribution in the water phase (Dullien, 1992). The lower

hydrostatic pressure at the upper boundary layer has to be compensated by a stronger curvature, which leads to a dispartment of the gas aggregates.

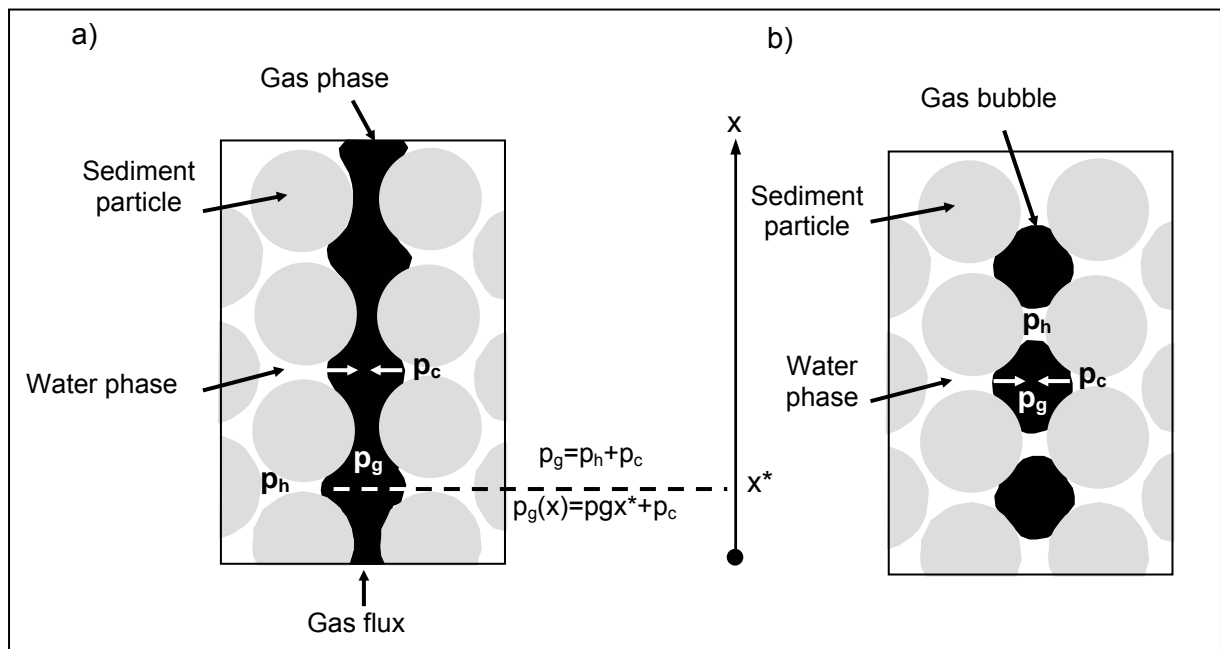


FIGURE 3: a) Pressure distribution in a gas filled capillary. b) Trapped gas bubbles after the injection pulse.

The factors determining the microscopic mechanism of gas bubble trapping are according to Morrow & Songkran (1981):

- the geometry of the pore network;
- fluid properties such as interfacial tension, density difference, viscosity ratio and phase behavior;
- fluid-sediment interfacial properties which determine the wetting behavior;
- applied pressure gradient and gravity.

In general, the forces that act on a trapped gas bubble in a porous media are capillary, viscous and buoyancy forces which prevail during the displacement of one fluid by another (Figure 4) (Wardlaw, 1982). The capillary forces are proportional to the interfacial tension between immiscible fluid phases and the wettability of the solid phase by a fluid. The viscous forces are proportional to the permeability of the media and the pressure gradient, and buoyancy forces are proportional to the density differences between the fluids (Fry et al., 1997). Parameters that will influence trapping of a nonwetting phase can be accounted for by using dimensionless numbers (Morrow & Songkran, 1981). The dimensionless numbers of interest

are the bond number N_B (buoyancy/capillary forces) and the capillary number N_C (viscous/capillary forces):

$$N_B = \frac{\Delta\rho \cdot g \cdot r_p^2}{\sigma_{w,nw}}, \quad (5)$$

$$N_C = \frac{u \cdot \eta_w}{\sigma_{w,nw}}, \quad (6)$$

where $\Delta\rho$ [kg/m^3]: fluid density difference, g [m/s^2]: acceleration due to gravity, r_p [m]: particle radius, u [m/d]: flow velocity, η_w [Pa s]: dynamical viscosity of displacing fluid.

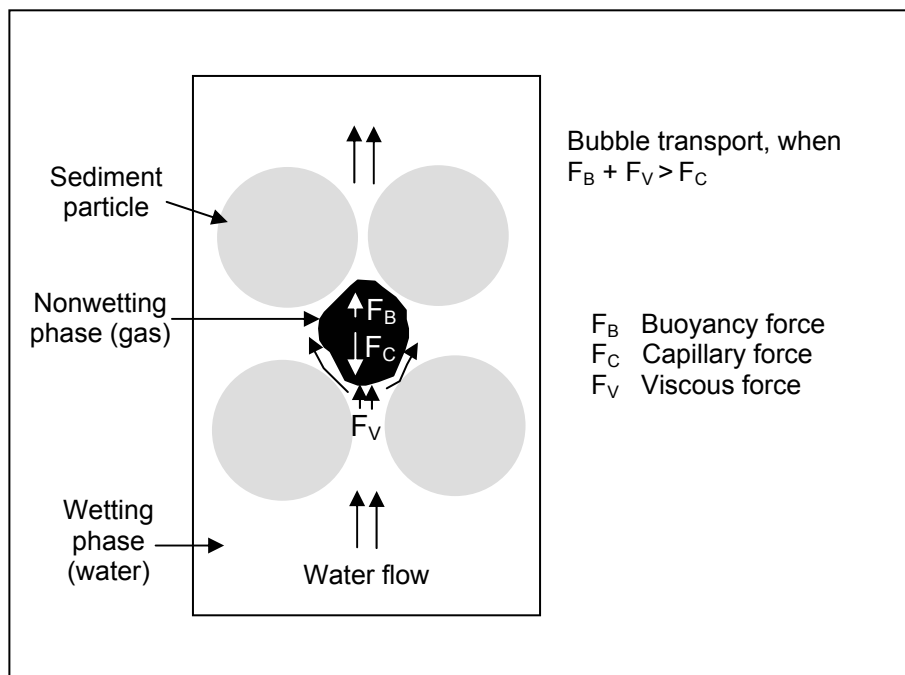


FIGURE 4: Balance of forces acting on a gas bubble (after Weber, 2000).

Gas bubbles will be trapped in the aquifer when the capillary forces are greater than buoyancy forces or viscous pressure gradient (small capillary and bond number) (Morrow & Songkran, 1981; Fry et al., 1997). In the case of vertical flow (conditions during the column experiments performed in this work, see Chapter 4.2) the buoyancy and viscous forces act in the same direction and their absolute values will sum up (Figure 4). Following Morrow & Songkran (1981), the critical bond number above which no trapping occurs is 0.35. For the experiments of this work, a bond number of approximately 0.012 was calculated; consequently the capillary forces hold the gas phase in the interstitial pore spaces over the buoyancy forces. At typical groundwater velocities, the viscous forces will be small relative to the capillary forces, and thus it will be difficult to mobilize the gas phase once it is emplaced (Fry et al., 1997).

The viscous forces necessary for mobilization of a nonwetting phase that has been trapped are significantly greater than the viscous forces needed to prevent entrapment of the nonwetting phase initially (Morrow & Songkran, 1981).

One factor that determines the residual saturation of a nonwetting phase, i.e. the total volume of gas phase that is immobilized in the porous media, is the structure of the pore space (Peck, 1969; Wardlaw, 1982; Chatzis et al., 1983). Gas bubbles can be trapped in both dead-end and open pores (Faybishenko, 1995). Larger numbers of poorly connected pores and an increase in pore size variability correlate with an increase in residual saturation (Peck, 1969; Coskun and Wardlaw, 1994, from Fry et al., 1997). The aspect ratio of pore-body to pore-throat size will also affect the volume trapped. The greater the aspect ratio, the larger the volume trapped (Wardlaw, 1982; Chatzis et al., 1983). Column experiments performed by Fry et al. (1997) with uncompressed uniform sediments have shown that the residual nonwetting phase saturation during direct gas injection is not dependent on the grain size, unless the matrix is so fine that the wetting phase cannot be displaced initially by the nonwetting phase (Chatzis et al., 1983). The gas saturations achieved in those experiments ranged from 14 % to 17 % of the pore space. Nevertheless, the gas flow distribution during gas injection will have an effect on the gas saturation in the way that gas bubbles will only be trapped in the areas beforehand affected by the gas flow. In consequence of the broader distribution of the gas flow in finer sediments, the distribution of trapped gas bubbles can be expected to be larger in fine to medium sand.

2.3 Mass Transfer between Gas and Water Phase

Once a gas bubble is trapped in the porous medium, oxygen from the gas phase will be transferred to the surrounding water phase with a low dissolved oxygen content (Figure 5). On the other hand, already dissolved gases – like CO₂ and N₂ – will accumulate in the residual gas phase (Gupta et al., 1994; Fry et al., 1995; Donaldson et al., 1997; Bruce et al., 2001; Vulava et al., 2002). The gas partitioning of all gas components in the system is coupled, so that the behavior of a single gas component cannot be considered independently of the others (Cirpka & Kitanidis, 2001). Consequently, the injection of a one-component gas phase in a real aquifer, which contains dissolved gases, leads to a multi-component mass transfer process (Geistlinger et al., 2005). The driving force of the mass transfer is the concentration gradient between the gas and the water phase (Schwarzenbach et al., 2002). The transport of the components from one phase to the other will be mainly due to diffusion. Since every gas has a different diffusion coefficient as well as a different concentration gradient, the transfer of the

single components out of or into the bubble will be varying, so that the gas bubble will either dissolve or enlarge. The system can adapt to an increased transfer of dissolved gases from the water phase into the gas phase by increasing the gas saturation (Cirpka & Kitanidis, 2001).

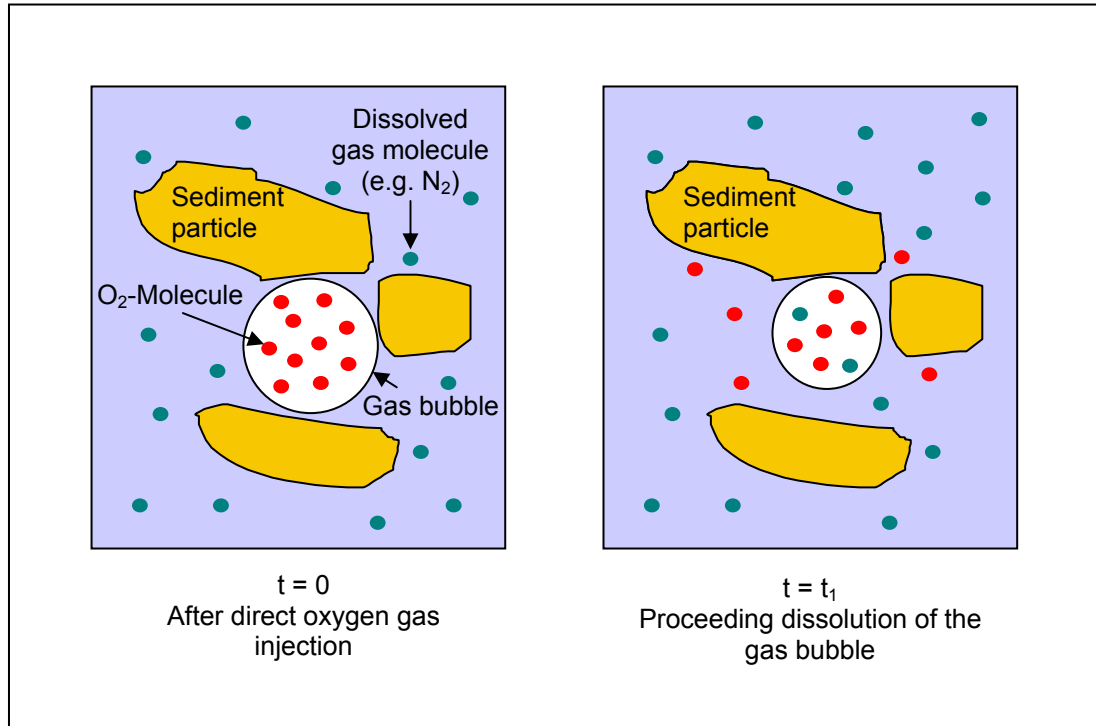


FIGURE 5: Conceptual model: Dissolution of the gas bubble.

A factor that will increase the concentration gradient is the pressure acting on the trapped gas bubble. This pressure is the sum of hydrostatic and capillary pressure and creates an increase in the pressure inside the gas bubble causing the concentration of gas in the bubble to rise. Thereby, the sum of partial pressures of the single gas components cannot exceed the pressure acting on the gas phase in the medium (Bae et al., 1995; Cirpka & Kitanidis, 2001). The increased concentration in the gas bubble creates a concentration gradient causing the gas to slowly diffuse out of the bubble into the surrounding water. As Figure 3 indicates, the gas pressure increases with increasing depth. That means that gas bubbles in the deeper aquifer dissolve faster than in the upper aquifer assuming the same boundary conditions. The capillary pressure is the reason for a complete dissolution of any residual gas phase in the aquifer, since the radius of curvature of the gas bubble creates a permanent concentration gradient (Fry et al., 1997) and will maintain a non-equilibrium state. Nevertheless, the capillary pressure induced dissolution process will be relatively slow, since the capillary pressure acting on a gas bubble in a typical aquifer material is normally quite low (Cirpka &

Kitanidis, 2001). Taking the medium grain diameter $d_{50} = 0.3$ mm as capillary radius, a capillary pressure of about 0.5 kPa was calculated for the experiments in this work.

Nonetheless, a gas bubble trapped in the porous medium will shrink after a while. As soon as the trapped gas bubble has reached a critical diameter $d_{\text{crit}} < d_c^{\text{min}} / 2$ (d_c^{min} : minimal pore channel diameter, approximately 0.08 mm for the sediment used in this work), it leaves the pore space and will move fast upwards due to buoyancy. During the upward movement, the gas bubble volume increases (Peck, 1969) since the hydrostatic pressure decreases and the gas bubble can be trapped again. Therefore, the dissolution process of the entire gas bubbles is accompanied by a stochastic rearrangement of the gas bubbles from below to top and in flow direction. As soon as the gas is dissolved in the water, it will be transported, like any solute, through a porous medium by the processes of advection and dispersion.

2.4 Hydraulic Conductivity

The hydraulic conductivity K_f [m/d] describes the ability of the aquifer material to conduct water through it under hydraulic gradients. It is a combined property of the porous medium and the fluid flowing through it, for example pore space, friction coefficients and fluid viscosity (Bear, 1972; Zheng & Bennett, 2002):

$$K_f = K_i \cdot \frac{\rho_w \cdot g}{\eta_w}, \quad (7)$$

where K_i [m^2] is the intrinsic permeability. For the experiments described in this work, the fluid properties as well as the geometry of the pore space can be considered to be relatively stable. However, there is an influence on the hydraulic conductivity during direct gas injection. The trapped gas bubbles are blocking the pores leading to a modification of the effective porosity and permeability. If gas bubbles are trapped in the column, the hydraulic conductivity decreases. During the dissolution of the gas phase, the hydraulic conductivity will be increasing again. An entrapment of gas bubbles can also occur by other remediation strategies like air sparging, or in some cases by the injection of hydrogen peroxides (Fry et al., 1996). The effect of trapped gas on the hydraulic conductivity of soils has been described extensively in the literature (Christiansen, 1944; Faybishenko, 1995; Fry et al., 1997).

3. Conceptual Models

3.1 Modeling of Mass Transfer between Gas and Water Phase

A variety of conceptual models and mathematical approaches exist to describe mass transfer among phases in a multi-component multi-phase system. These models have been advanced by investigators involved with fluid mechanics, surface water hydraulics, separation chemistry, chemical process engineering, and heat transfer (Bird et al., 1960; Levich, 1962; Levenspiel, 1972; Crank, 1975; Treybal, 1980; Cussler, 1997; Geistlinger et al., 2003). Mass transfer models have been based upon a variety of transport processes that may occur in the vicinity of phase interfaces, such as diffusion, advection, and turbulent flow phenomena (Miller et al., 1990).

The dissolution process of a residual gas phase consisting of single trapped gas bubbles has strong similarities with the dissolution process of a fine-dispersed trapped Non Aqueous Phase Liquid (NAPL) which consists of single trapped blobs. In both cases the diffusive and advective transport of dissolved species away from the phase boundary limits the mass transfer. Therefore, some of the following arguments are taken from literature concerning NAPL-dissolution.

3.1.1 Equilibrium Approach

Mass transfer between the gas and water phase will continue until equilibrium is reached. It will proceed until the chemical potential of a component i $\mu_{i,g}$ [-] and $\mu_{i,w}$ [-] of both phases have been equilibrated:

$$\mu_{i,g} = \mu_{i,w} \quad (8)$$

Consequently, the simplest attempt to describe the mass transfer is the equilibrium-approach according to Henry's law (Gulliver, 1990; Fry et al., 1995):

$$C_{i,g} = H_i \cdot C_{i,w} \quad (9)$$

($C_{i,g}$ [kg/m^3]: concentration of component i in the gas phase; H_i [-]: dimensionless Henry's law constant of component i ; $C_{i,w}$ [kg/m^3]: concentration of component i in the water phase) (Appendix 1). The net flux of any gas molecule across an interface is well described by Fick's law:

$$j = -D \cdot \left. \frac{\partial C_g}{\partial x} \right|_{x=0} \quad (10)$$

where j [$\text{kg}/\text{s m}^2$] is the mass flux of gas molecules per unit surface area across the interface, D [m^2/d] the diffusion coefficient of the gas, C_g [kg/m^3] the concentration of the gas, and x

[m] is the distance from the interface. In column experiments described by Fry et al. (1995), investigating the effect of a trapped gas phase on the transport of dissolved gases in water, an equilibrium-based retardation factor was described as:

$$R_i = 1 + H_i \cdot \frac{V_g}{V_w} \quad (11)$$

(R_i [-]: retardation factor of component i ; V_g [m^3]: volume of trapped gas phase; V_w [m^3]: volume of water phase) and could not describe the gas partitioning between trapped gas and a mobile aqueous phase satisfactorily. The measured retardation factors for oxygen were higher than the theoretical ones, when the gas saturation was 5 % of the pore volume or higher. Moreover, a change of gas saturation was not included in their model (V_g/V_w was held constant), which does not comply with the actually occurring physical process that the gas saturation changes during gas partitioning. Fry et al. (1997) identified kinetic mass transfer as a factor contributing to a delayed breakthrough.

Cirpka & Kitanidis (2001) developed a semi-analytical model, based on a local equilibrium approach that takes into account a trapped multi-component gas phase and changes in gas saturation. They performed numerical model calculations for gas tracers with various dimensionless Henry's law constants neglecting dispersion and mass transfer kinetics. The governing equations are formulated as functions of total concentrations. The total concentrations C_i [kg/m^3] can hence be expressed by the concentration of the component in the gas or aqueous phase, respectively:

$$C_i = \left\{ \frac{1 - S_g}{H_i} + S_g \right\} \cdot C_{i,g} = \frac{1 + S_g(H_i - 1)}{H_i} \cdot C_{i,g}, \quad (12a)$$

$$C_i = \{1 + (H_i - 1) \cdot S_g\} \cdot C_{i,w} \quad (12b)$$

(S_g [-]: gas saturation). Assuming ideal gas behaviour, the concentration of one component in the gas phase is related to the partial pressure of the component by:

$$C_{i,g} = \frac{p_i}{R_g \cdot T}, \quad (13)$$

where p_i [Pa] is the partial pressure of component i , R_g [kPa l/mol K] the universal gas constant and T [K] is the absolute temperature. The partial pressure can in addition be expressed as function of the total concentration C_i by:

$$p_i = \frac{C_i \cdot H_i}{1 + \left(\frac{H_i}{R_g \cdot T} - 1 \right) \cdot S_g}. \quad (14)$$

If C_i of all components i is known and mass conservation taken into account, the partial pressure and the gas saturation of the components can be calculated for a multi-component system with the help of a numerical solution. Thereby, the analysis is restricted to the 1D-case. Then the mass flux j of component i yields:

$$j_i = q_w \cdot C_{i,w} = \frac{q_w \cdot C_i}{1 + \left(\frac{H_i}{R_g \cdot T} - 1 \right) \cdot S_g} \quad (15)$$

(q_w [m/d]: water flux or Darcy velocity).

The simplifications of the local-equilibrium approach applied by Cirpka & Kitanidis (2001) are only justified if the mass transfer occurs fast compared to the water flow and is therefore only applicable to very slow groundwater flow conditions together with high concentration gradients (fast mass transfer) between a trapped gas and a mobile aqueous phase. Since the dissolution of a trapped gas phase generally is a rather fast process, the local-equilibrium approach may be a good approximation to describe the experiments performed in this work. Moreover, the mathematical complexity is low in contrast to a kinetic theory, since only the Henry's law constant is needed for calculation of the mass transfer.

3.1.2 Kinetic Approach

The kinetic model used in this work was developed by Geistlinger et al. (2003) and considers a variable gas volume (variable volume model VVM). It assumes that the mass transfer between a trapped oxygen gas bubble and the adjacent water is determined by diffusive and advective transport in the flowing water phase. The model concerns multi-components, which means that it accounts not only for the dissolution of oxygen in the water phase, but also for gases already dissolved in the water phase and their contribution to the mass transfer. The VVM is restricted to the 1D-case.

During the dissolution of an injected oxygen gas phase, the already dissolved gases partition into the gas bubbles. The emerging gas phase consists of multiple components. The concentrations [mol/l] of the i -th component in the gas and water phase, respectively, are defined as follows:

$$C_{i,g} = \frac{N_{i,g}}{V_g}, \quad C_{i,w} = \frac{N_{i,w}}{V_w} \quad (16)$$

($N_{i,g/w}$ [mol]: mol number). Under ideal conditions the partial pressure p_i is related to the concentration of one component in the gas phase by Equation 13 and according to Dalton's law the gas pressure p_g [Pa] is given by the sum of the partial pressures:

$$p_g = \sum_i p_i = \sum_{i \neq H_2O} p_i + p_{H_2O} = \tilde{p}_g + p_{H_2O} \quad (17)$$

(p_{H_2O} [Pa]: water vapour pressure, \tilde{p}_g [Pa]: reduced gas pressure). At the phase boundary area mechanical equilibrium can be assumed:

$$p_g = p_w + p_c, \quad (18)$$

where p_w [Pa] is the water phase pressure and the capillary pressure p_c is given by Laplace's law (Equation 4). The interphase mass transfer of component i is described by the mass flux j_i across the interface:

$$j_i = \beta_i \cdot \left(\frac{C_{i,g}}{H_i} - C_{i,w} \right), \quad (19)$$

and the specific mass transfer rate $R_{i,w}$ [kg/l s] assuming a first order kinetic (Donaldson et al., 1997):

$$R_{i,w} = \left(\frac{A_g}{V} \right)^* \cdot j_i = k_i \cdot \left(\frac{C_{i,g}}{H_i} - C_{i,w} \right), \quad (20)$$

where β_i [m/d] is the mass transfer coefficient of component i , $(A_g/V)^*$ [1/m] is the effective gas-water interface and k_i [1/s] the rate constant of component i . The rate constant can be split into a geometrical or structural factor – the effective gas-water interface – and a process describing factor – the mass transfer coefficient:

$$k_i = \left(\frac{A_g}{V} \right)^* \cdot \beta_i. \quad (21)$$

As discussed by Miller et al. (1990) the effective gas-water interface depends on the pore structure, saturation and flow conditions. Though the mass transfer coefficient can be derived from gas tracer experiments through inverse modeling, there will always be an uncertainty concerning the actual gas-water interface. It can either be measured through a surface-reactive tracer (Kim et al., 1997) or has to be estimated.

3.1.2.1 Estimates for the Effective Gas-Water Interface

Based on the experimental observations and the instability argument given beforehand (large coherent gas clusters are not stable), the trapped gas phase was presumed to consist of single bubbles with different bubble radii. Since the thermodynamic system tries to minimize the phase boundary area, the gas bubbles will be trapped first by the pores with the largest radii and then subsequently by the pores with smaller radii. For slightly unsaturated sediments only

the first few pore size classes are filled with gas and the gas volume can be expressed by the corresponding bubble volumes:

$$V_g = \frac{4\pi}{3} \cdot \sum_{m=1}^M N_b^m \cdot (r_b^m)^3, \quad (22)$$

where for the bubble radii r_b [m] holds:

$$r_b^1 > r_b^2 > \dots > r_b^M, \quad (23)$$

and where the numbers N_b^m can be estimated by the pore size distribution. Knowing N_b^m the gas-water interfacial area A_g [m²] can be obtained:

$$A_g = \sum_{m=1}^M N_b^m \cdot A_b^m \quad (24)$$

(A_b^m [m²]: surface area of a single bubble of class m). Powers et al. (1991) discuss the influence of different NAPL-blob shapes on mass transfer. They estimated the specific effective interface of a single blob or bubble through

$$\left(\frac{A_b}{V}\right)^* = \kappa \cdot \left(\frac{A_b}{V_b}\right) \cdot S_g, \quad (25)$$

where V_b [m³] is the volume of a bubble and κ [-] is the fraction of bubble surface area exposed to mobile water.

Predictions of the mass transfer across phase interfaces under flow conditions are rather difficult, a consequence of the complex geometry involved (Cussler, 1997). Applying the concept of advective-diffusive mass transfer, only the interface between the trapped gas phase and the mobile water phase has to be considered (Luckner & Schestakow, 1991). Holocher et al. (2003) set $\kappa = 1$ and argued that the solid surface is always covered by a thin water film. A simple and often used approximation is that this empirical factor κ can be estimated by the porosity. This approximation is also applied in the VVM.

For one bubble class the following expression for the time-dependent effective interface is obtained (Powers et al., 1991):

$$\left(\frac{A_g}{V}\right)^*(t) = \kappa \cdot \frac{3 \cdot \phi}{r_b} \cdot S_g = \kappa \cdot \frac{3 \cdot \phi}{r_b(0)} \cdot S_g^{2/3}(t) \cdot S_g^{1/3}(0), \quad (26)$$

with the time-dependent bubble radius r_b :

$$r_b(t) = r_b(0) \cdot \left(\frac{\theta_g(t)}{\theta_g(0)}\right)^{1/3}, \quad (27)$$

assuming the number of gas bubbles remaining constant during the dissolution process (ϕ [-]: porosity, θ_g [-]: volumetric gas content). The gas bubble radius and the gas saturation in

contrast are time-dependent functions. Therefore the mass transfer coefficient changes during the dissolution of a trapped gas phase, because it depends on the saturation and bubble radius through the time-dependent effective interface.

The described estimation for the effective gas-water interface has been used for the VVM. For a more elaborated model, the heterogeneity of the mass transfer process due to an inhomogeneous bubble size distribution has to be taken into account (Haggerty & Gorelick, 1995).

3.1.2.2 Conceptual Models of the Mass Transfer Coefficient

A common concept of many mass transfer theories in the literature is that the mass flux between two phases is a function of a driving force like the concentration difference between the two phases of concern and a mass transfer coefficient (Treybal, 1980; Miller et al., 1990; Cussler, 1997; Donaldson et al., 1997; Holocher et al., 2003):

$$j_i = \beta_i \cdot \Delta C_i, \quad (28)$$

where ΔC_i [kg/m³] is the concentration gradient. There are different approaches to determine the mass transfer coefficient.

Many of the existing models for the dissolution of a gas phase are based on the stagnant film model first suggested by Nernst in 1904. In this model the mass transfer between a trapped gas bubble and the adjacent water is determined by the diffusive transport of the gas through a thin stagnant water film surrounding the gas bubble (Gulliver, 1990; Cussler, 1997; Donaldson et al., 1997; Holocher et al., 2003) (Figure 6). The concentration gradient in the film is linear (Figure 6) and at equilibrium across the interface (Gulliver, 1990). Then, the mass transfer coefficient can be described as a ratio between the diffusion coefficient and the film thickness (Cussler, 1997):

$$\beta_i = \frac{D_{i,w}}{d_w} \quad (29)$$

($D_{i,w}$ [m²/d]: diffusion coefficient for component i in water, d_w [m]: thickness of the water film). According to this model, the mass transfer coefficient is directly proportional to the diffusion coefficient thus seeming to be an appropriate assumption. Consequently, the mass transfer coefficient shows a species dependency since the diffusion coefficient is varying for different components. For the components used in this work the diffusion coefficient is well studied. A detailed discussion of the stagnant-film model can be found at Schwarzenbach et al. (2002).

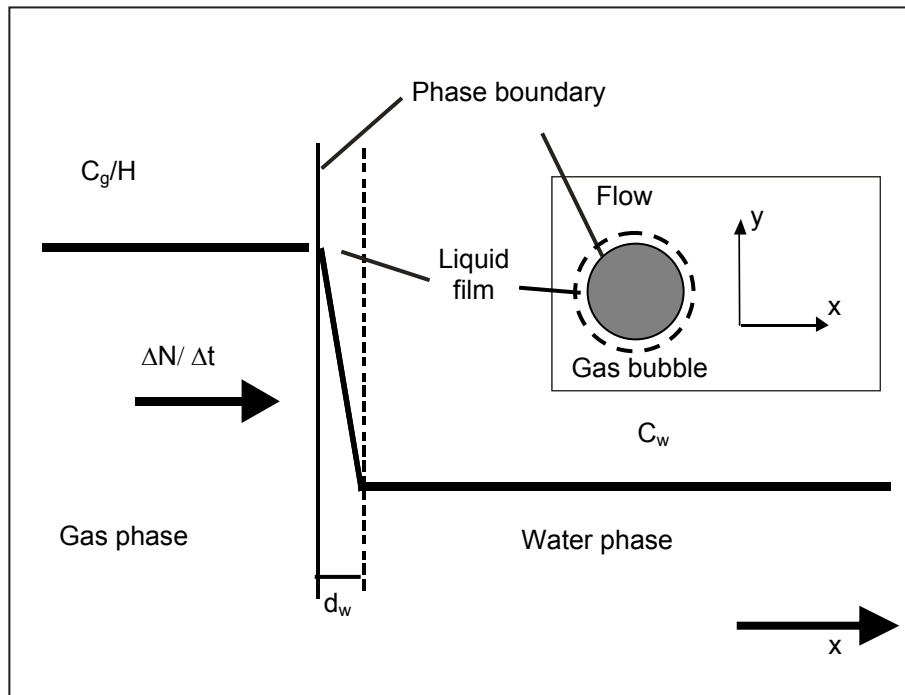


FIGURE 6: Stagnant film model (after Cussler, 1997).

In case of no flow, the microscopic mass transfer coefficient for a spherical gas bubble based on the stagnant film model is given by the stationary solution of the diffusion equation (Schwarzenbach et al., 2002):

$$\beta_i = \frac{D_{i,w}}{d_{\text{eff}}} = D_{i,w} \cdot \left(\frac{1}{r_b} + \frac{1}{d_w} \right) \quad (30)$$

(d_{eff} [m]: effective film thickness).

In case of flow the stagnant film theory is not the best conceptual model (Gulliver, 1990). According to Cussler (1997), a stagnant water film around a gas bubble is almost always hypothetical, for fluid motions commonly occur right up to even a solid interface (Campbell & Hanratty, 1982; Miller et al., 1990). The film thickness is continually changing with time and is advected with the surface velocity (Gulliver, 1990). Moreover, the mass transfer coefficient varies in some unknown fashion with variables like fluid viscosity and velocity, because these variations are lumped into the unknown film thickness (Cussler, 1997).

The surface renewal theory (Dankwerts, 1951) provides a better physical picture of mass transfer from gas bubbles into a moving water phase than the film theory and at the same time the increase in mathematical complexity is low. It is a conceptual expansion of the penetration theory developed by Higbie in 1935 (after Gulliver, 1990). The classical penetration theory is

valid for rigid spherical bubbles (Nedeltchev, 2003). The concept of the surface renewal theory is that the fluid on the surface is periodically renewed by the bulk fluid. Although the film still exists at the interface, its thickness varies over time and space (Figure 7). The surface renewal theory states that the frequency of renewal is more important in gas-water mass transfer than the film thickness.

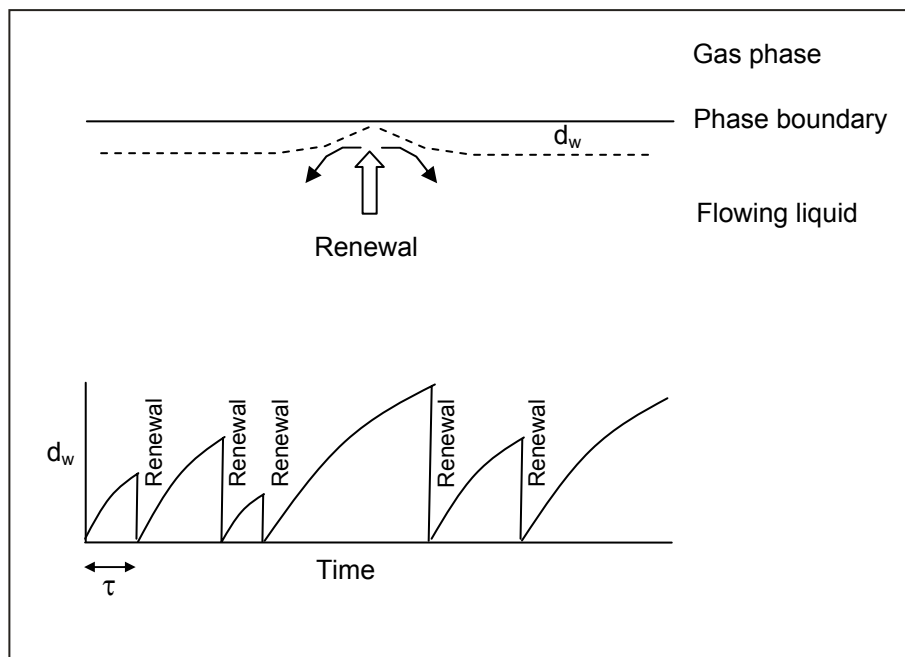


FIGURE 7: Conceptual sketches of surface renewal on the water side of the interface (above) and of the film thickness at one location over time (below) as assumed by the surface renewal theory (after Gulliver, 1990).

Mass transfer involves diffusion into this film with varying thickness. The interfacial concentration in the liquid is assumed to be in equilibrium with that of the gas. Within the gas bubble, mixing processes in the gas phase are fast and therefore the gas phase can be described as homogeneous. According to Miller et al. (1990), the mass transfer near the interface of the gas and water phase is the combined result of an advective and a diffusive process. The surface renewal model assumes that in direction perpendicular to the flow direction, diffusion is much more important than advection whereas in flow direction, diffusion is much less important than advection.

Considering the surface renewal theory, the film thickness d_w can be estimated by the following equation, assuming that the penetration length of a gas molecule into the water phase can be approximated by the diffusion length:

$$d_w \approx \sqrt{D_{i,w} \cdot \tau} = \sqrt{\frac{D_{i,w} \cdot \pi \cdot r_b}{u_w}}, \quad (31)$$

where τ [s] is the contact time (i.e. the time interval for surface renewal) and u_w [m/d] the flow velocity of water. Inserting (31) into (30) one obtains a first approximation for the velocity dependency of the mass transfer coefficient (square root velocity dependency, Levich, 1962; contact time model, Holocher et al., 2003):

$$\beta_i = D_{i,w} \cdot \left(\frac{1}{r_b} + \sqrt{\frac{u_w}{\pi \cdot r_b \cdot D_{i,w}}} \right). \quad (32)$$

Therefore, the mass transfer coefficient shows a velocity dependency due to the contact time between the gas and water phase (Figure 8).

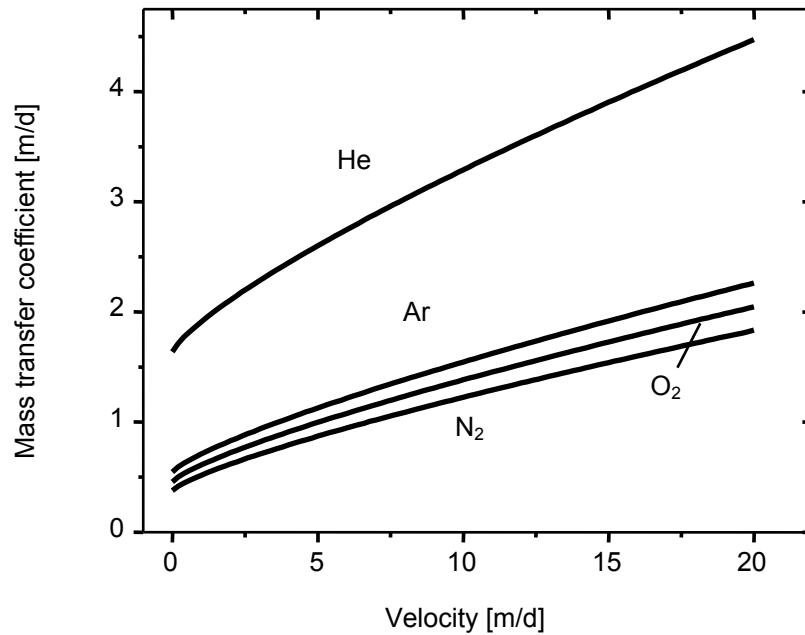


FIGURE 8: Velocity dependency of the mass transfer coefficient for different gases according to the empirical Sherwood correlation (Equ. 33 and 34).

Equation 32 can be written in terms of dimensionless numbers (Cussler, 1997). The mass transfer coefficient can be expressed using a Sherwood number parameterization:

$$\beta_i = \frac{Sh_i}{2 \cdot r_b} \cdot D_{i,w} \quad (33)$$

(Sh_i [-]: Sherwood number of component i). The result is a dependency of the mass transfer coefficient from dimensionless numbers since the Sherwood number (dimensionless mass

transfer coefficient) can be expressed in terms of the Reynolds number Re [-] and Schmidt number Sc [-] (shown in generalized form (Romkes et al., 2003)):

$$Sh = a_1 + a_2 \cdot Re^y \cdot Sc^z. \quad (34)$$

The factors a_1 and a_2 as well as the power of the dimensionless numbers will change depending on the investigated system. The characteristics of the dimensionless numbers are given in Table 2. The Sherwood number involves the mass transfer coefficient itself, the Schmidt number involves diffusion and the Reynolds number describes the flow. For advective-diffusive mass transfer the Sherwood number can also be considered as a function of the Peclet number Pe [-]:

$$Sh = f(Pe^y), \text{ where } Pe^y = Re^y \cdot Sc^y. \quad (35)$$

TABLE 2: Significance of dimensionless numbers for typical groundwater conditions: $u = 1 - 10$ m/d and bubble diameter $d_b = 0.1 - 1.0$ mm (after Cussler, 1997).

Group	Formula	Physical meaning	Used in
Sherwood number	$Sh = \frac{\beta \cdot d_b}{D_{i,w}}$	<u>mass transfer velocity</u> diffusion velocity	Usual dependent variable
Schmidt number	$Sc = \frac{\nu}{D_{i,w}}$	<u>diffusivity of momentum</u> diffusivity of mass	Correlations of gas or liquid data
Reynolds number	$Re = \frac{d_b \cdot u}{\nu}$	<u>inertial forces</u> viscous forces	Forced advection

d_b [m]: bubble diameter
 ν [m^2/s]: kinematic viscosity

3.2 Transport of Dissolved Gases and Contaminants

As soon as the gas is dissolved in the water, it will be transported, like any solute, through a porous medium by the processes of advection and dispersion. The kinetic model applied in this work assumes that the transport of a dissolved gas in a porous medium can be described by the advection-dispersion equation (Bear, 1972) (adsorption is neglected). In this advection-dispersion equation the mass transfer from a trapped gas bubble into the water phase is represented with a source/sink term accounted for by the specific mass transfer rate R_i^w . Together with a saturation-dependent flow equation the following system of partial differential equations has to be solved:

mobile water phase:

$$\theta_w \frac{\partial C_{i,w}}{\partial t} = \frac{\partial \theta_w}{\partial x} \cdot D_{i,w} \frac{\partial C_{i,w}}{\partial x} - q_w \frac{\partial C_{i,w}}{\partial x} + R_{i,w}, \quad i = 1 - k, i \neq \text{H}_2\text{O} \quad (36a)$$

immobile gas phase:

$$\theta_g \frac{\partial C_{i,g}}{\partial t} = R_{i,g} = -R_{i,w}, \quad i = 1 - (k-1), i \neq \text{H}_2\text{O} \quad (36b)$$

gas saturation:

$$\frac{\partial \theta_g}{\partial t} = \frac{-R_g T \sum_{i \neq \text{H}_2\text{O}} R_{i,w} - \rho_w \cdot g \cdot \theta_g \cdot \frac{\partial h_w}{\partial t}}{\tilde{p}_g - \frac{1}{3} \cdot p_c} \quad (36c)$$

(θ_w [-]: volumetric water content, ρ_w [kg/m³]: density of water, h_w [m WS]: pressure head in the water phase). The dissolution velocity of the gas phase (Equation 36c) depends on the transfer rates, the temporal change of the head and the capillary pressure. That means the larger the capillary pressure, the higher the dissolution velocity. In contrast to the kinetic multi-component model of Holocher et al. (2003) (steady state flow approximation) the Darcy potential ($\frac{\partial h_w}{\partial t}$ -term), which influences the dissolution process, is taken into account.

The transport is calculated for each gas component i . Consequently, for a system with two dissolved gas components, two differential equations for the water phase, two differential equations for the gas phase, and one differential equation for flow have to be solved, resulting in a system of five differential equations. Therefore, the numerical complexity of the kinetic theory is much higher compared to the local-equilibrium approach. The system of partial differential equations (Equations 36a-c) is solved in the VVM using a time-adaptive operator-splitting-method. This leads for the reaction step to a system of ordinary differential equations, which are solved by a time-step-controlled Runge-Kutta-solver (odeint-solver from Press et al., 1992).

The Darcy flux q_w is determined by the groundwater continuity equation:

$$\frac{\partial(\phi \cdot S_w)}{\partial t} = \phi \cdot \frac{\partial S_w}{\partial t} = -\frac{\partial q_w}{\partial x}, \quad q_w = -K_{f0} \cdot K_{rw}(S_w) \frac{\partial h_w}{\partial x}, \quad (37)$$

where K_{f0} [m/d] is the saturated hydraulic conductivity and K_{rw} [m/d] is the relative permeability with respect to water. For the relative permeability a van Genuchten parameterization is used (Luckner et al., 1989):

$$K_{rw}(S_w) = S_e^{1/2} [1 - (1 - S_e^{1/m})^m]^2, \quad S_e = \frac{S_w - S_r}{S^{\max} - S_r} \quad (38)$$

(S_e [-]: effective saturation, S_r [-]: residual saturation, S^{\max} [-]: maximum saturation, the exponent m is connected to the van Genuchten parameter n [-] by $m = 1 - 1/n$ (see Figure 9)).

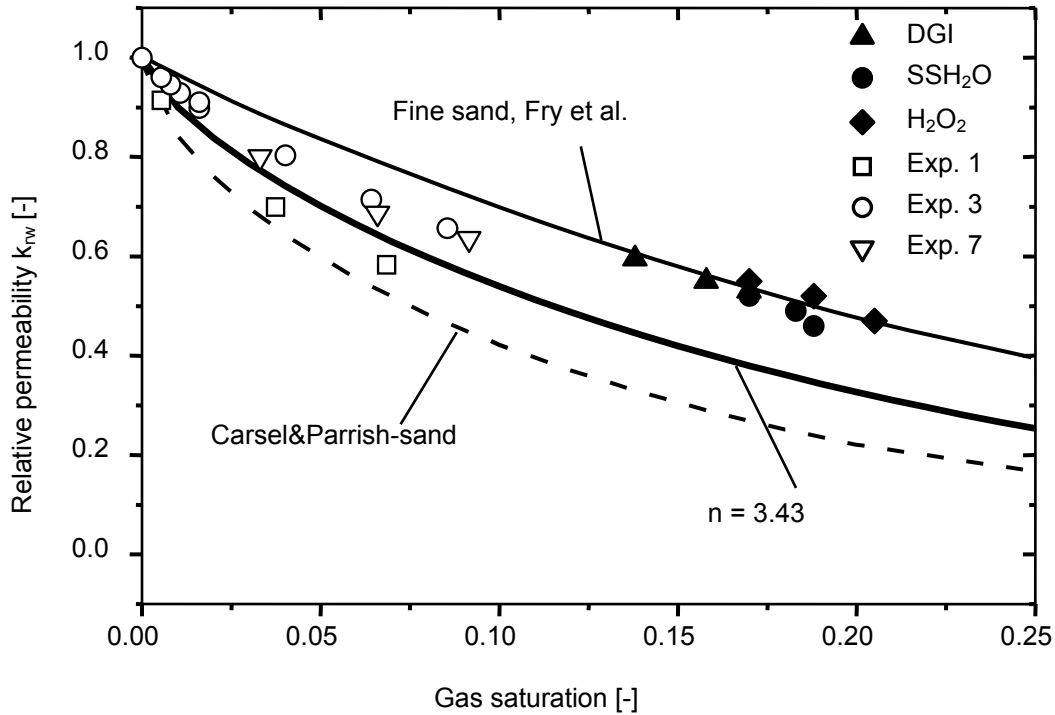


FIGURE 9: Van Genuchten parameterization of the relative permeability (Equation 44). Thick solid line: Fit to own experiments 1, 3, and 7 (van Genuchten parameter $n = 3.43$); thin solid line: Fit to the experimental values from Fry et al. (1996) ($n = 12$), DGI = direct gas injection, SSH₂O = injection of supersaturated water, H₂O₂ = injection of hydrogen peroxide solution; dashed line: Typical sand after Carsel & Parrish (1988) ($n = 2.68$) (after Geistlinger et al., 2005).

For the experiments described in this work the following boundary and initial conditions applied:

boundary conditions:

$$q_w(x = 0, t) = \text{const.}, \quad (39a)$$

$$p_w(x = L, t) = \text{const.}, \quad (39b)$$

$$C_{O_2,w}(x = 0, t) = 0, \quad (39c)$$

$$C_{i,w}(x = 0, t) = \text{const.}, \quad i = \text{He, Ar, N}_2, \quad (39d)$$

initial conditions:

$$\theta_g(x, t = 0) = \text{const.}, \quad (40a)$$

$$C_{O_2,w}(x, t = 0) = \frac{C_{O_2,g}(x, t = 0)}{H_{O_2}}, \quad (40b)$$

$$C_{i,w}(x, t = 0) = \frac{C_{i,g}(x, t = 0)}{H_i} = 0, \quad i = \text{He, Ar, N}_2 \quad (40c)$$

(L [m]: column length). Equation 40c is a form of the so-called Danckwerts boundary condition (Pearson, 1959 after Donaldson et al., 1997) that has been shown to be an accurate outlet boundary condition for use with the advection-dispersion equation to describe the results of laboratory column experiments.

3.3 Comparison of Different Kinetic Models used for Inverse Modeling

In the literature an analytical solution of a kinetic one-component approach (in the following referred to as constant volume model (CVM)) is often used in order to determine mass transfer coefficients from integral information, for example from breakthrough or elution curves. Donaldson et al. (1997) developed this simplistic kinetic model to describe the transport of dissolved gases in the water phase in the presence of small amounts of trapped gas in porous media. Their model is based on the stagnant film model and assumes that the volumetric gas content is constant during the transport process ($\theta_g = \text{const.}$). This assumption simplifies the system of partial differential equations (Equation 36a-c), since flow and transport decouple and the volumetric gas content θ_g and the pressure head h_w become time-independent. They performed transport experiments and injected a pulse of oxygen-saturated water into partially water-saturated sediment-filled columns containing different residual gas phases: Air, nitrogen or helium. They used an analytical solution of the CVM for the interpretation of their experiments. The model results fitted the shape of their experimental oxygen breakthrough curves well.

Vulava et al. (2002) also used an analytical solution of the CVM for the interpretation of partitioning gas tracers. The authors used a combined Kr-SF₆-partitioning gas tracer test to determine gas saturation and partitioning rates in laboratory columns under partially water-saturated conditions. They injected a tracer solution containing approximately 130 mg/l Kr and 1 mg/l SF₆ into a column that was partially saturated with air. The model accurately described the tracer breakthrough curves.

In both cases, a multi-component system was described by a one-component theory. Only the interphase mass transfer from the dissolved gas transported by the water phase was considered. However, as was stated before the gas partitioning of all gas components in the system is coupled, so that the behaviour of a single gas component cannot be considered independently of the others. Moreover, the CVM contains the assumption that the gas saturation is constant during the transport process, though the transfer of the different gas

components out of or into the bubble will be varying – depending on their varying diffusion coefficient – so that the gas phase volume will change. However, in both experiments described above the changes in the gas saturation were small and the assumption of constant volume may be justified.

To answer the question if the CVM can also be used to describe the dissolution of gas bubbles in a mobile water phase, a comparison between different solutions of the CVM and the quasi exact numerical solution of the VVM was carried out (Figure 10) (Geistlinger et al., 2005). As a test case a two-component system was considered: The dissolution of a trapped oxygen gas phase, where the by-passing water is completely saturated with nitrogen. The elution curves in Figure 10 were calculated using a parameter set similar to that used in the experiments of this work: porosity $\phi = 0.376$, gas saturation $S_g = 0.08$, longitudinal dispersivity $\alpha_1 = 2$ mm, gas bubble radius $r_b = 0.3$ mm, water flux $q_w = 6.25$ m/d, mass transfer coefficient of oxygen $\beta_{O_2} = 1.78$ m/d, mass transfer coefficient of nitrogen $\beta_{N_2} = 1.59$ m/d, $n = 3.43$.

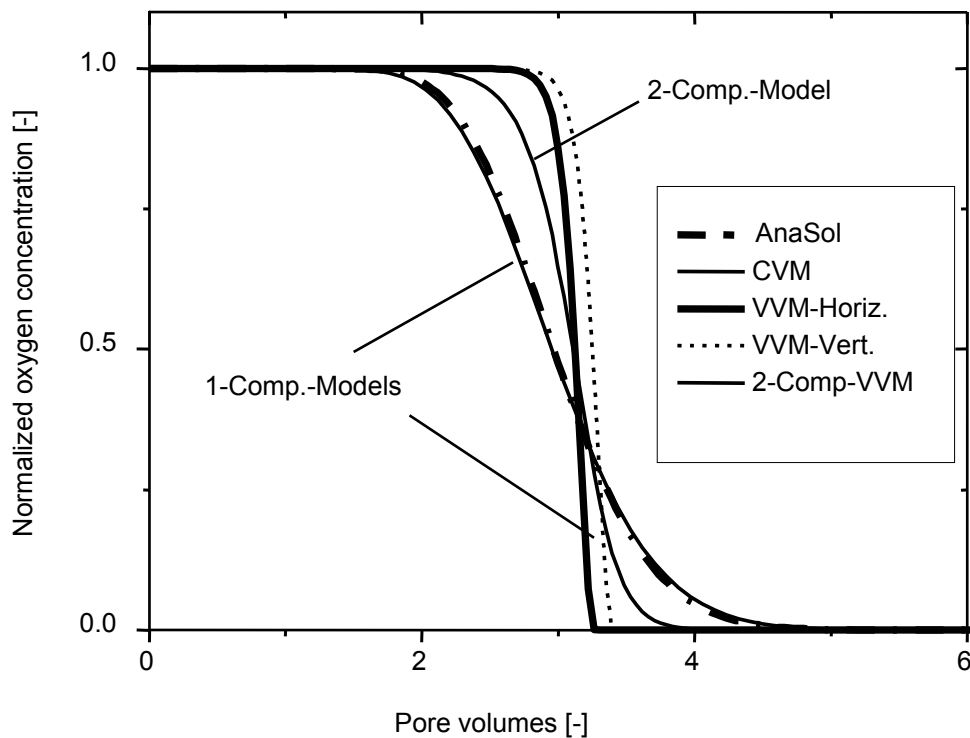


FIGURE 10: Comparison of the CVM- and VVM-elution curves for the dissolution of a trapped oxygen gas phase (after Geistlinger et al., 2005).

At first the horizontal case (flow in horizontal direction, no gravitational effects) was considered and described by one-component models. To understand the impact of the inherent assumptions made by an analytical treatment, an analytical solution of the CVM (thick dashed line in Figure 10) was compared with a numerical solution of the CVM (left thin solid line). There is only a slight deviation between the analytical and the numerical solution, which can be considered as a good test of the operator-splitting method. In addition, the one-component analytical and numerical solution of the CVM was compared with a one-component numerical solution of the VVM (thick solid line). The most important characteristic of the CVM is its less steep decrease of the elution curve, i.e. a slower dissolution of the gas phase, compared to the very steep decrease of the exact solution of the VVM. This is a direct result of the assumption inherited in the CVM that the gas volume is constant during the dissolution process. It leads to a decreasing partial oxygen pressure caused by a decreasing number of oxygen mols in the gas phase and a slowed down dissolution process. Physically, the oxygen pressure must remain nearly constant, because it is given by the hydrostatic pressure, leading to the steep decrease of the VVM-elution curve.

Secondly, the one-component numerical solutions of the CVM and VVM were compared with a two-component numerical solution of the VVM (right thin solid line) still considering the horizontal case. It is obvious that the two-component VVM-elution curve must exhibit a less steep decrease – meaning a slower dissolution – than the one-component VVM-elution curve, since the nitrogen transfer from the water to the gas phase reduces the partial oxygen pressure and therefore decreases the driving force of the oxygen mass transfer; the concentration gradient. It is remarkable that the decrease of the CVM-elution curve is even more pronounced than the decrease of the two-component VVM-elution curve. However, the less steep decrease of the CVM-elution curve is a result of the simplistic constant volume assumption and not based on real physical processes. Hence, the application of the CVM for the description of the dissolution process of a trapped gas phase is rather questionable. Its use to determine the mass transfer coefficients from integral information can lead to errors in this case. Another less pronounced effect of the CVM is that the decrease of the normalized oxygen concentration starts earlier for the one-component CVM-curve than for the two-component VVM-curve. This is because the velocity in the CVM is calculated accounting for the maximal (initial) gas saturation (steady-state solution of the flow equation).

Finally, the vertical case (flow in vertical direction, including gravitational effects) was considered. A one-component numerical solution of the VVM for the vertical case is shown in Figure 10 (thin dashed line). For the horizontal case the dominating contribution to the gas

pressure results from the hydrostatic pressure (the capillary pressure is neglected), thus an assumption of homogeneous initial conditions is justified. In the vertical case the analytical solution will fail, since an inhomogeneous hydrostatic pressure– linear increase with depth – will result in an inhomogeneous partial oxygen pressure distribution along the column.

In conclusion, the multi-component numerical VVM should be used to describe the dissolution process of a trapped gas phase, since it is based on a more realistic physical picture than the CVM. An important feature of the VVM is its saturation dependency. Moreover, a multi-component model has to be used for the interpretation of the experiments described in this work, since the injection of a one-component gas phase in a real aquifer, which contains dissolved gases, always leads to a multi-component mass transfer process.

4. Laboratory Experiments

The objective of the laboratory column experiments was to investigate the dissolution of a trapped oxygen gas phase and its interaction with dissolved gases in the water phase under aquifer near conditions. To achieve these conditions, a special column design was created. The main achievement was an artificial application of a sediment overburden. As fixed boundary conditions, a constant water flow was established at the column entrance and a fixed hydrostatic pressure was applied at the column exit. Moreover, the whole experimental set up was placed in a constant temperature room at 10 °C reflecting the general temperature conditions in natural aquifers (Ellis et al., 2000). Temperature variations were in the order of 1 °C. A range of water flow velocities was applied in different experimental test series trying to adjust aquifer typical flow velocities of about 1 – 10 m/d. To minimize experimental uncertainties, all experiments were repeated as a matter of principle.

Pure oxygen gas was injected into a column filled with sediment and the dissolution of the gas phase was observed. For the model application it was essential to accurately determine the initial gas saturation. This was achieved by determining the saturation state of the column by three independent methods: By gravimetric measurements, by consecutive bromide tracer tests, and by hydraulic conductivity measurements. For the dissolution of the oxygen gas phase flow through the column was performed with an almost oxygen free flushing solution. This flushing solution was produced by fully saturating water with a flushing gas. In a first test series, the different effects of these flushing solutions on the oxygen dissolution were detected by the use of varied flushing gases (helium, nitrogen or argon). In a second test series, experiments were conducted with a chosen flushing solution at decreased water flow velocities. Altogether, ten dissolution experiments were performed (Table 3).

TABLE 3: Summary of the dissolution experiments.

Test series	Number of experiment	Flushing gas	Velocity ¹ [m/d]
1	1 and 2	He	17
1	3 and 4	N ₂	17
1	5 and 6	Ar	17
2	7 and 8	N ₂	9
2	9 and 10	N ₂	4

¹ calculated for the saturated state (ϕ_{tot})

4.1 Design of the Laboratory Column

4.1.1 Dimension of the Column and Sand Properties

The laboratory experiments were performed using a packed sand column. The column had a length of $0.942 \text{ m} \pm 0.001 \text{ m}$ and an inner diameter of $2.14 \text{ cm} \pm 0.01 \text{ cm}$ and was made of transparent PVC (Table 4). It was filled with sand classified as pleistocene quartz sand at medium grain size, on which dry grain size distribution analyses were performed (Appendix 2.1 and 2.2). The grain size range lay between $0.125 - 0.6 \text{ mm}$, the median grain diameter d_{50} [mm] determined by sieving was 0.3 mm . The uniformity coefficient U [-] was 2. Furthermore, the hydraulic conductivity K_f was estimated from the grain size analyses using an empirical equation after Hazen:

$$K_f = C \cdot d_{10}^2, \quad (41a)$$

$$C_H = (0.7 + 0.03 \cdot T) / 86.4, \quad (41b)$$

where C_H [1/s·mm] denotes for a temperature-dependent empirical coefficient, d_{10} [mm] represents the particle size, relative to which 10 percent of the sample is finer and T [°C] for the temperature. For the sediment used in the column a hydraulic conductivity of $3.75 \cdot 10^{-4} \text{ m/s}$ was calculated from the grain size distribution (Appendix 2.1 and 2.2).

The sand was well sorted. The particle density ρ_s [g/cm³] of the sand, determined by helium pycnometry, was 2.7 g/cm^3 . The determination of the specific surface A_i [m²/g] resulted from the BET-method, in which the amount of nitrogen adsorbed at the grain surface is detected. This measuring method has a high resolution, at which the resolution is limited through the diameter of a nitrogen molecule. The roughness of all single particles is recorded. By this method a specific surface of $0.597 \text{ m}^2/\text{g}$ was determined for the sand. The specific surface of a sediment is a measure for the contact area between sediment particles and water and therefore relevant for the permeability towards the water phase. A high specific surface has a reducing impact on the hydraulic conductivity.

The column was packed in the manner that the dry sand was filled into the column and slightly consolidated (dry tamping). The dry mass of sand M_s [g] added was $570.76 \text{ g} \pm 2 \text{ g}$. It was determined after all experiments were finished by removing the sand, drying and weighting it. The column volume V_{col} [cm³] was also determined after all experiments were completed by filling the empty column with water and determining the volume of the water body over its mass and density. This method resulted in a column volume of $338.95 \text{ cm}^3 \pm 0.5 \text{ cm}^3$. The dry mass of the sand and the column volume were used together with the particle

density – determined by helium pycnometry – to calculate the bulk density ρ_b [g/cm³] and the total porosity ϕ_{tot} [-] of the packed column:

$$\rho_b = \frac{M_s}{V_{\text{col}}}, \quad (42a)$$

$$\phi_{\text{tot}} = 1 - \frac{\rho_b}{\rho_s}. \quad (42b)$$

The bulk density is the ratio of the mass of soil to its total volume (solids and pores together), which is in this case the column volume. The employed packing method resulted in a bulk density of $1.684 \text{ g/cm}^3 \pm 0.008 \text{ g/cm}^3$. The total porosity was 0.376 ± 0.003 . The same sediment was used in all experiments performed in this work.

TABLE 4: Relevant parameter of the sediment-filled column generally applicable to all experiments.

Parameter	
Sediment type	medium sand
Medium grain diameter d_{50} [mm]	0.3
Uniformity coefficient U [-]	2
Hydraulic conductivity K_f [m/s]	$3.75 \cdot 10^{-4}$
Particle density ρ_s [g/cm ³]	2.7
Specific surface A_i [m ² /g]	0.597
Dry mass of sediment M_s [g]	570.76 ± 2
Bulk density ρ_b [g/cm ³]	1.684 ± 0.008
Total porosity ϕ_{tot} [%]	37.6 ± 0.3
Column length L [cm]	94.2 ± 0.1
Column diameter d_{col} [cm]	2.14 ± 0.01
Column volume V_{col} [cm ³]	338.95 ± 0.5

4.1.2 Dynamical Compression of the Sediment

Preliminary experiments had shown that in uncompressed, but densely packed sediments gas injection leads to air channelling and preferential flow paths (Figure 11). Similar observations were made during column experiments performed by Weber (2000). To avoid the formation of preferential flow paths in following experiments, the sediment was dynamically compressed inside the column to achieve a stable grain structure.

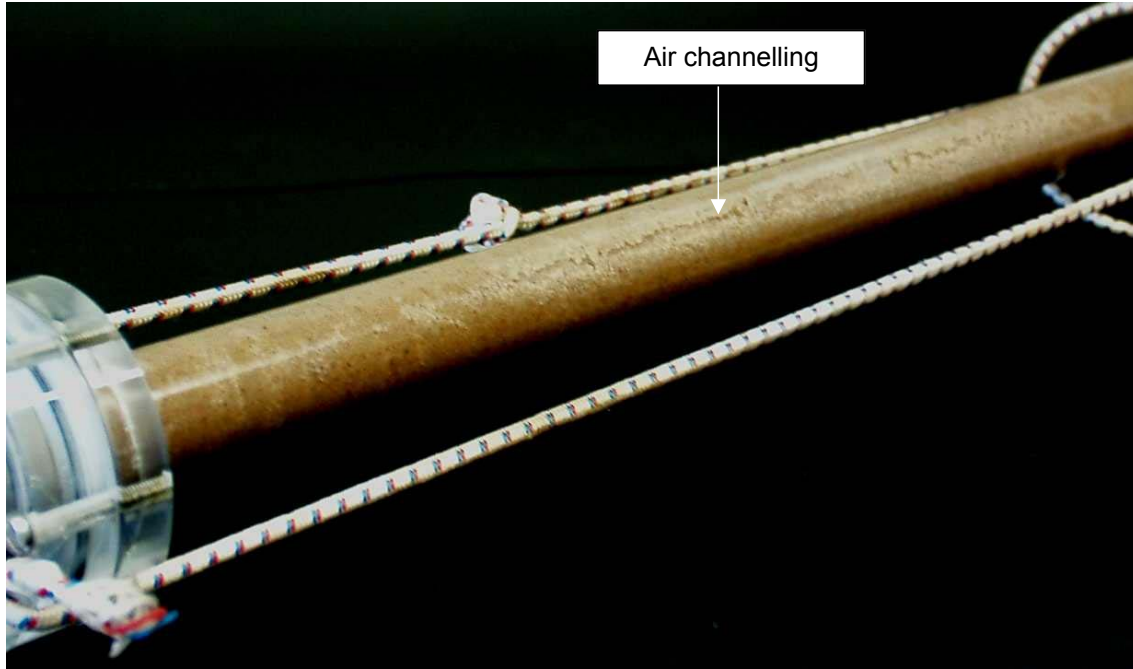


FIGURE 11: Channelling that has arisen in uncompressed sediments during direct gas injection.

In Figure 12 the construction of the symmetrical column is illustrated. The column consisted of two PVC parts that were linked by a sleeve made of acrylic glass. In the sleeve both column parts were connected by a telescope device made out of thin aluminium cylinders. The mounting of the column parts in the sleeve was realized by greased sealing rings. This permitted their axial movement, whereby only slight friction forces had to be overcome. By this structure, an axial load applied on the column ends through a clamping device (Figure 13) was essentially transferred as tension to the sediment. A pressure of approximately 0.3 MPa was applied on the sediment (measured by a pressure sensor connected to the clamping device). This pressure can be related to the lithostatic pressure p_l [Pa], which is the pressure of the weight of overburden, or overlying rock, on sediment. Then the corresponding depth or thickness of overburden h_o [m] can be calculated by:

$$h = \frac{p_l}{\rho_s \cdot g}, \quad (43)$$

where ρ_s [kg/m^3] is the density of the overlying sediments and can be estimated by the particle density determined for the sediments used for this work. This results in an overburden of about 11 m (dry sediment) for the column design used in this work. Due to the small column diameter, high tension could be applied on the sediment with the help of only small forces.

At both ends the column parts were locked by specially designed column caps (LAZIK, 1998) (Appendix 3.1, 3.2 and 3.3) that were likewise sealed with greased rings. Inside the column

caps an inlet distributor made out of coarse meshed fleece material provided uniform axial flow of the water within the sediment over the whole column diameter and at the same time retained the sand particles and prevented their intrusion into the inlet tube.

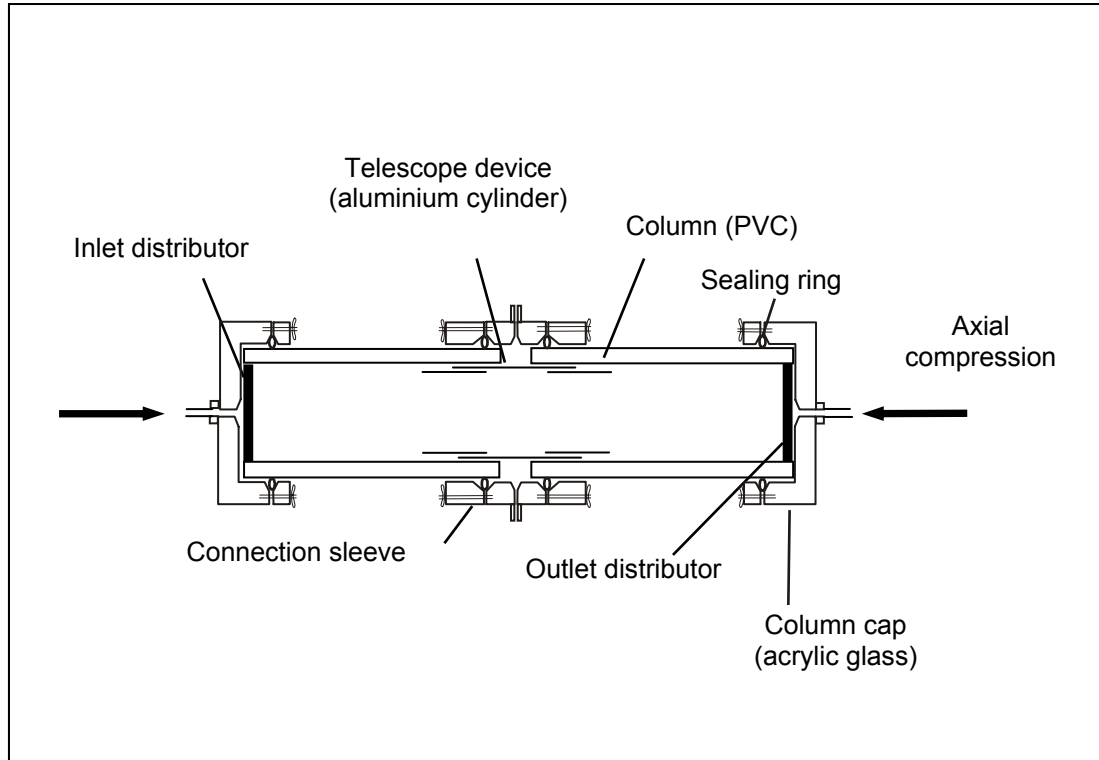


FIGURE 12: Schematic construction of the column. An axial compression is applied on the column ends through a clamping device.

4.2 Experimental Setup

The entire experimental setup was composed of the following components (Figure 13):

- gravimetric unit, consisting of glass bottles and balances
- sand-filled, dynamically compressed column (Figure 14)
- clamping device
- bromide and oxygen sensors, pressure transducers
- two 4-channel peristaltic pumps.

In preparation for the experiments the column was fixed in a vertical position and a constant upward water flow into the column could be realized through a constant pumping rate using a peristaltic pump (Figure 13). The test solutions pumped into the column were stored in glass bottles placed on a balance near the inflow of the column (balance 1).

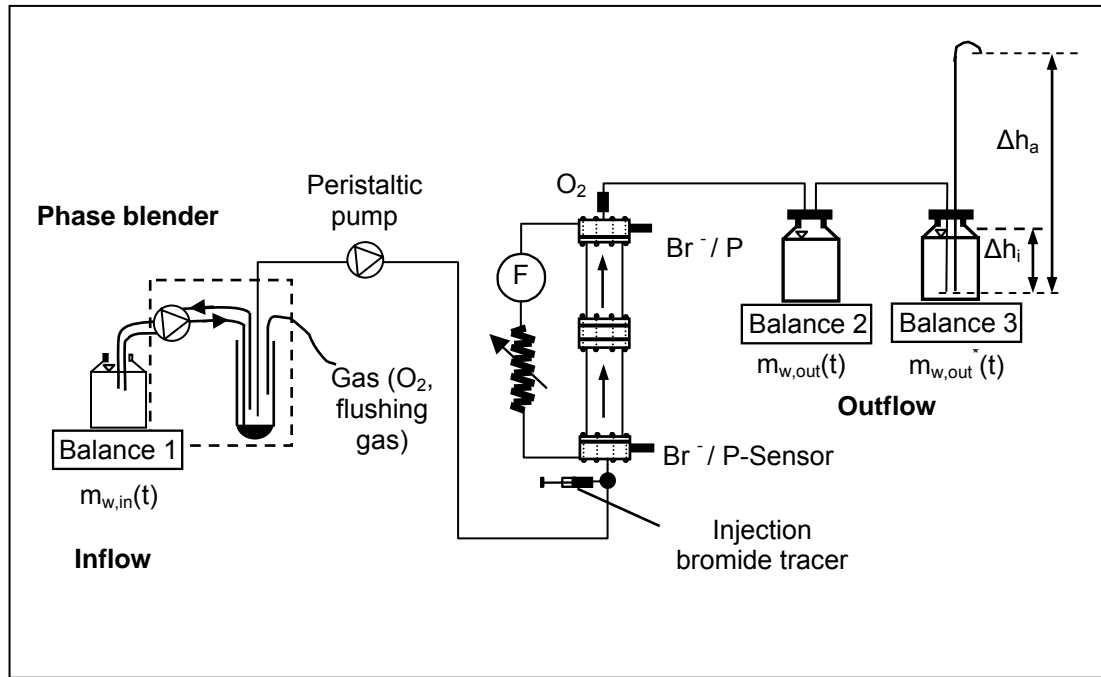


FIGURE 13: Experimental set up. The gravimetric measuring system contains three balances: One inflow-balance and two outflow-balances. A phase blender regulates a specified gas-water flow. The column is dynamically compressed through a clamping device. The inflow column cap contains a bromide sensor and a pressure transducer. The outflow column cap additionally contains an oxygen sensor.

The water supply was designed in the manner that a concurrent injection of gas and water could take place over a single injection port at the inlet of the column. Thereby, a uniform, small-volume mixing of gas and water was achieved in a phase blender. From this phase blender the water was pumped into the column with a second peristaltic pump. The water flowing out of the column was collected in another glass bottle also placed on a balance (balance 2). This glass bottle is coupled to a third water filled glass bottle on balance 3 (Figure 14) to determine the gas flow out of the column. As a fixed boundary condition, an artificial hydrostatic pressure h_a of approximately 7 kPa was applied on the column outlet in order to prevent gas accumulation at the top of the column. Special efforts were taken to make the experimental setup gas-tight and minimize gas losses due to gas diffusion. Therefore, tubing made out of polyethylene with low oxygen permeability was used to connect the column with the glass bottles containing the test solutions. All connections were with quick-couplings.

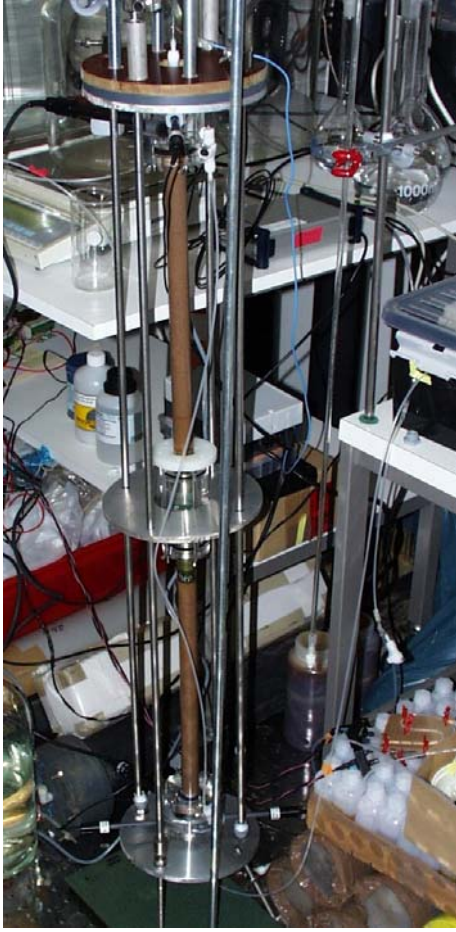


FIGURE 14: Sand-filled, dynamically compressed symmetrical column (left), computer based data recording in the outlet of the column (right).

4.3 Measurement and Control Technology

4.3.1 Gravimetric Measurements

A gravimetric recording of the water flow into and out of the column was accomplished for each experiment. The principle of this measuring method is the determination of the water and gas volume by the mass and density of an incompressible fluid (water). Therefore, the continuous water mass decrease on balance 1 and the water mass increase on balance 2 was measured (Figure 13). The reproducibility of the balances is about 0.01 g, which corresponds to a water volume of 0.01 ml. Since a closed water system was used, the total water mass remained constant during the entire experiment: $m_{\text{tot}} = \text{constant}$. By measuring the water mass decrease on balance 1 the water flow into the column was determined by:

$$\Delta V_{w,\text{in}}(t) = \frac{\Delta m_{w,\text{in}}(t)}{\rho_w}, \quad \Delta m_{w,\text{in}}(t) = m_{w,\text{in}}(t_0) - m_{w,\text{in}}(t), \quad (44a)$$

$$Q_{w,\text{in}}(t) = \frac{\Delta V_{w,\text{in}}}{\Delta t}, \quad (44b)$$

where $\Delta V_{w,in}(t)$ [cm^3] is the water volume pumped into the column, $\Delta m_{w,in}(t)$ [g] the amount of water loss measured on balance 1, Δt [s] the considered time interval and ρ_w [g/cm^3] is the density of water. The Darcy velocity can be determined by:

$$q_w = \frac{Q_{w,in}(t)}{A_{col}} \quad (45)$$

(A_{col} [cm^2]: cross-sectional area of the column). The water flow out of the column can be determined equivalently by:

$$\Delta V_{w,out}(t) = \frac{\Delta m_{w,out}(t)}{\rho_w}, \quad \Delta m_{w,out}(t) = m_{w,out}(t) - m_{w,out}(t_0), \quad (46a)$$

$$Q_{w,out}(t) = \frac{\Delta V_{w,out}}{\Delta t} \quad (46b)$$

($\Delta V_{w,out}(t)$ [cm^3]: water volume pumped out of the column, $\Delta m_{w,out}(t)$ [g]: amount of water gain measured on balance 2). Assuming that the total porosity and the total volume of the system is constant, the gas volume in the column can be determined by balancing the volume of the water pumped into the column and the volume of the water pumped out of the column. The gas volume injected into the column will displace an equivalent water volume in the column. The change in gas volume in the column ΔV_g [cm^3] can be computed by:

$$\Delta V_g(t) = \frac{(\Delta m_{w,out}(t) - \Delta m_{w,in}(t))}{\rho_w} \quad (47)$$

Under steady-state conditions the flow into the column must be the same as the flow out of the column: $Q_{w,in}(t) = Q_{w,out}(t)$. However, slightly different errors of the two balances led to a small deviation between the in- and outflow. This linear drift between the balances was determined for each experiment at the steady-state condition before the gas injection ($\Delta V_g(t) = 0$) and corrected (Figure 15). In Figure 15 a small jump in the temporal development of the gas volume can be seen at the steady-state plateau that was reached after the end of the gas injection. This jump is caused by the injection of 1 ml bromide solution for the bromide tracer tests. The gravimetric system was sensitive enough to record the total mass increase by 1 g. In contrast, the small oscillations in the residual gas volume displayed in Figure 15 are because there was no continuous water flow into the glass bottle on balance 2, but the water dropped periodically into the bottle. Nevertheless, the total mass had to be corrected by the bromide tracer mass.

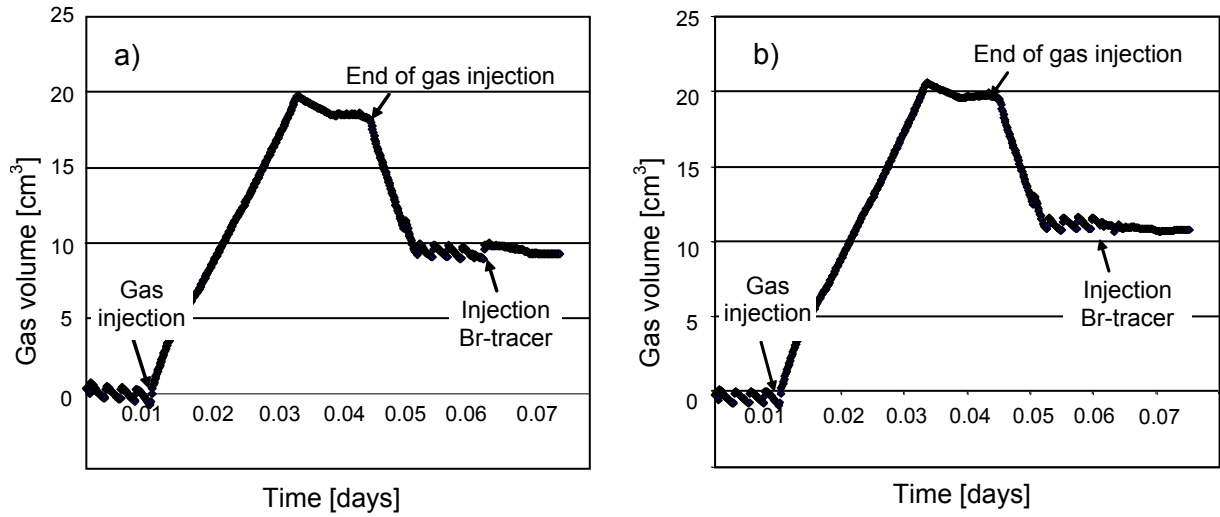


FIGURE 15: Gas volume in the column calculated from gravimetric measurements versus time shown for experiment 5 a) before corrections b) after corrections of the linear drift between the balances.

After accomplishing both corrections, the gravimetric measurements of the gas volume were used to determine the maximum residual gas saturation S_g^{\max} in the column at the end of the gas injection for each experiment (Appendix 4):

$$S_g^{\max} = \frac{V_g^{\max}}{V_{p,\text{tot}}}, \quad (48)$$

where V_g^{\max} [cm^3] is the average maximum residual gas volume in the column and $V_{p,\text{tot}}$ [cm^3] the total pore volume (computed from the total porosity).

Moreover, a gravimetric recording of the gas flow was accomplished in the outflow of the column. Therefore, the bottle on balance 2 collecting the water flowing out of the column was coupled to another water filled glass bottle placed on balance 3. Gas flowing out of the column displaced an equivalent water volume in the second bottle. By determining the difference between the two bottles in the outflow, the gas flow out of the column can be determined by the volume of gas flowing out of the column $\Delta V_{g,\text{out}}$ for each point of time:

$$\Delta V_{g,\text{out}}(t) = \frac{(\Delta m_{w,\text{out}}^*(t) - \Delta m_{w,\text{out}}(t))}{\rho_w}, \quad (49a)$$

$$Q_{g,\text{out}}(t) = \frac{\Delta V_{g,\text{out}}}{\Delta t} \quad (49b)$$

($\Delta m_{w,\text{out}}^*(t)$ [g]: amount of water loss measured on balance 3, $\Delta m_{w,\text{out}}(t)$ [g]: amount of water gain measured on balance 2).

4.3.2 Oxygen Measurements

The dissolved oxygen concentration was measured by a conventional electrochemical Clark-type electrode (CellOx 325, WTW GmbH, Weilheim, Germany) attached in the outflow column cap. Because this kind of electrode consumes oxygen and needs a certain incident flow to measure correctly, problems can arise by reducing the flow velocity. Therefore, the dissolved oxygen concentration was additionally measured by a miniaturized fiber optic chemical sensor (FTC-PSt3, PreSens GmbH, Regensburg, Germany) (in the following referred to as optode) in a flow-through cell directly in the outflow of the column (Figure 16). The flow-through cell is connected to a corresponding oxygen meter (Fibox, PreSens GmbH, Regensburg, Germany) by a polymer optical fiber with 2 mm diameter as a light guide. The principle of the sensor operation is based on the oxygen-dependent change in luminescence intensity and lifetime of a luminescent dye. The oxygen meter internally evaluates the phase shift between the modulated blue excitation light and the red fluorescence response from a detector foil in the flow-through cell (Hecht & Kölling, 2001). The optode has the advantage over common Clark type electrodes of measuring the oxygen concentration independently of the flow velocity and without oxygen consumption (measuring range 0 – 100 % oxygen-saturation).

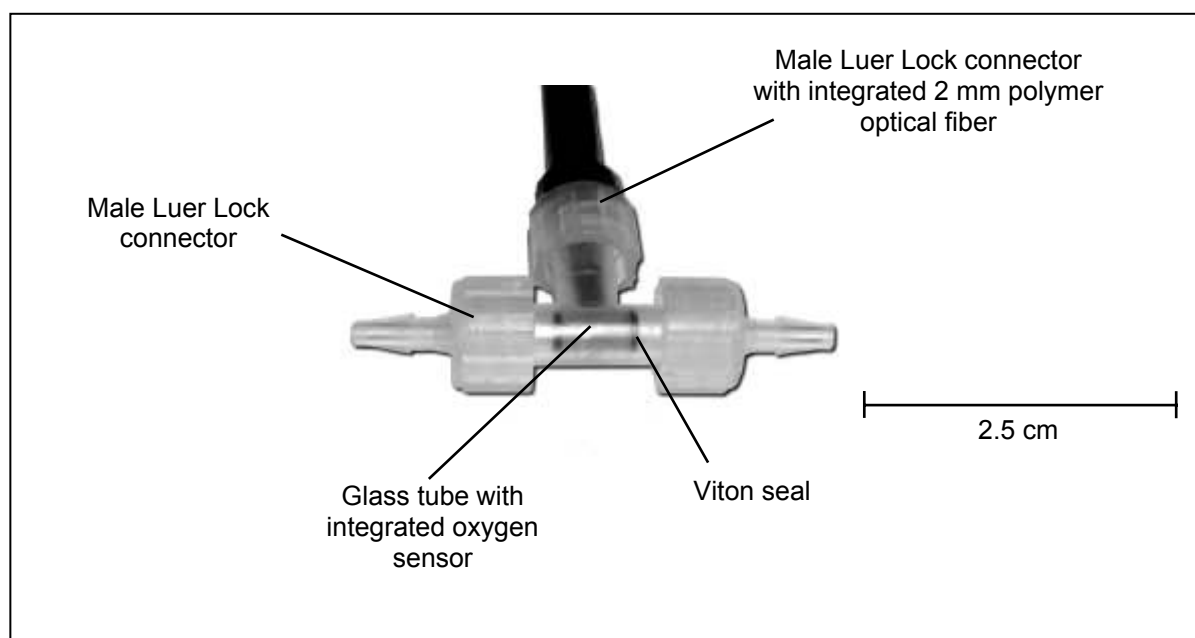


FIGURE 16: Flow-through cell with integrated oxygen sensor (optode).

The calibration of the optode was performed in the flow-through cell with the help of a calibration assistant of the Fibox software and the calibration curve calculated internally in the

Fibox oxygen meter. A conventional two-point calibration in oxygen-free water and air-saturated water had to be used. The oxygen-free water was prepared by using sodium dithionit ($\text{Na}_2\text{S}_2\text{O}_4$). The oxygen meter relates the measured phase angles to the oxygen content. Thereby, the optode shows a distinct non-linearity in the calibration curve, which can be described by a modified Stern-Volmer equation (Holst et al., 1997) (Appendix 5.1). The manufacturer gives an accuracy of the optode of 1 % air-saturation at 100 % air-saturation (i.e. 20 % oxygen-saturation) at 20 °C. Unfortunately, with the Stern-Volmer equation used by the Fibox oxygen meter and the two-point calibration using air-saturated water as maximum value, the uncertainty increases with increasing oxygen-saturation (deviation up to 15 % at 100 % oxygen-saturation). Since concentrations at those high levels were the sensitive area for the experiments, the optode was carefully re-calibrated for high concentrations. Therefore, a three-point calibration in oxygen-free, air-saturated and oxygen saturated water was performed with the sensor and repeated three times. A new modified Stern-Volmer equation was determined with this three-point calibration and the phase angles measured during the experiments were correlated to the oxygen concentrations, resulting in a medium deviation of 1.7 % at 100 % oxygen saturation (Appendix 5.2).

As expected, differences between the two oxygen measurement methods arose, mainly for small velocities due to oxygen consumption of the Clark-type electrode. The optode delivered more stable results for all velocities under investigation. Consequently, the data shown in the following are obtained from that sensor. The oxygen concentration curves reflecting the temporal change of the oxygen concentration in the water phase at the column outlet are presented as concentration versus eluted saturated pore volumes (calculated for the total porosity $\phi_{\text{tot}} = 0.376$). The time t_{PV} needed for one pore volume to pass through a control volume (here the column) is:

$$t_{\text{PV}} = \frac{L}{u_w}. \quad (50)$$

However, the water filled pore volume changes during the dissolution of the trapped gas phase. Applying the saturated pore volume instead of the effective pore volume leads to a maximum deviation of 10 % at maximum gas saturation, at which the deviation decreases with continuous dissolution. Nevertheless, this presentation allows an approximation of how much water is flowing through the pores until the gas bubbles do not release oxygen anymore. Therefore it allows a better comparability to experiments from the literature.

4.3.3 Hydraulic Conductivity Measurements

The change in hydraulic head difference over the column during the dissolution of the oxygen gas phase was measured directly through pressure transducers (HCXM100D6H, Sensortech, Puchheim, Germany) installed in the column caps at the column in- and outlet (Figure 17). As reference pressure the air pressure in the constant temperature room was measured. The key advantage of using pressure transducers instead of the more traditional piezometers is that they permit the measurement of the pressure potential to be fully automated. They also tend to be more sensitive than piezometers to small changes in hydraulic head (Baveye et al., 1998). The pressure transducers were calibrated before each experiment with the help of a water filled glass tube for four and five different pressures, respectively (Appendix 6).

The averaged hydraulic conductivity K_f was calculated as an additional process indicator via the water pressure measurements before gas injection and during the dissolution of the gas phase using the following form of Darcy's law:

$$K_f = q_w \cdot \frac{L}{\Delta h}, \quad (51a)$$

$$\Delta h = (h_{w,in} - h_{w,out}) - L, \quad h_w = \frac{p_w}{\rho_w \cdot g} \quad (51b)$$

(L [m]: distance between the two points where h is measured (in our experiments the column length), Δh [m]: difference in hydraulic head, $h_{w,in}$ [m]: hydraulic head at the column inlet, $h_{w,out}$ [m]: hydraulic head at the column outlet). In the results section the hydraulic conductivity is displayed as values normalized to the maximum hydraulic conductivity at complete water saturation of the column ($K_f^{Sg}/K_f^{Sg=0}$) versus saturated pore volumes for a better comparability of the single experiments. Oscillations can be seen in the hydraulic conductivity measurements caused by the automatic temperature regulation of the constant temperature room, which resulted in a periodic pressure variation and consequently in a gas volume change. At low flow velocities the error noise became too strong and the pressure measurements in the column cap were not stable enough. Therefore, the hydraulic conductivity measurements could not be displayed for the experiments conducted at a flow velocity of 4 m/d.

The residual gas saturation in the column influences the hydraulic conductivity. Consequently, the measured changes in hydraulic conductivity can be used as an indirect indicator of the saturation state in the column. After the gas injection is stopped and the maximum gas saturation is reached, the minimum hydraulic conductivity is measured. During

the dissolution of the gas phase, the hydraulic conductivity increases again until the column is completely water saturated and the hydraulic conductivity reaches its initial value.

4.3.4 Bromide Measurements and Bromide Tracer Tests

Tracer tests are aimed at determining the physical parameters of the investigated system. In this work bromide tracer tests were conducted to determine the effective porosity ϕ_{eff} [-] and the longitudinal dispersivity α_1 [m]. Each bromide tracer test was performed by injecting 1 ml of a bromide solution with a syringe at the column inflow end (Figure 13). At an average, three bromide tracer tests were conducted before the oxygen injection in order to determine the initial parameters. One bromide tracer test was conducted after the gas injection was stopped to determine the parameters for the state with the maximum gas saturation (except for experiments 1, 2 and 4 due to experimental problems). Furthermore, consecutive bromide tracer tests were performed for each experiment during the dissolution of the oxygen gas phase. Altogether, a total of 147 bromide tracer tests were performed over all ten experiments.

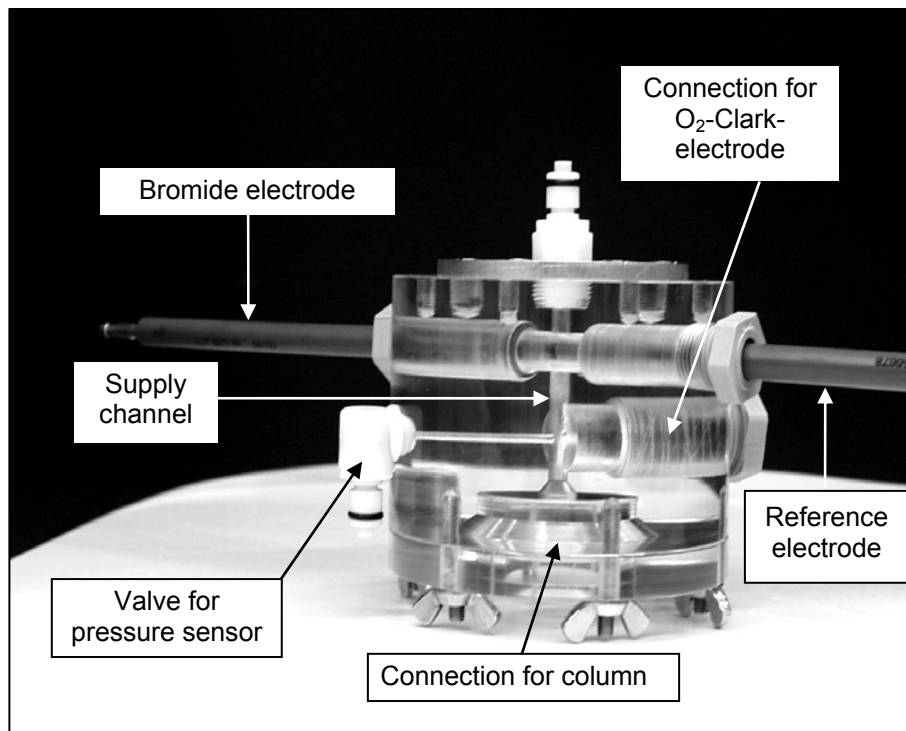


FIGURE 17: Installation of the bromide electrodes in the column cap.

Solid state bromide ion-selective electrodes (ELIT 8271, Nico200 Ltd., London, UK) were attached in the column caps together with a double junction potassium nitrate reference electrode (ELIT 002, Nico200 Ltd., London, UK) (Figure 17), which allowed a measurement

of the bromide concentration directly in the in- and outflow of the column. To maximize the incident flow along the electrodes, the supply channels in the column cap were made as small as possible. The electrodes were pre-conditioned by immersing both the bromide ion-selective electrodes and the reference electrode in 1000 ppm standard solution for approximately one day. Before each experiment a four-point calibration was conducted in the column caps under flow conditions similar to that of the experiment (Appendix 7). The manufacturer states a potential drift of the electrodes of < 3 mV/d (in 1000 ppm).

Since the column has a high ratio of length to diameter of about 44, the tracer transport through the column can be considered as one-dimensional and is well described by a 1D-transport equation (Bear, 1972). Figure 18 illustrates that the almost symmetrical curves of the conservative tracer (black line) were described well by an analytical Dirac solution (red line). Based on a Marquard-Levenberg algorithm, which is part of the software Origin 6.1, the two variable parameters ϕ_{eff} and α_1 were determined. The mass of the injected bromide, the cross sectional area of the column, the column length, and the Darcy velocity were used as fixed input parameters.

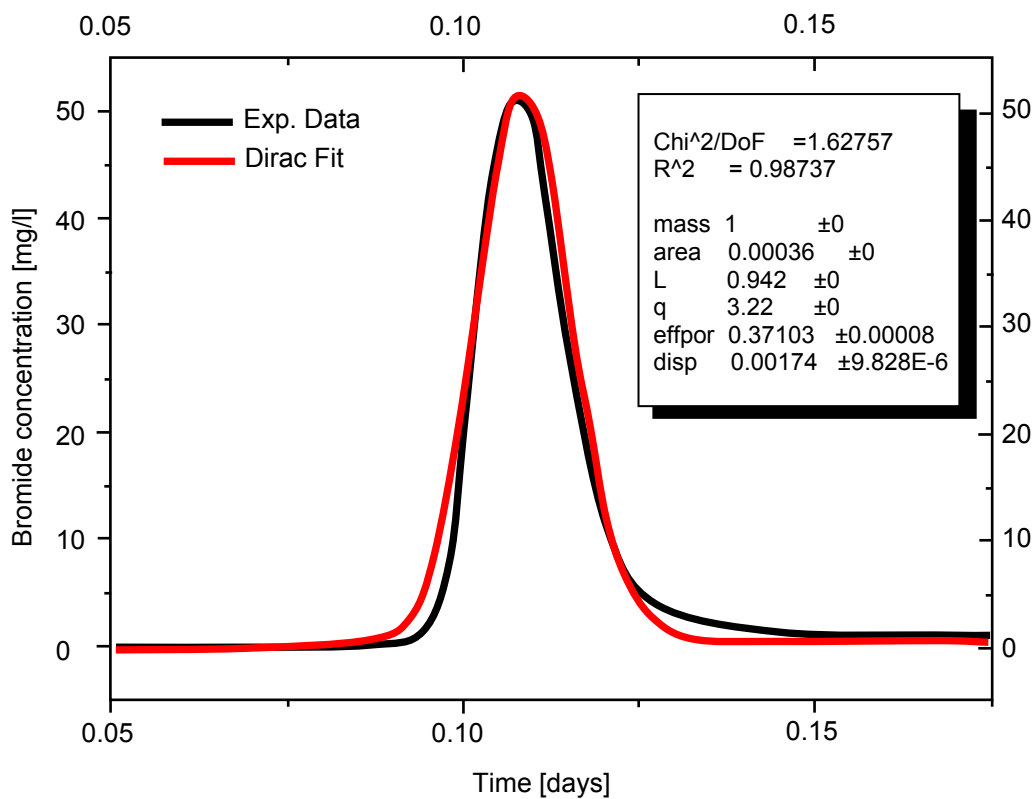


FIGURE 18: Automated parameter estimation: Exemplary bromide breakthrough curve. Black line: Experimental bromide tracer curve; red line: Analytical Dirac solution.

Because the bromide concentration was measured in the inflow as well as in the outflow of the column, the validity of the Dirac solution applied could be tested by a numerical solution using the actual time-dependent inflow bromide concentration (central spatial weighting, Cranc-Nicolson time weighting, Courant numbers of 0.5 and 1.0, discretizations of 500 and 1000). The correlation coefficient between the Dirac- and the numerical solution was higher than 0.997.

Because the flow field of the column can be considered to be very homogeneous, immobile water phases can be neglected. Consequently, the effective porosity determines the fractional volume of water filled pore space and gives information about the gas phase content ($= \phi_{\text{eff}}^{\text{max}} - \phi_{\text{eff}}$). Since the total volume of the column was determined after the experiments via weighting, the effective volume of the water and gas phase can be calculated with the help of the bromide tracer tests. Then the gas saturation S_g could be calculated using Equation 48 (Appendix 4). Thereby, the total pore volume $V_{p,\text{tot}}$ was calculated for each experiment using the maximum effective porosity determined by the bromide tracer tests for complete water saturation.

4.3.5 Peristaltic Pump

For the control of the flow rate and variation of the flow velocities applied in the single experiments, two four-channel peristaltic pumps (IP 4, Ismatec, Glattbrugg, Switzerland) were used. An advantage is the low dependency of the flow rate on the pressure in the column. The flow rate can be adjusted via the rotational frequency of the pump. Additionally, the flow rate can be varied by changing the inner diameter of the pumping tubes. Consequently, the adjustment to different flow rates for gas and water was achieved with the help of the peristaltic pumps. Gastight Viton tubes with an inner diameter of 1.65 mm were used to reduce gas losses when pumping gas or gas saturated water. In addition, the pumps were placed in boxes with a permanent gas supply (either oxygen or flushing gas). In the forefront of the experiments a calibration curve was plotted to test the linearity of the flow rate relating to the rotational frequency of the pumps (Appendix 8).

4.3.6 Data Acquisition

For a steady acquisition of the measured data at regular intervals over the complete period of a single experiment, which runs over a period of several days, it was necessary to record the data online. Therefore, the bromide electrodes, the oxygen electrode as well as the pressure

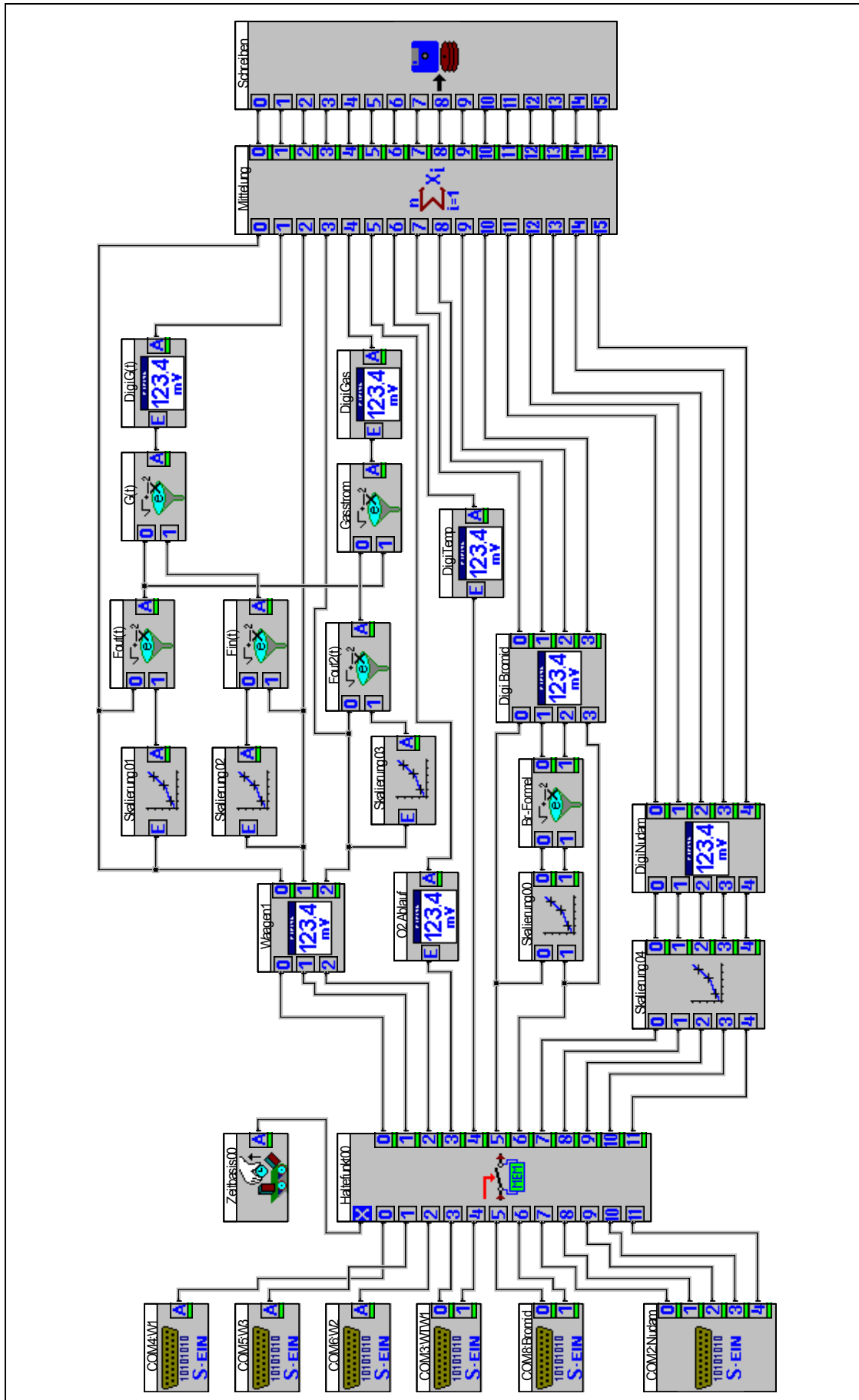


FIGURE 19: Graphical user interface with digital readouts (DasyLab 6.0).

sensors were attached to a data logger, at which an analog signal was measured and passed on as a digital signal via a RS232-interface to a computer. Similarly, a computer based data recording of the water and gas flow occurred via the balances. With the aid of software for data acquisition (DASYLab 6.0), the measured values were recorded and saved online during the experiment. A clearly arranged graphical user interface with digital readouts was created (Figure 19). Measurements were collected at 10 second intervals so that several hundred measured concentrations for oxygen and bromide were obtained in each experiment. The data of the optode was recorded separately via software delivered with the sensor.

4.4 Experimental Procedure

The same experimental procedure was applied before each dissolution experiment. Test solutions were prepared in two 5 l glass bottles. One bottle contained oxygen-saturated water, prepared by flushing pure oxygen gas through distilled water; the other contained distilled water with an oxygen content as low as possible. This was achieved by flushing helium, nitrogen or argon through the water. The headspace in the glass bottles was flushed with oxygen or flushing gas, respectively, to sustain the saturation state of the solutions.

Regarding the flushing gas, nitrogen was chosen as the main constituent of atmospheric air, argon and helium as examples for atmospheric trace gases that are not affected by chemical or biological processes. Moreover, the three gases show a variation in their diffusion and dimensionless Henry's law constant, consequently a different influence on the dissolution process of oxygen bubbles could be expected. In the solutions with the high oxygen content an average saturation with oxygen of approximately 94.1 % was achieved resulting in a dissolved oxygen concentration of about $50.2 \text{ mg/l} \pm 2.3 \text{ mg/l}$, while the dissolved oxygen concentration in the low oxygen solution ranged between 0.2 and 2.9 mg/l (at atmospheric pressure).

Prior to each experiment carbon dioxide gas was injected at the bottom of the column for approximately 30 min to displace any residual air from the pore space. Then oxygen-saturated water was pumped through the column for a certain time (approximately 1-2 days), dissolving the highly soluble carbon dioxide until stable flow conditions were established and the column was completely water-saturated.

The procedure of the gas injection is illustrated in Figure 20 in principle. Each experiment started by the injection of oxygen gas at the bottom of the column. Concurrent to the gas injection, oxygen-saturated water was pumped into the column. The gas injection was stopped when a first steady-state flow condition was reached (volumetric flow rate of water $Q_w [\text{m}^3/\text{d}]$

into the column is equal to the volumetric flow rate out of the column $Q_{w,in} = Q_{w,out}$; dynamical gas saturation of the column). Figure 20 shows the typical decrease of the gas volume in the column, which signifies that not the complete dynamical gas saturation can be bound as trapped gas phase in the sediment.

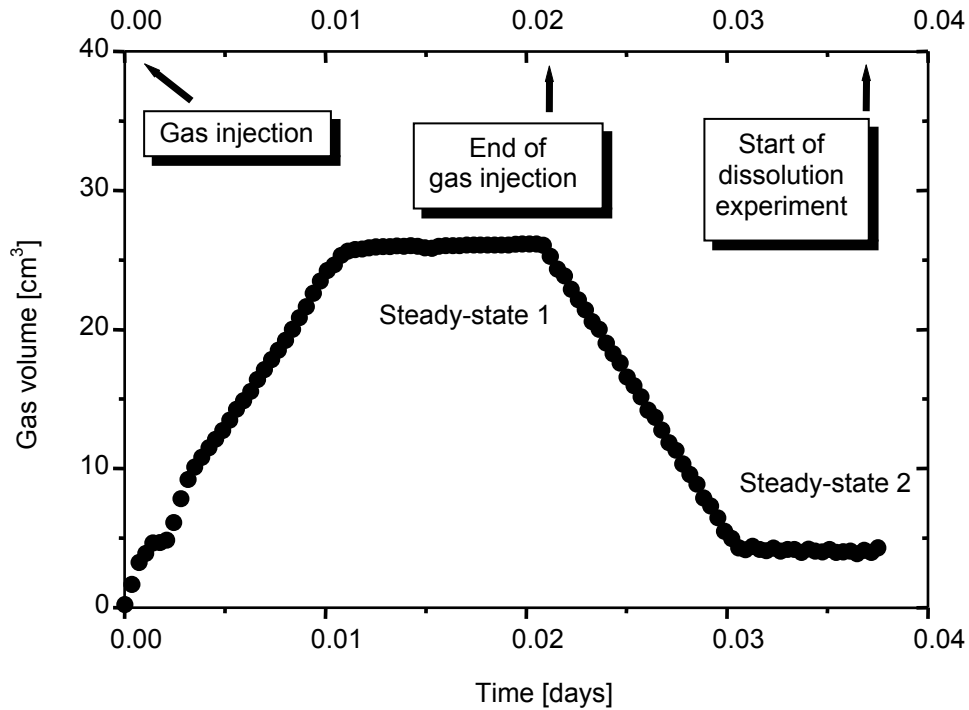


FIGURE 20: Procedure of the gas injection. The experiment started by the injection of oxygen gas at the bottom of the column. The gas injection was stopped when a first steady-state flow condition was reached. The gas volume in the column decreased until a second steady-state flow condition was established and the column feed was switched to the low oxygen solution (start of the dissolution of the trapped oxygen gas phase).

After a second steady-state flow condition was established (residual stationary gas saturation of the column), the column feed was switched to the low oxygen solution and the dissolution of the trapped oxygen gas phase began (time $t = 0$ of the actual dissolution experiment).

5. Experimental Results

Dissolution experiments were performed using the sand-filled, dynamically compressed column to gain insight into the processes that occur during the direct injection of pure oxygen gas into a porous medium. The column was fixed in a vertical position and the direction of flow during the experiments was from bottom to top. The data gained from the gravimetric measurements, the oxygen measurements, the hydraulic conductivity measurements and the bromide measurements were collected and evaluated. As mentioned before, all experiments were replicated. In the following, the results are displayed for both experiments conducted at the same initial conditions, respectively, for comparison.

5.1 Test Series 1: Influence of Different Dissolved Gases on the Dissolution of a Trapped Oxygen Gas Phase

To dissolve the injected oxygen gas phase the column was flushed with an almost oxygen free flushing solution produced by fully saturating water with a flushing gas. In the first test series the gases helium, nitrogen and argon were used as flushing gas preparing the low oxygen solution, to determine the influence of already dissolved gases on the dissolution of a trapped oxygen gas phase. The water flow velocity for each experiment was approximately 17 m/d (volumetric flow rates ranged between 1.54 and 1.64 cm³/min with an averaged standard deviation of 0.01 cm³/min). Altogether, six experiments were conducted in this series:

- experiments 1 and 2 with helium as flushing gas,
- experiments 3 and 4 with nitrogen as flushing gas,
- experiments 5 and 6 with argon as flushing gas.

5.1.1 Helium as Flushing Gas

In Table 5 the most important experimental results for experiments 1 and 2 are listed. The changes in gas volume in the column before the start of the dissolution experiment calculated from gravimetric measurements are displayed for experiments 1 and 2 in Figure 21. The data set was corrected for the balance drift (see Chapter 4.3.1). In both experiments the gas injection was started after approximately 0.01 days. Immediately with the gas entry into the column, the gas volume in the column increased until the first steady-state flow condition with dynamical gas saturation of the column established after 0.038 d for experiment 1 and

0.035 d for experiment 2. The gas volume injected into the column amounted to approximately 19 cm³ for both experiments at that time.

TABLE 5: Parameters and results of experiments 1 and 2 (helium as flushing gas).

Parameter	Experiment 1	Experiment 2
Q_w [cm ³ /min]	1.57 ± 0.02	1.59 ± 0.002
Q_g [cm ³ /min] ¹	0.64	0.92
q_w [m/d]	6.29 ± 0.13	6.37 ± 0.07
u_w^{\max} [m/d] ²	16.7 ± 0.5	16.9 ± 0.3
$p_{\text{hyd,out}}$ [kPa] ³	7.3 ± 0.07	6.7 ± 0.07
p_{atm} [kPa] ⁴	101.5 ± 0.2	101.6 ± 0.1
T [°C] ⁵	11.5 ± 1	11.5 ± 1
Min. hydraulic conductivity [m/s] ⁶	$1.15 \cdot 10^{-4}$	$1.14 \cdot 10^{-4}$
Max. hydraulic conductivity [m/s] ⁷	$2.12 \cdot 10^{-4}$ ± $0.03 \cdot 10^{-4}$	$2.18 \cdot 10^{-4}$ ± $0.03 \cdot 10^{-4}$
Min. effective porosity [%] ⁸	-	-
Max. effective porosity [%] ⁹	37.8 ± 0.3	37.1 ± 0.2
Max. longitudinal dispersivity [mm] ⁹	2.7 ± 0.1	2.7 ± 0.1
Max. $S_{g,\text{grav}}$ [%] ¹⁰	8.2 ± 0.3	7.5 ± 0.3
Max. $S_{g,\text{tracer}}$ [%] ¹¹	-	-
$C_{\text{O}_2,w}$ [mg/l] ¹²	57.5 ± 0.75	56.9 ± 0.62
$C_{\text{O}_2,w}^{\text{ini}}$ [mg/l] ¹³	2.2	2.9

¹ gas flow rate during gas injection determined gravimetrically at the column outlet

² water flow velocity at complete water saturation calculated with the tot. porosity ($\phi_{\text{tot}} = 0.376$)

³ artificially applied hydrostatic pressure at column outflow

⁴ average atmospheric pressure during dissolution experiment

⁵ average temperature during dissolution experiment

⁶ determined by pressure measurements at maximum residual gas saturation

⁷ determined by pressure measurements at complete water saturation

⁸ determined by bromide tracer tests at maximum residual gas saturation

⁹ determined by bromide tracer tests at complete water saturation

¹⁰ maximum residual gas saturation determined by gravimetric measurements

¹¹ maximum residual gas saturation determined by bromide tracer tests

¹² oxygen concentration in the water phase at the begin of the dissolution experiment

¹³ oxygen concentration in flushing solution

The gas flow out of the column was measured gravimetrically after the gas breakthrough. For experiments 1 and 2 a gas flow rate of 0.64 cm³/min and 0.92 cm³/min was determined, respectively (Table 5). The first steady-state flow condition was maintained for 20 minutes before the gas injection was stopped. Instantly with the end of the gas flow into the column, the gas volume decreased. The second steady-state flow condition with the residual gas saturation was reached after 0.061 d for experiment 1 and 0.056 d for experiment 2. As mentioned before, for both experiments no bromide tracer test was conducted at the period

when the maximum residual gas saturation was attained. Therefore the residual gas saturation of the column was detected by gravimetric measurements only. For experiment 1 a residual gas volume of $10.5 \text{ cm}^3 \pm 0.34 \text{ cm}^3$ was determined from the gravimetric measurements, which corresponds to a maximum residual gas saturation of 0.082 ± 0.003 . For experiment 2 the residual gas volume was $9.5 \text{ cm}^3 \pm 0.26 \text{ cm}^3$, resulting in a gas saturation of 0.075 ± 0.003 (Table 5).

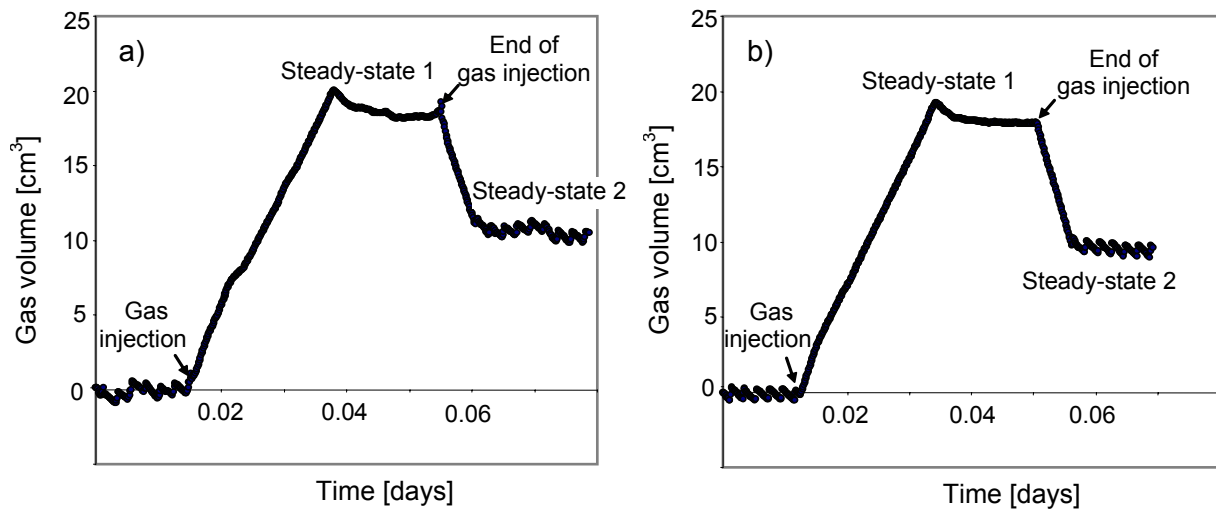


FIGURE 21: Gas volume in the column determined by gravimetric measurements before the start of the dissolution experiment for a) experiment 1 and b) experiment 2. The water flow rate for experiment 1 was $1.58 \text{ cm}^3/\text{min}$ and the gas flow rate was $0.64 \text{ cm}^3/\text{min}$. For experiment 2 a water flow rate of $1.59 \text{ cm}^3/\text{min}$ was applied and a gas flow rate of $0.92 \text{ cm}^3/\text{min}$. In both experiments helium was used as flushing gas. For both experiments no bromide tracer test was conducted during the second steady-state flow condition.

The dissolved oxygen concentration curves recorded at the column outlet during the dissolution of the injected oxygen gas phase (the actual dissolution experiment) are displayed in Figure 22 for experiments 1 and 2. The water flow velocity determined from the gravimetric measurements was $16.7 \text{ m/d} \pm 0.5 \text{ m/d}$ for experiment 1 and $16.9 \text{ m/d} \pm 0.3 \text{ m/d}$ for experiment 2 (Table 5). Both curves show a plateau-like phase with a nearly constant concentration pattern at the beginning, resembling a quasi-steady-state condition, although the dissolution progress is still continuing. The average oxygen concentration at this plateau-like phase was $57.5 \text{ mg/l} \pm 0.75 \text{ mg/l}$ for experiment 1 and $56.9 \text{ mg/l} \pm 0.62 \text{ mg/l}$ for experiment 2 (Table 5). These values are higher than the oxygen concentrations achievable at atmospheric pressure (approximately 53 mg/l) due to the higher hydrostatic pressure in the column. After approximately 3 saturated pore volumes were exchanged, the effluent dissolved oxygen

concentration shows a steep decline and reaches concentrations identical to that in the flushing solution (feed concentration; about 2.5 mg/l) after the exchange of 3.5 pore volumes. That means that after this time the residual oxygen gas phase was completely dissolved.

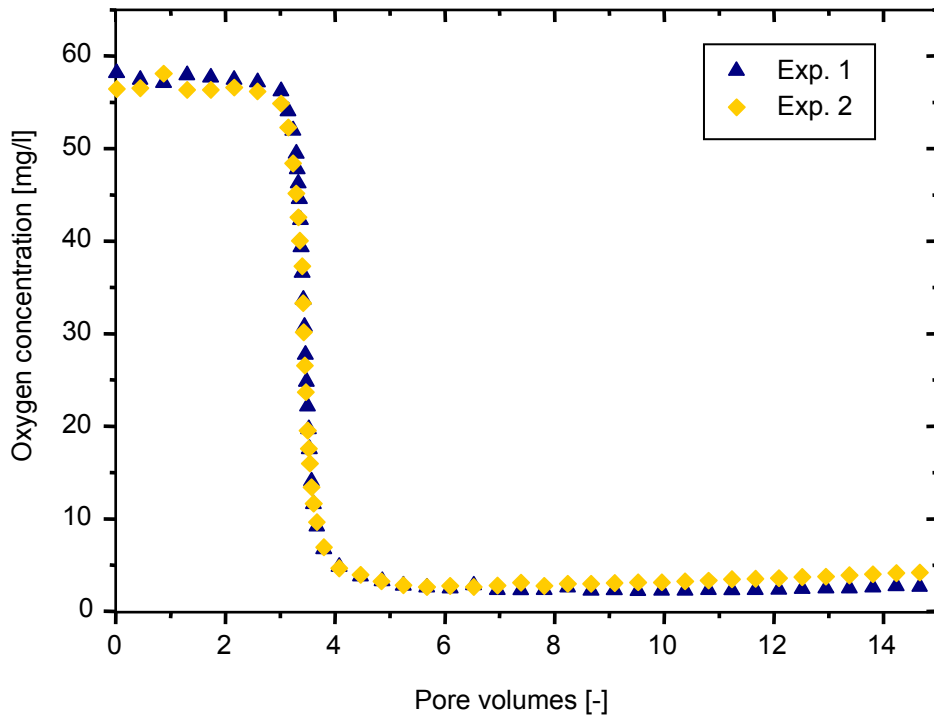


FIGURE 22: Dissolved oxygen concentration versus saturated pore volumes recorded at the column outlet during the dissolution of the injected oxygen gas phase for experiment 1 (dark blue triangles) and 2 (yellow squares). The water flow velocity determined from the gravimetric measurements was 16.7 m/d for experiment 1 and 16.9 m/d for experiment 2. In both experiments helium was used as flushing gas.

Figure 23 shows the normalized hydraulic conductivity versus saturated pore volumes for experiments 1 and 2. Both curves exhibit a steep increase at the beginning and reach the maximum value after approximately 3.5 pore volumes were exchanged. The progression of the hydraulic conductivity curves corresponds to the oxygen curves. Both measurements imply that in the experiments where helium was used as flushing gas, the oxygen gas phase was completely dissolved after the exchange of 3.5 pore volumes and complete water saturation was attained again. The maximum hydraulic conductivity at complete water saturation was $2.12 \cdot 10^{-4} \text{ m/s} \pm 0.03 \cdot 10^{-4} \text{ m/s}$ for experiment 1 and $2.18 \cdot 10^{-4} \text{ m/s} \pm 0.03 \cdot 10^{-4} \text{ m/s}$ for experiment 2. The maximum K_F -values correspond to the values that were achieved before the gas injection at complete water saturation of the column (data not shown).

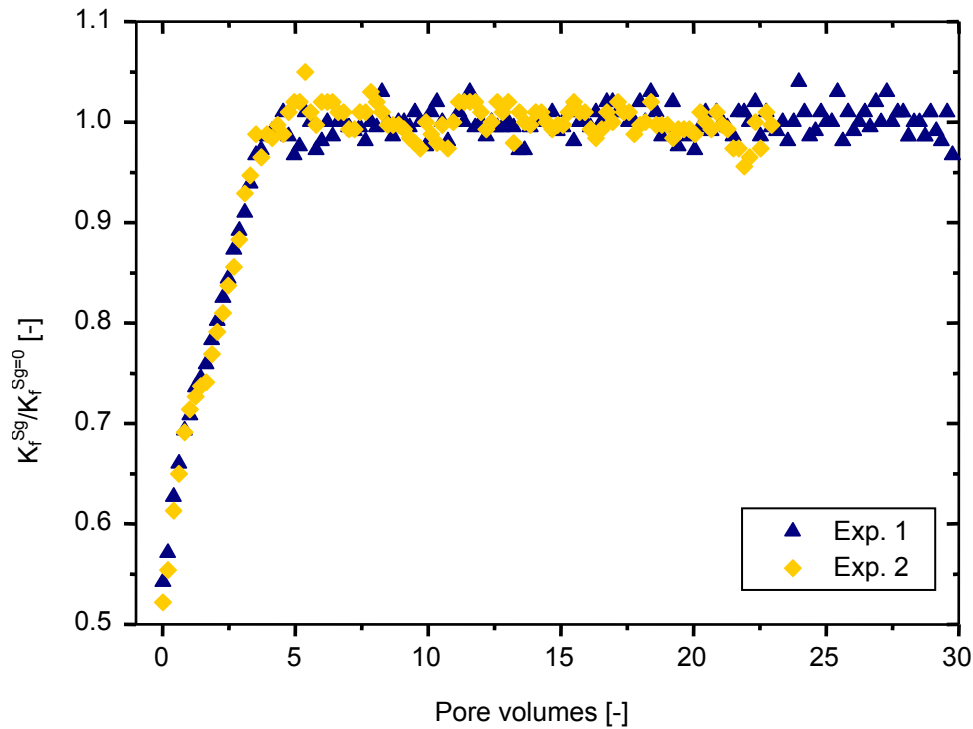


FIGURE 23: Normalized hydraulic conductivity plotted versus the saturated pore volumes for experiment 1 (dark blue triangles) and 2 (yellow squares) (helium used as flushing gas).

The results of the bromide tracer tests conducted during the dissolution experiments 1 and 2 are presented in Figure 24. The two physical parameters, the longitudinal dispersivity and the effective porosity, determined directly by the tracer tests are presented versus the pore volumes. Furthermore, the gas saturations calculated from the effective porosity determined in the tracer tests are displayed.

The effective porosity as well as the corresponding gas saturations reflects the results of the dissolved oxygen curves and the hydraulic conductivity curves, whereas the longitudinal dispersivity shows no distinct trend. The progression of the effective porosity shows a steep increase after exchanging 3.5 pore volumes. Then a plateau is reached, at which the values scatter around a maximum value similar to those values measured before the gas injection at complete water saturation of the column (data not shown). The maximum effective porosity for experiment 1 was 0.378 ± 0.003 . For experiment 2 a value of 0.371 ± 0.002 was determined. The gas saturations computed from the effective porosity show a reverse progression, since at maximum effective porosity the minimum gas saturation is reached. For the maximum longitudinal dispersivity (determined at complete water saturation) an averaged value of $2.7 \text{ mm} \pm 0.1 \text{ mm}$ was determined for both experiments.

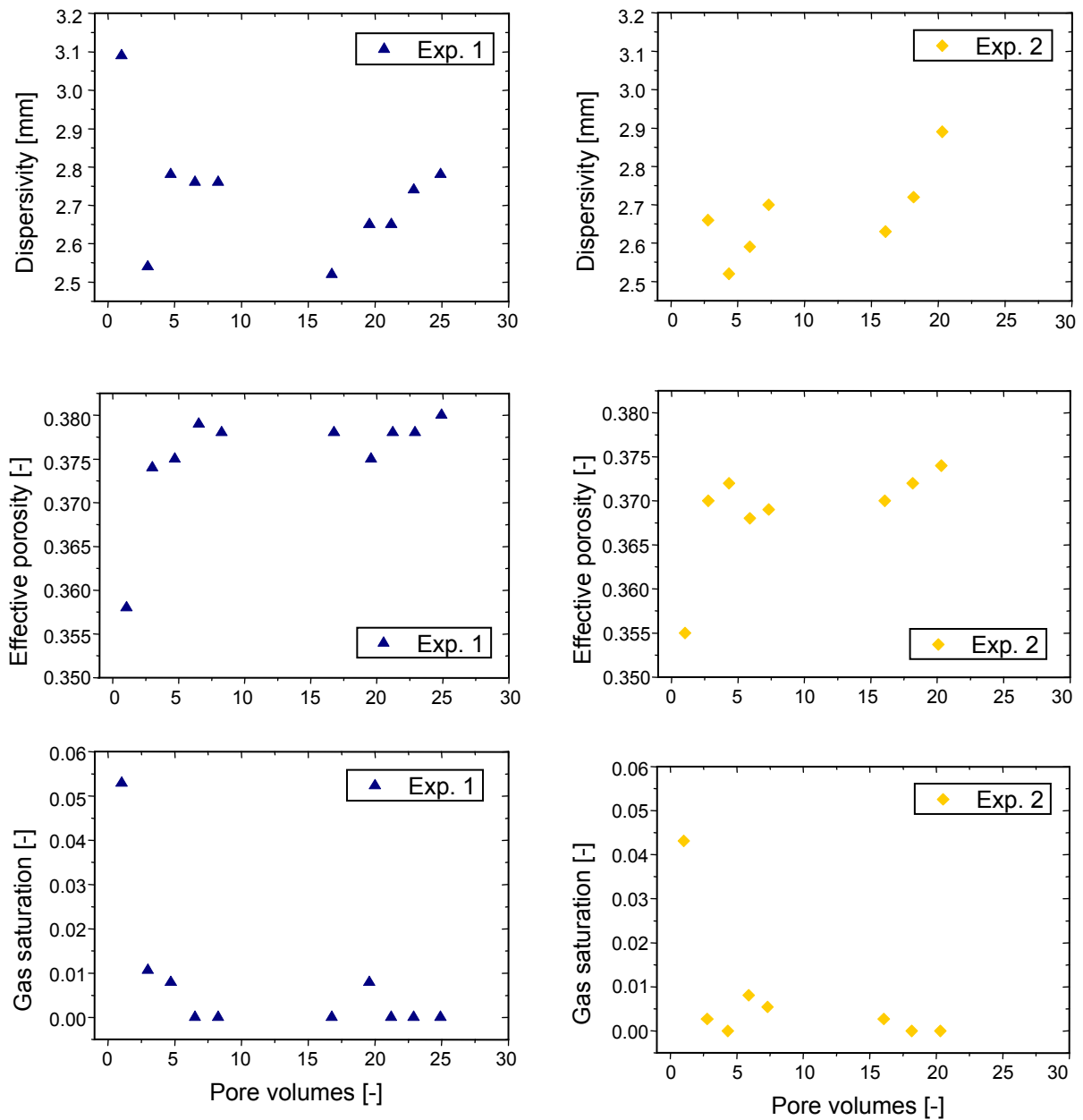


FIGURE 24: Longitudinal dispersivity, effective porosity and corresponding gas saturation determined by bromide tracer test during dissolution experiment 1 (dark blue triangles) and 2 (yellow squares). Helium was used as flushing gas.

5.1.2 Nitrogen as Flushing Gas

For the experiments where nitrogen was used to prepare the low oxygen solution (experiments 3 and 4), the most important experimental results are listed in Table 6.

TABLE 6: Parameters and results of experiments 3 and 4 (nitrogen as flushing gas).

Parameter	Experiment 3	Experiment 4
Q_w [cm ³ /min]	1.56 ± 0.01	1.64 ± 0.01
Q_g [cm ³ /min] ¹	0.80	0.53
q_w [m/d]	6.25 ± 0.08	6.56 ± 0.09
u_w^{\max} [m/d] ²	16.6 ± 0.4	17.4 ± 0.4
$p_{\text{hyd,out}}$ [kPa] ³	7.3 ± 0.06	6.6 ± 0.04
p_{atm} [kPa] ⁴	101.4 ± 0.06	101.9 ± 0.3
T [°C] ⁵	11.2 ± 1	11.5 ± 1
Min. hydraulic conductivity [m/s] ⁶	$1.21 \cdot 10^{-4}$	$1.11 \cdot 10^{-4}$
Max. hydraulic conductivity [m/s] ⁷	$1.84 \cdot 10^{-4}$ ± $0.03 \cdot 10^{-4}$	$1.88 \cdot 10^{-4}$ ± $0.02 \cdot 10^{-4}$
Min. effective porosity [%] ⁸	33.7 ± 0.2	-
Max. effective porosity [%] ⁹	37.2 ± 0.3	37.6 ± 0.3
Max. longitudinal dispersivity [mm] ⁹	2.7 ± 0.2	2.8 ± 0.4
Max. $S_{g,\text{grav}}$ [%] ¹⁰	7.7 ± 0.3	8.3 ± 0.4
Max. $S_{g,\text{tracer}}$ [%] ¹¹	9.4 ± 1.4	-
$C_{\text{O}_2,w}$ [mg/l] ¹²	58.1 ± 0.44	58.3 ± 1.10
$C_{\text{O}_2,w}^{\text{ini}}$ [mg/l] ¹³	1.4	0.2

¹ gas flow rate during gas injection determined gravimetrically at the column outlet

² water flow velocity at complete water saturation calculated with the tot. porosity ($\phi_{\text{tot}} = 0.376$)

³ artificially applied hydrostatic pressure at column outflow

⁴ average atmospheric pressure during dissolution experiment

⁵ average temperature during dissolution experiment

⁶ determined by pressure measurements at maximum residual gas saturation

⁷ determined by pressure measurements at complete water saturation

⁸ determined by bromide tracer tests at maximum residual gas saturation

⁹ determined by bromide tracer tests at complete water saturation

¹⁰ maximum residual gas saturation determined by gravimetric measurements

¹¹ maximum residual gas saturation determined by bromide tracer tests

¹² oxygen concentration in the water phase at the begin of the dissolution experiment

¹³ oxygen concentration in flushing solution

Figure 25 shows the gravimetrically determined changes in the gas volume inside the column before the start of the dissolution experiment for experiments 3 and 4. The data set of both curves were corrected for the balance drift. For experiment 3, the gravimetrically determined gas volume had to be corrected by the injected bromide tracer mass additionally. The gas injection was started after approximately 0.01 days in both experiments. The first steady-state flow condition with dynamical gas saturation was established after 0.034 d for experiment 3 and 0.033 d for experiment 4. At the beginning of the first steady-state condition, a dynamical gas volume of about 20 cm³ prevailed in the column for both experiments. After the gas breakthrough, the gas flow out of the column could be measured gravimetrically and amounted to 0.80 cm³/min for experiment 3 and 0.53 cm³/min for experiment 4 (Table 6). The first steady-state flow condition was kept for 20 minutes before the gas injection was stopped.

Following the typical decrease of the gas volume in the column, the second steady-state flow condition with the residual gas saturation was reached after 0.057 d for experiment 3 and 0.059 d for experiment 4.

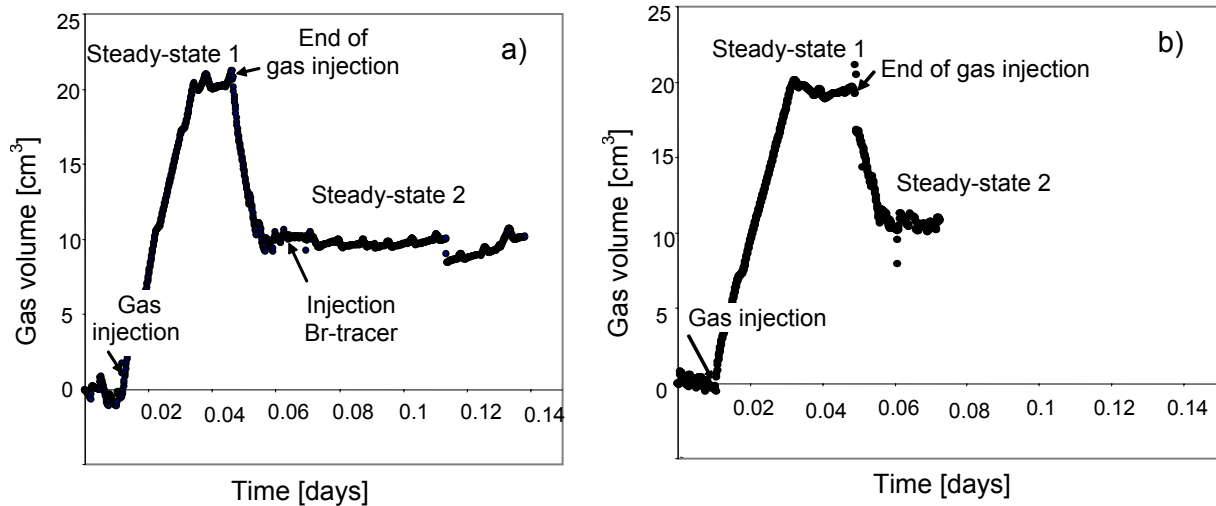


FIGURE 25: Gas volume in the column determined by gravimetric measurements before the start of the dissolution experiment for a) experiment 3 and b) experiment 4. The water flow rate for experiment 3 was $1.56 \text{ cm}^3/\text{min}$ and the gas flow rate was $0.80 \text{ cm}^3/\text{min}$. For experiment 4 a water flow rate of $1.64 \text{ cm}^3/\text{min}$ was applied and a gas flow rate of $0.54 \text{ cm}^3/\text{min}$. In both experiments nitrogen was used as flushing gas. For experiment 3 a bromide tracer test was conducted at the second steady-state flow condition.

For experiment 3, a bromide tracer test was conducted at the second steady-state flow condition (maximum residual gas saturation). Therefore, the dissolution experiment was not started until the tracer test was finished. After the bromide breakthrough curve was measured in the column outflow, the column feed was switched to the nitrogen saturated flushing solution and the dissolution experiment began. The jump in the gas volume at the end of the second steady-state condition displayed in Figure 25 a) was caused by unintentional contact with the balances. The residual gas saturation was determined by two different methods for experiment 3. From the gravimetric measurements a residual gas volume of $9.8 \text{ cm}^3 \pm 0.25 \text{ cm}^3$ was determined for the second steady-state flow condition, corresponding to a maximum residual gas saturation of 0.077 ± 0.003 . The bromide tracer test conducted at maximum residual gas saturation resulted in an effective porosity of 0.337 ± 0.003 , the gas saturation computed from the tracer test was 0.094 ± 0.014 .

For experiment 4 no bromide tracer test was performed at maximum residual gas saturation. Consequently, for this experiment the residual gas saturation of the column was detected by

the gravimetric measurements only. A residual gas volume of $10.6 \text{ cm}^3 \pm 0.43 \text{ cm}^3$ was determined from the gravimetric measurements, which corresponds to a maximum residual gas saturation of 0.083 ± 0.004 (Table 6).

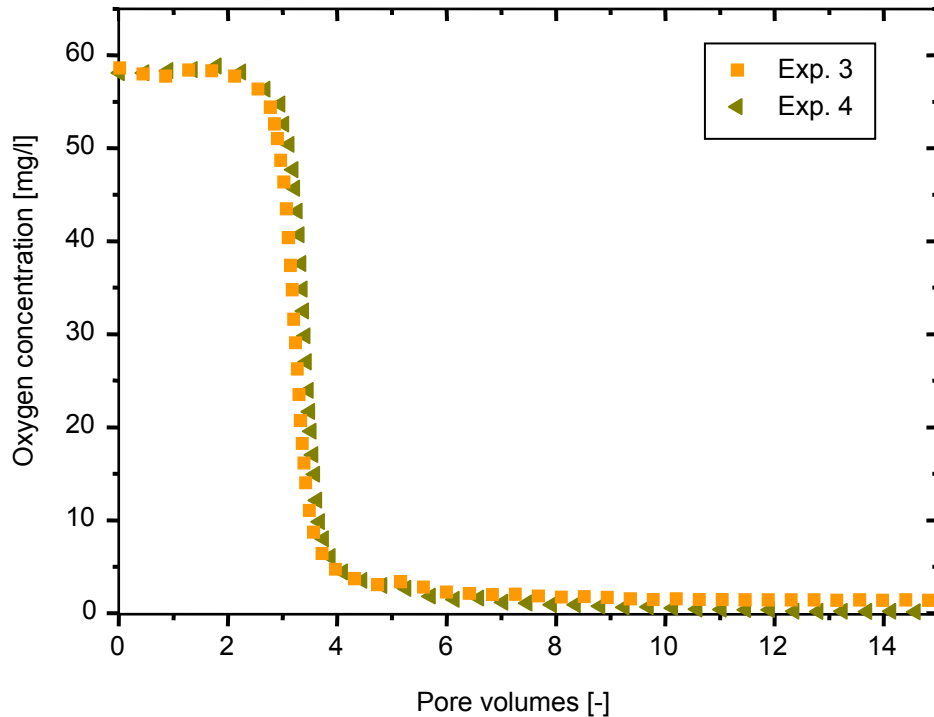


FIGURE 26: Dissolved oxygen concentration recorded at the column outlet versus saturated pore volumes for experiment 3 (orange squares) and 4 (light green triangles). The water flow velocity determined from the gravimetric measurements was 16.6 m/d for experiment 3 and 17.4 m/d for experiment 4. In both experiments nitrogen was used as flushing gas.

For experiments 3 and 4, the dissolved oxygen concentration curves recorded during the dissolution of the injected oxygen gas phase are displayed in Figure 26. The water flow velocities determined from the gravimetric measurements for experiments 3 and 4 were $16.6 \text{ m/d} \pm 0.4 \text{ m/d}$ and $17.4 \text{ m/d} \pm 0.4 \text{ m/d}$, respectively (Table 6). The progression of the dissolved oxygen concentration curves for experiments 3 and 4 (nitrogen as flushing gas) is very similar to the progression of the former two experiments 1 and 2 (helium as flushing gas). The averaged oxygen concentration obtained at the plateau-like phase at the beginning of the dissolution experiment was $58.1 \text{ mg/l} \pm 0.44 \text{ mg/l}$ for experiment 3 and $58.3 \text{ mg/l} \pm 1.1 \text{ mg/l}$ for experiment 4. Similar to experiments 1 and 2, the effluent dissolved oxygen concentration reached the feed concentration (about 1.44 mg/l for experiment 3 and 0.18 mg/l

for experiment 4) after approximately 3.5 saturated pore volumes were exchanged, indicating that the residual oxygen gas phase was completely dissolved.

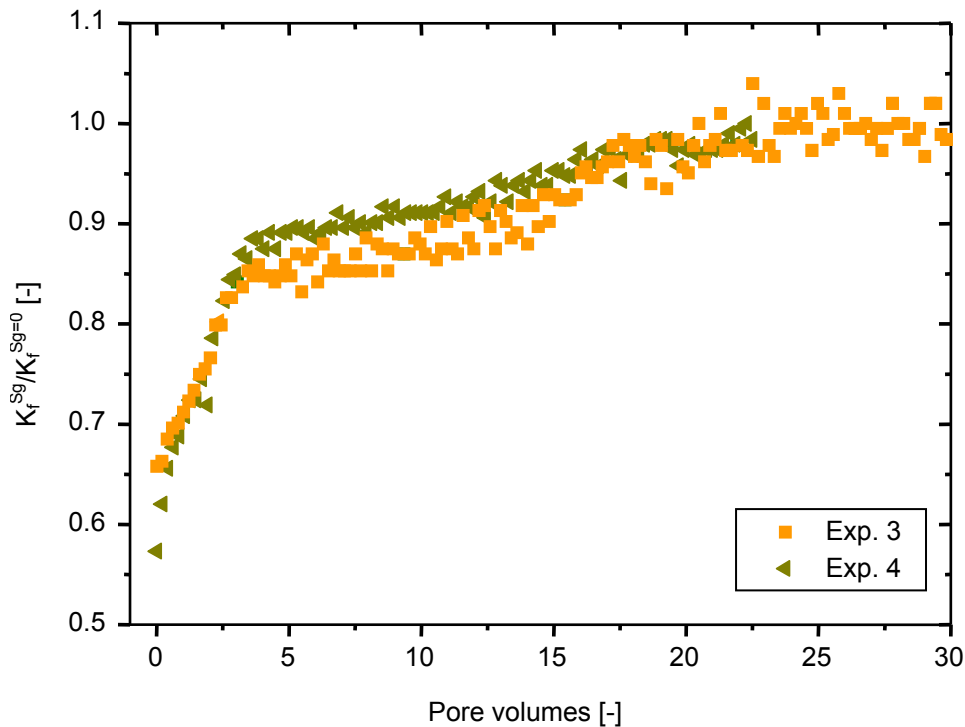


FIGURE 27: Normalized hydraulic conductivity plotted versus the saturated pore volumes for experiment 3 (orange squares) and 4 (light green triangles) (nitrogen used as flushing gas).

Figure 27 shows the normalized hydraulic conductivity versus saturated pore volumes. The hydraulic conductivity curves for experiments 3 and 4 show a different progression than the hydraulic conductivity curves from experiments 1 and 2. Both curves of the experiments conducted with nitrogen as flushing gas show a two-stage increase of the curves during the dissolution experiment. The hydraulic conductivity shows a steep increase at the beginning until the time when 3.5 pore volumes were exchanged. This first increase corresponds to the time when the trapped gas bubbles still release oxygen. When 3.5 pore volumes were exchanged, the gas bubbles do not release oxygen anymore and the curves rise slower. After approximately 22.5 pore volumes being exchanged the curves finally equal the plateau with the maximum hydraulic conductivity values, indicating that complete water saturation is reached. This means that when the trapped oxygen gas phase is completely dissolved, there is still a certain amount of gas in the column. This residual gas phase dissolves much slower in the bypassing water than the oxygen gas phase, but after the exchange of 22.5 pore volumes the entire gas phase in the column is dissolved. The maximum hydraulic conductivity at

complete water saturation was $1.84 \cdot 10^{-4} \text{ m/s} \pm 0.03 \cdot 10^{-4} \text{ m/s}$ for experiment 3 and $1.88 \cdot 10^{-4} \text{ m/s} \pm 0.02 \cdot 10^{-4} \text{ m/s}$ for experiment 4.

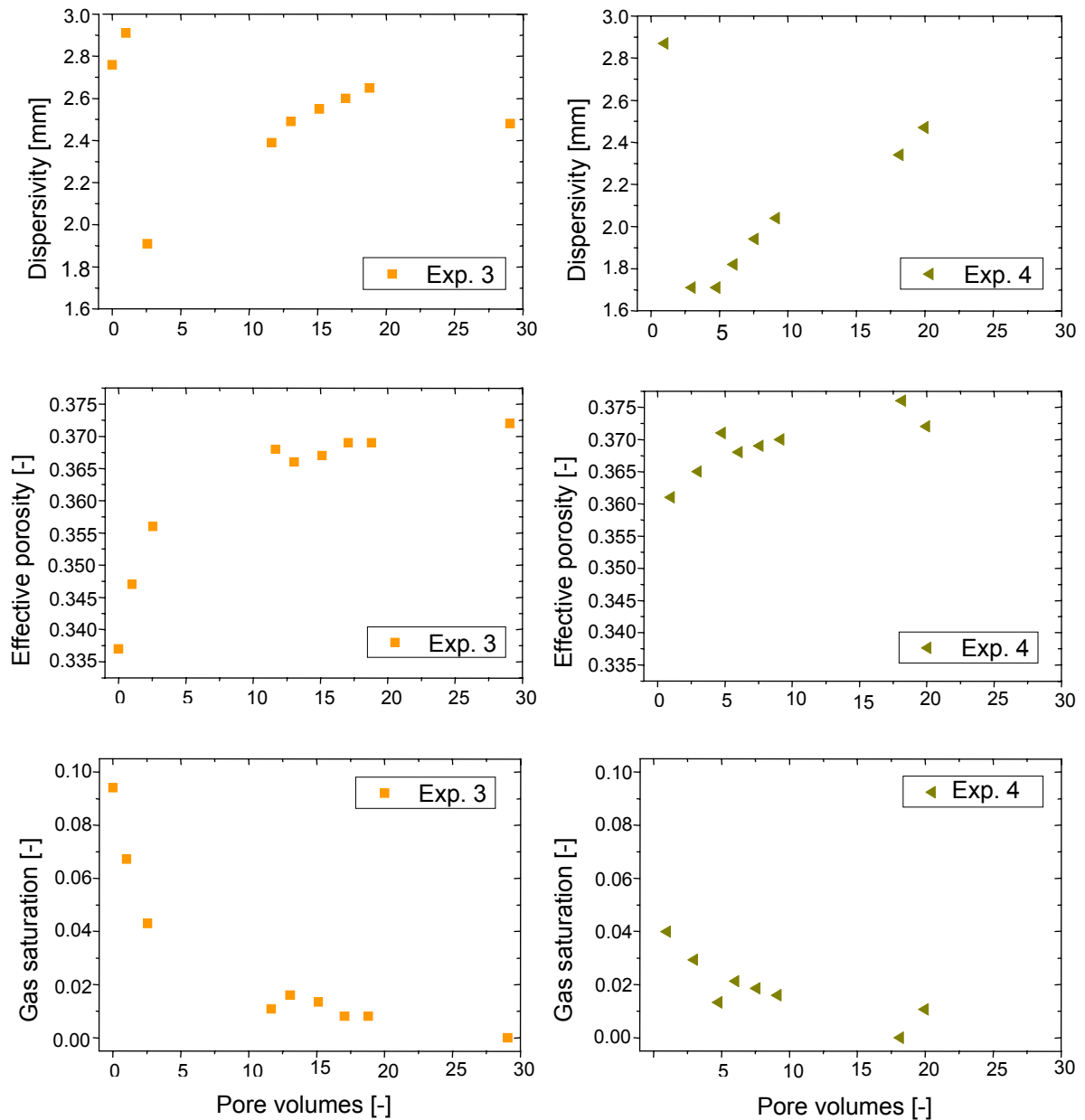


FIGURE 28: Longitudinal dispersivity, effective porosity and corresponding gas saturation determined by bromide tracer test during dissolution experiment 3 (orange squares) and 4 (light green triangles). For both experiments nitrogen was used as flushing gas.

The longitudinal dispersivity, the effective porosity, and the gas saturations determined from the bromide tracer tests are displayed in Figure 28 for experiments 3 and 4. In contrast to the experiments where helium was used to prepare the low oxygen solution, the dissolution experiments with nitrogen as flushing solution exhibit a minimum for the dispersivity during gas dissolution after approximately 2.5 pore volumes were exchanged. In the subsequent

progression the dispersivity increases continuously till the end of the experiment. For the maximum longitudinal dispersivity (determined at complete water saturation before the dissolution experiment) a value of $2.7 \text{ mm} \pm 0.2 \text{ mm}$ was determined for experiment 3 and a value of $2.8 \text{ mm} \pm 0.4 \text{ mm}$ was determined for experiment 4. The effective porosity as well as the corresponding gas saturations shows a similar progression to the hydraulic conductivity curves. For experiment 3 the effective porosity shows a steep increase, followed by a gently inclined curve progression. For experiment 4 the steep increase cannot be traced clearly due to the small number of data points at that part of the curve. The maximum effective porosity for experiment 3 was 0.372 ± 0.003 . For experiment 4 a value of 0.376 ± 0.003 was determined. The gas saturations computed from the effective porosity shows the reverse progression again.

5.1.3 Argon as Flushing Gas

The most significant experimental results for experiments 5 and 6 are listed in Table 7. The gravimetrically determined changes in gas volume in the column before the start of the dissolution experiment are displayed in Figure 29 for the two experiments using argon as flushing gas. For both experiments, a bromide tracer test was conducted at the time when the maximum residual gas saturation was reached. Therefore, both data sets had to be corrected by the bromide tracer mass as well as for the balance drift. For experiment 5 the gas injection started after approximately 0.01 days, for experiment 6 after 0.014 days.

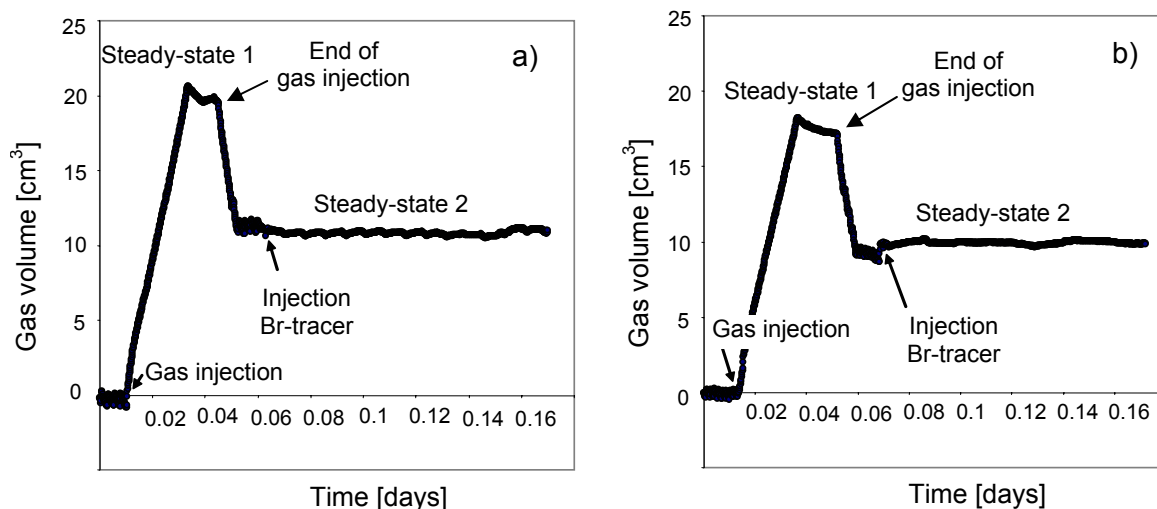


FIGURE 29: Gas volume in the column determined by gravimetric measurements before the start of the dissolution experiment for a) experiment 5 and b) experiment 6. The water flow rate for experiment 5 was $1.58 \text{ cm}^3/\text{min}$ and the gas flow rate was $1.30 \text{ cm}^3/\text{min}$. For experiment 6 a water flow rate of $1.54 \text{ cm}^3/\text{min}$ was applied and a gas flow rate of $1.50 \text{ cm}^3/\text{min}$. In both experiments argon was used as flushing gas and a bromide tracer test was conducted at the second steady-state condition.

TABLE 7: Parameters and results of experiments 5 and 6 (argon as flushing gas).

Parameter	Experiment 5	Experiment 6
Q_w [cm ³ /min]	1.58 ± 0.01	1.54 ± 0.01
Q_g [cm ³ /min] ¹	1.30	1.50
q_w [m/d]	6.34 ± 0.11	6.15 ± 0.08
u_w^{\max} [m/d] ²	16.9 ± 0.4	16.4 ± 0.3
$p_{\text{hyd,out}}$ [kPa] ³	6.9 ± 0.06	6.8 ± 0.08
p_{atm} [kPa] ⁴	101.6 ± 0.06	101.5 ± 0.09
T [°C] ⁵	11.4 ± 1	11.7 ± 1
Min. hydraulic conductivity [m/s] ⁶	$1.15 \cdot 10^{-4}$	$1.13 \cdot 10^{-4}$
Max. hydraulic conductivity [m/s] ⁷	$2.06 \cdot 10^{-4}$ ± $0.03 \cdot 10^{-4}$	$1.71 \cdot 10^{-4}$ ± $0.04 \cdot 10^{-4}$
Min. effective porosity [%] ⁸	35.2 ± 0.2	34.4 ± 0.2
Max. effective porosity [%] ⁹	37.6 ± 0.2	36.7 ± 0.2
Max. longitudinal dispersivity [mm] ⁹	2.7 ± 0.3	2.3 ± 0.1
Max. $S_{g,\text{grav}}$ [%] ¹⁰	8.5 ± 0.2	7.8 ± 0.3
Max. $S_{g,\text{tracer}}$ [%] ¹¹	6.4 ± 1.1	6.3 ± 1.2
$C_{\text{O}_2,w}$ [mg/l] ¹²	57.8 ± 0.45	61.3 ± 3.38
$C_{\text{O}_2,w}^{\text{ini}}$ [mg/l] ¹³	1.0	0.9

¹ gas flow rate during gas injection determined gravimetrically at the column outlet

² water flow velocity at complete water saturation calculated with the tot. porosity ($\phi_{\text{tot}} = 0.376$)

³ artificially applied hydrostatic pressure at column outflow

⁴ average atmospheric pressure during dissolution experiment

⁵ average temperature during dissolution experiment

⁶ determined by pressure measurements at maximum residual gas saturation

⁷ determined by pressure measurements at complete water saturation

⁸ determined by bromide tracer tests at maximum residual gas saturation

⁹ determined by bromide tracer tests at complete water saturation

¹⁰ maximum residual gas saturation determined by gravimetric measurements

¹¹ maximum residual gas saturation determined by bromide tracer tests

¹² oxygen concentration in the water phase at the begin of the dissolution experiment

¹³ oxygen concentration in flushing solution

After 0.034 days the first steady-state flow condition with dynamical gas saturation was established for experiment 5. The gas volume inserted into the column amounted to approximately 20.5 cm³ at that time. For experiment 6, the first steady-state condition with a dynamical gas volume of about 18 cm³ was reached after 0.037 days. The gravimetrically measured gas flow out of the column was determined after the gas breakthrough and amounted to 1.30 cm³/min for experiment 5 and 1.50 cm³/min for experiment 6 (Table 7). For experiment 5, the first steady-state flow condition was sustained for 15 minutes, for experiment 6 the gas injection was stopped after 20 minutes. The second steady-state flow condition with the residual gas saturation was reached after 0.053 d for experiment 5 and 0.06 d for experiment 6. As mentioned before, for both experiments a bromide tracer test was

conducted when the maximum residual gas saturation in the column was obtained. Again, the dissolution experiment was not started until the tracer test was finished.

The residual gas saturation was determined by two different methods for both experiments. For experiment 5, a residual gas volume of $10.8 \text{ cm}^3 \pm 0.18 \text{ cm}^3$ was determined from the gravimetric measurements, which corresponds to a maximum residual gas saturation of 0.085 ± 0.002 . The bromide tracer test conducted at maximum residual gas saturation resulted in an effective porosity of 0.352 ± 0.002 , the gas saturation computed from the tracer test was 0.064 ± 0.011 . For experiment 6, the residual gas volume determined by gravimetric measurements was $9.9 \text{ cm}^3 \pm 0.27 \text{ cm}^3$, resulting in a gas saturation of 0.078 ± 0.003 . From the bromide tracer tests an effective porosity of 0.344 ± 0.002 was determined for the second steady-state condition, corresponding to a maximum residual gas saturation of 0.063 ± 0.012 (Table 7).

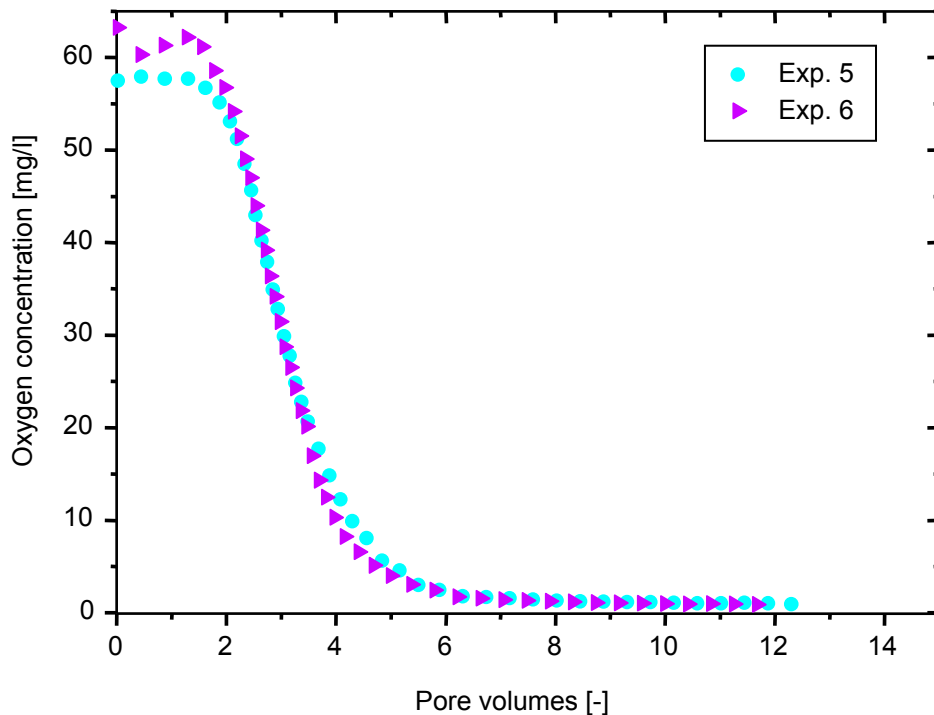


FIGURE 30: Dissolved oxygen concentration versus saturated pore volumes recorded at the column outlet during the dissolution of the injected oxygen gas phase for experiment 5 (light blue dots) and 6 (purple triangles). The water flow velocity determined from the gravimetric measurements was 16.9 m/d for experiment 5 and 16.4 m/d for experiment 6. In both experiments argon was used as flushing gas.

In Figure 30 the dissolved oxygen concentration curves recorded during the dissolution of the injected oxygen gas phase are presented for experiments 5 and 6. The water flow velocity in the column determined from the gravimetric measurements was $16.9 \text{ m/d} \pm 0.4 \text{ m/d}$ for

experiment 5 and $16.4 \text{ m/d} \pm 0.3 \text{ m/d}$ for experiment 6. The averaged oxygen concentration obtained at the plateau-like phase at the beginning of the dissolution experiment was $57.8 \text{ mg/l} \pm 0.45 \text{ mg/l}$ for experiment 5 and $61.3 \text{ mg/l} \pm 3.38 \text{ mg/l}$ for experiment 6 (Table 7). The progression of the dissolved oxygen concentration curves for experiments 5 and 6 (argon as flushing gas) is different from the progression of the other four experiments of this test series. In contrast to the steep decline of the oxygen curves of experiments 1 to 4, the two oxygen concentration curves in Figure 30 show a less steep decline after exchanging 2 pore volumes. Moreover, the dissolution of the trapped oxygen gas phase lasted longer (approximately 4 to 5 pore volumes compared to 3.5 pore volumes in experiments 1 to 4).

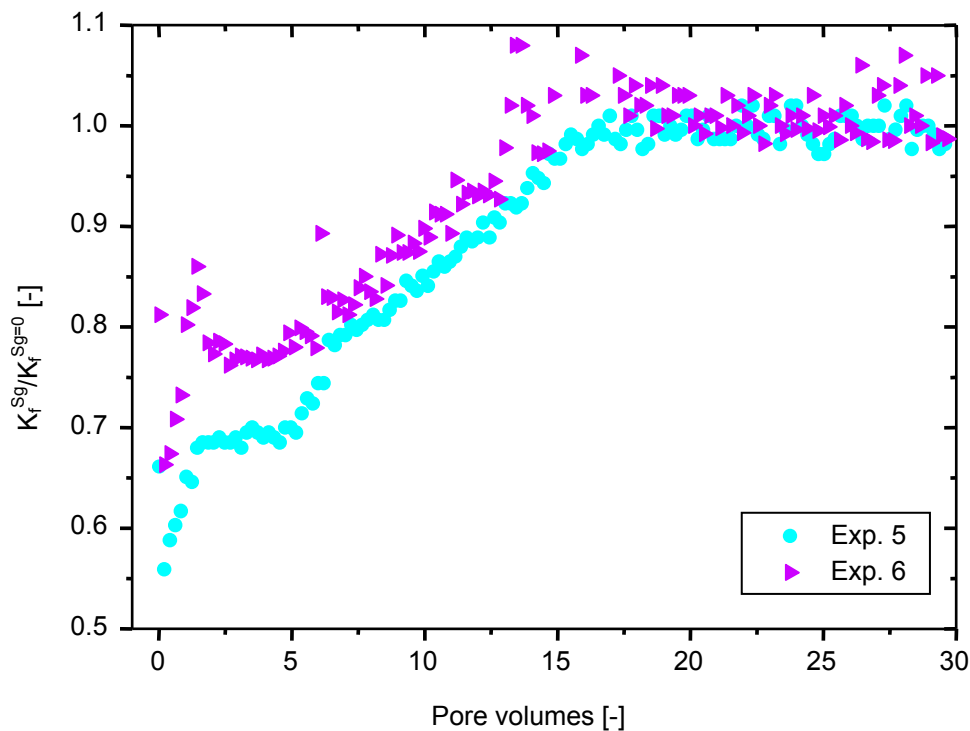


FIGURE 31: Normalized hydraulic conductivity plotted versus the saturated pore volumes for experiment 5 (light blue dots) and 6 (purple triangles) (argon used as flushing gas).

The normalized hydraulic conductivity versus saturated pore volumes for experiments 5 and 6 is shown in Figure 31. The progression of the hydraulic conductivity curves for experiments 5 and 6 is comparable to the hydraulic conductivity curves from experiments 3 and 4. Likewise a two-stage rise of the curves is observable during the dissolution experiment, though not as pronounced as in experiments 3 and 4. After a first steep increase at the beginning, the hydraulic conductivity curve passes into a slower rise at the exchange of approximately 2 pore

volumes. After 17 pore volumes were exchanged the curve finally reaches the plateau with the maximum hydraulic conductivity values indicating that complete water saturation is reached. The maximum hydraulic conductivity at complete water saturation was $2.06 \cdot 10^{-4} \text{ m/s} \pm 0.03 \cdot 10^{-4} \text{ m/s}$ for experiment 5 and $1.71 \cdot 10^{-4} \text{ m/s} \pm 0.04 \cdot 10^{-4} \text{ m/s}$ for experiment 6. Like in the experiments using nitrogen to prepare the low oxygen solution, there is still a certain amount of gas in the column at the time the trapped oxygen gas phase is completely dissolved. This residual gas phase dissolves slower in the bypassing water than the oxygen gas phase, but faster compared to the residual gas phase in experiments 3 and 4 (17 pore volumes compared to 22.5 pore volumes).

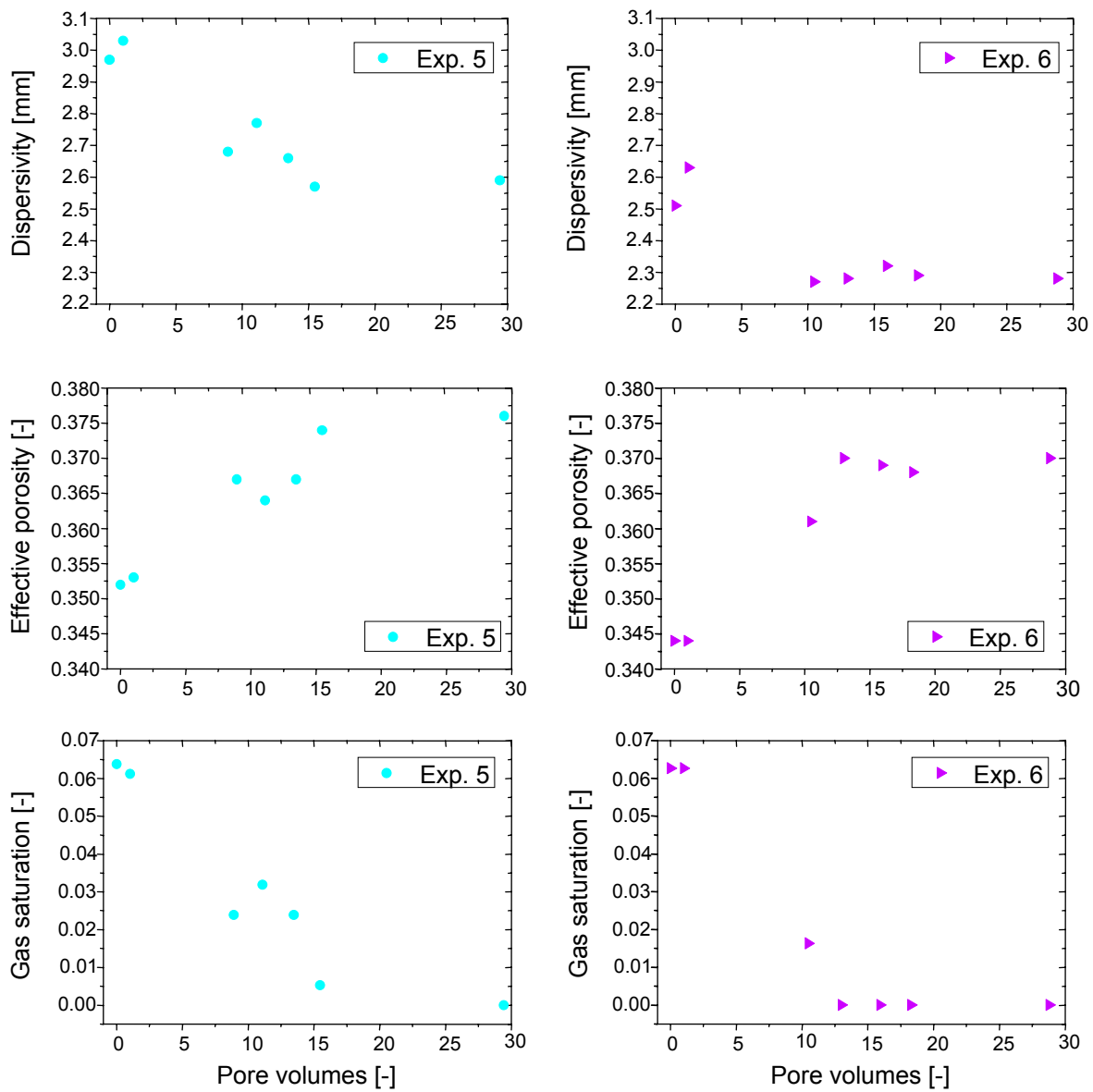


FIGURE 32: Longitudinal dispersivity, effective porosity and corresponding gas saturation determined by bromide tracer test during dissolution experiment 5 (light blue dots) and 6 (purple triangles). Argon was used as flushing gas.

The results of the bromide tracer tests conducted during the dissolution experiments 5 and 6 are shown in Figure 32. The longitudinal dispersivity apparently shows a different trend than in the other four experiments of this test series. After a maximum at the beginning of the dissolution experiment, a plateau is reached, at which the values scatter around a minimum value. However, a thorough comparison to experiments 1 to 4 is difficult, because of the small number of data points between 1 and 9 pore volumes. A value of $2.7 \text{ mm} \pm 0.3 \text{ mm}$ and $2.3 \text{ mm} \pm 0.1 \text{ mm}$ was determined for the maximum longitudinal dispersivity (determined at complete water saturation) for experiments 5 and 6, respectively.

The effective porosity as well as the corresponding gas saturations reflects quite well the results of the hydraulic conductivity curves. For the effective porosity, the steep increase at the beginning of the dissolution experiment cannot be followed due to the low frequency of data points at that part of the curve. Nevertheless, the effective porosity shows a gently inclined curve progression, until the plateau for the complete water saturation is reached. For experiment 5, a maximum effective porosity of 0.376 ± 0.002 was determined. For experiment 6, the maximum effective porosity was 0.367 ± 0.002 . Again, the gas saturations computed from the effective porosity show the reverse progression.

5.2 Test Series 2: Velocity Modifications

In a second test series, experiments with nitrogen as flushing gas were performed at reduced water flow rates. Nitrogen was selected since it is more abundant in natural aquifer systems than the trace gases helium and argon. Two experiments were conducted at a volumetric water flow rate of $0.4 \text{ ml/min} \pm 0.01 \text{ ml/min}$ and two at $0.8 \text{ ml/min} \pm 0.01 \text{ ml/min}$, which corresponds to a water flow velocity of 4 m/d and 9 m/d, respectively. Altogether, four additional experiments were performed:

- experiments 7 and 8 at a flow velocity of 9 m/d,
- experiments 9 and 10 at a flow velocity of 4 m/d.

5.2.1 Experiments at a Water Flow Velocity of 9 m/d

In Table 8 the most important experimental results for experiments 7 and 8 are listed. The changes in gas volume in the column calculated from gravimetric measurements before the start of the dissolution experiment are presented for experiments 7 and 8 in Figure 33. A bromide tracer test was performed for the state with the maximum residual gas saturation for both experiments, therefore both data sets had to be corrected by the bromide tracer mass as

well as for the balance drift (see Chapter 4.3.1). The gas injection was started after approximately 0.013 days in both experiments. The first steady-state flow condition with dynamical gas saturation was established after 0.059 d for experiment 7 and 0.063 d for experiment 8. The gas volume inserted into the column amounted to approximately 18.3 cm³ and 18.6 cm³ for experiments 7 and 8 at that time, respectively. As a result of the experimental setup, the reduction of the water flow rate resulted in a simultaneous reduction of the gas flow rate. The gravimetrically measured gas flow from the column determined after the gas breakthrough amounted to 0.37 cm³/min for experiment 7 and 0.41 cm³/min for experiment 8 (Table 8).

TABLE 8: Parameters and results of experiments 7 and 8 (nitrogen as flushing gas).

Parameter	Experiment 7	Experiment 8
Q_w [cm ³ /min]	0.80 ± 0.01	0.80 ± 0.01
Q_g [cm ³ /min] ¹	0.37	0.41
q_w [m/d]	3.19 ± 0.05	3.19 ± 0.05
u_w^{\max} [m/d] ²	8.5 ± 0.2	8.5 ± 0.2
$p_{\text{hyd,out}}$ [kPa] ³	7.1 ± 0.05	6.7 ± 0.07
p_{atm} [kPa] ⁴	101.8 ± 0.09	101.6 ± 0.05
T [°C] ⁵	11.4 ± 1	11.3 ± 1
Min. hydraulic conductivity [m/s] ⁶	$0.86 \cdot 10^{-4}$	$1.09 \cdot 10^{-4}$
Max. hydraulic conductivity [m/s] ⁷	$1.87 \cdot 10^{-4}$ ± $0.06 \cdot 10^{-4}$	$1.78 \cdot 10^{-4}$ ± $0.05 \cdot 10^{-4}$
Min. effective porosity [%] ⁸	34.4 ± 0.2	34.3 ± 0.1
Max. effective porosity [%] ⁹	36.8 ± 0.2	37.1 ± 0.1
Max. longitudinal dispersivity [mm] ⁹	1.8 ± 0.05	1.8 ± 0.05
Max. $S_{g,\text{grav}}$ [%] ¹⁰	8.6 ± 0.2	7.6 ± 0.2
Max. $S_{g,\text{tracer}}$ [%] ¹¹	6.5 ± 1.1	7.5 ± 0.6
$C_{O_2,w}$ [mg/l] ¹²	58.9 ± 1.30	58.4 ± 1.05
$C_{O_2,w}^{\text{ini}}$ [mg/l] ¹³	1.5	1.6

¹ gas flow rate during gas injection determined gravimetrically at the column outlet

² water flow velocity at complete water saturation calculated with the tot. porosity ($\phi_{\text{tot}} = 0.376$)

³ artificially applied hydrostatic pressure at column outflow

⁴ average atmospheric pressure during dissolution experiment

⁵ average temperature during dissolution experiment

⁶ determined by pressure measurements at maximum residual gas saturation

⁷ determined by pressure measurements at complete water saturation

⁸ determined by bromide tracer tests at maximum residual gas saturation

⁹ determined by bromide tracer tests at complete water saturation

¹⁰ maximum residual gas saturation determined by gravimetric measurements

¹¹ maximum residual gas saturation determined by bromide tracer tests

¹² oxygen concentration in the water phase at the begin of the dissolution experiment

¹³ oxygen concentration in flushing solution

The gas injection was stopped after maintaining the first steady-state flow condition for 20 minutes. For experiment 7, the second steady-state condition with the residual gas saturation was reached after 0.089 d, for experiment 8, the second steady-state condition was reached after 0.092 d. For both experiments a bromide tracer test was conducted when the condition with the maximum residual gas saturation was obtained and the dissolution experiment was not started until the bromide breakthrough curve was measured in the column outflow. The jump in the gas volume at the end of the second steady-state flow condition for experiment 8 displayed in Figure 33 b) was again caused by unintentional contacts with the balances.

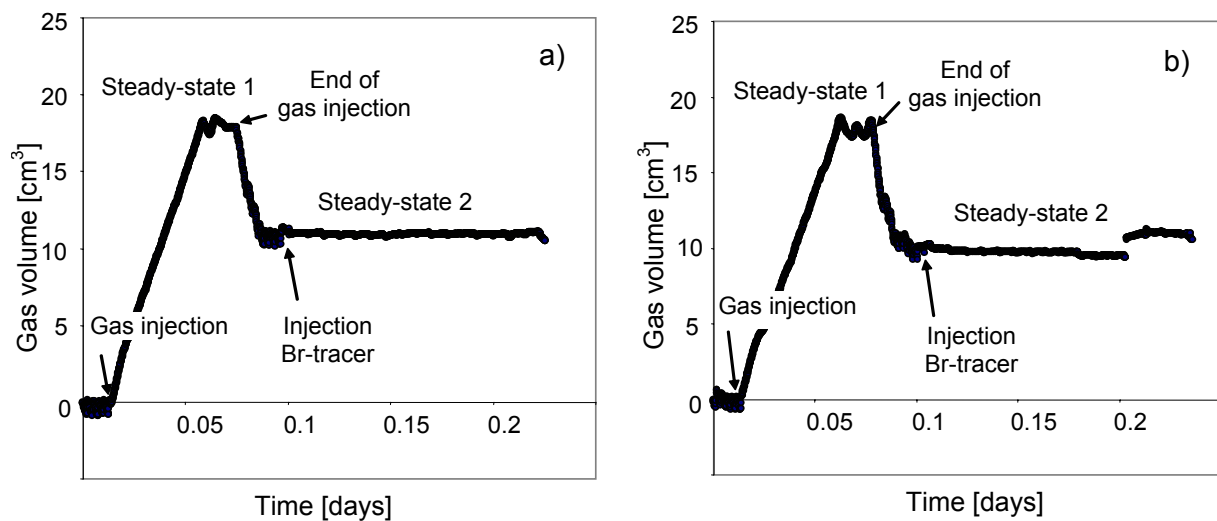


FIGURE 33: Gas volume in the column determined by gravimetric measurements before the start of the dissolution experiment for a) experiment 7 and b) experiment 8. The water flow rate for experiments 7 and 8 was $0.8 \text{ cm}^3/\text{min}$. The gas flow rate for experiment 7 was $0.37 \text{ cm}^3/\text{min}$ and for experiment 8 $0.41 \text{ cm}^3/\text{min}$. In both experiments nitrogen was used as flushing gas and a bromide tracer test was conducted at the second steady-state condition.

The residual gas saturation was determined by two different methods for both experiments. From the gravimetric measurements a maximum residual gas volume of $10.9 \text{ cm}^3 \pm 0.14 \text{ cm}^3$ was determined for experiment 7, corresponding to a maximum residual gas saturation of 0.086 ± 0.002 . The bromide tracer test yielded an effective porosity of 0.344 ± 0.002 for the state with maximum residual gas saturation. The gas saturation computed from the tracer test was 0.065 ± 0.011 . For experiment 8, a residual gas volume of $9.7 \text{ cm}^3 \pm 0.32 \text{ cm}^3$ was determined from the gravimetric measurements, which corresponds to a maximum residual gas saturation of 0.076 ± 0.002 . From the bromide tracer tests an effective porosity of 0.343

± 0.001 was determined for the second steady-state condition, corresponding to a maximum residual gas saturation of 0.075 ± 0.006 (Table 8).

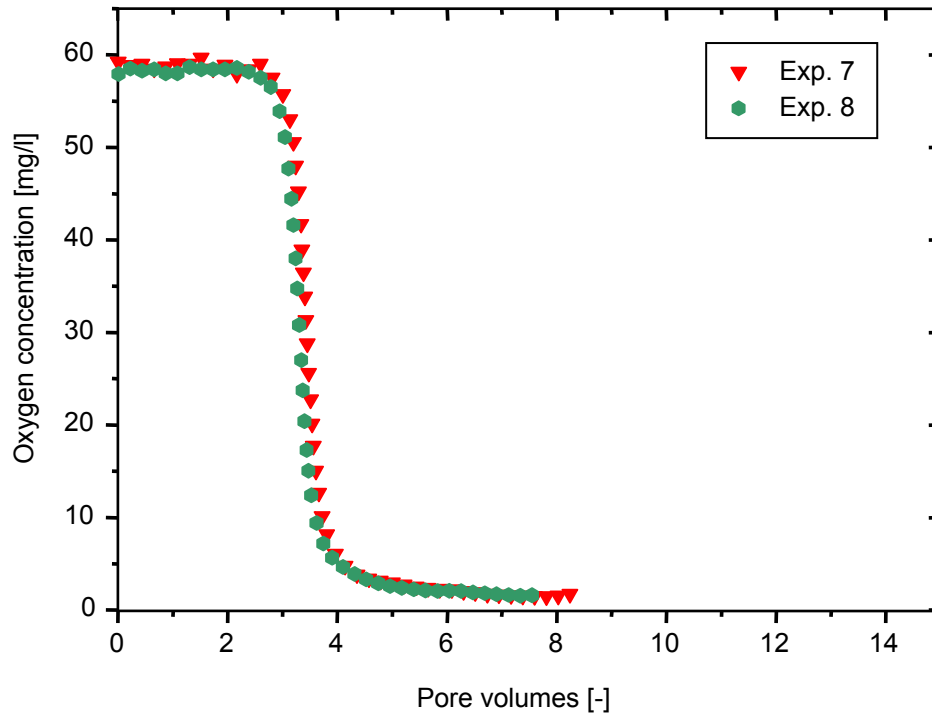


FIGURE 34: Dissolved oxygen concentration recorded at the column outlet versus saturated pore volumes for experiment 7 (red triangles) and 8 (green hexagons). The water flow velocity determined from the gravimetric measurements was 8.5 m/d for both experiments. Nitrogen was used as flushing gas.

The dissolved oxygen concentration curves of the actual dissolution experiment are displayed in Figure 34 for experiments 7 and 8. For both experiments, a water flow velocity of 8.5 m/d ± 0.2 m/d was determined from the gravimetric measurements (Table 8). As expected, the progression of the dissolved oxygen concentration curves for experiments 7 and 8 is similar to the progression of the curves likewise performed with nitrogen as flushing gas at a higher flow velocity (experiments 3 and 4). An averaged oxygen concentration of 58.9 mg/l ± 1.30 mg/l for experiment 7 and 58.4 mg/l ± 1.05 mg/l for experiment 8 was measured at the beginning of the dissolution experiment. The effluent dissolved oxygen concentration shows a steep decrease and reaches the feed concentration (about 1.54 mg/l for experiment 7 and 1.60 mg/l for experiment 8) after approximately 3.5 saturated pore volumes were exchanged, which marks the entire dissolution of the residual oxygen gas phase.

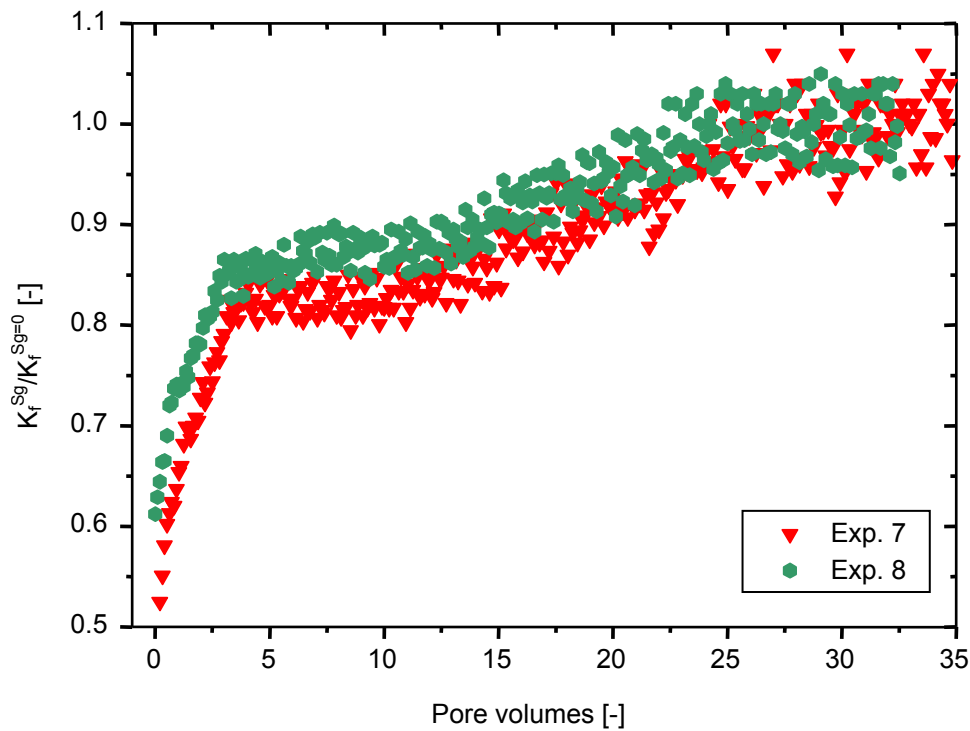


FIGURE 35: Trend of the normalized hydraulic conductivity plotted versus the saturated pore volumes for experiment 7 (red triangles) and 8 (green hexagons). For both experiments nitrogen was used as flushing gas.

Figure 35 shows the normalized hydraulic conductivity versus saturated pore volumes for experiments 7 and 8. Similar to experiments 3 and 4, both curves show a two-stage increase of the curve during the dissolution experiment. The hydraulic conductivity shows a steep increase at the beginning until the time when 3.5 pore volumes were exchanged, corresponding to the condition of complete dissolution of the oxygen gas phase.

Following the steep increase, the hydraulic conductivity curves exhibit a slower rise until after approximately 24 pore volumes were exchanged the curve finally reaches the plateau with the maximum hydraulic conductivity values indicating that complete water saturation is reached. At complete water saturation, the curves show a wider distribution of the values compared to the experiments conducted at a higher flow velocity. This is caused by the increasing interferences at decreasing flow velocities mentioned in Chapter 4.3.3. For experiment 7, the maximum hydraulic conductivity at complete water saturation was $1.87 \cdot 10^{-4} \text{ m/s} \pm 0.06 \cdot 10^{-4} \text{ m/s}$. For experiment 8, a value of $1.78 \cdot 10^{-4} \text{ m/s} \pm 0.05 \cdot 10^{-4} \text{ m/s}$ was obtained. Like in the experiments performed with nitrogen as flushing gas at a higher flow velocity, there is still a certain amount of gas in the column when the trapped oxygen gas phase is completely

dissolved. Again, this residual gas phase dissolves much slower in the bypassing water than the oxygen gas phase.

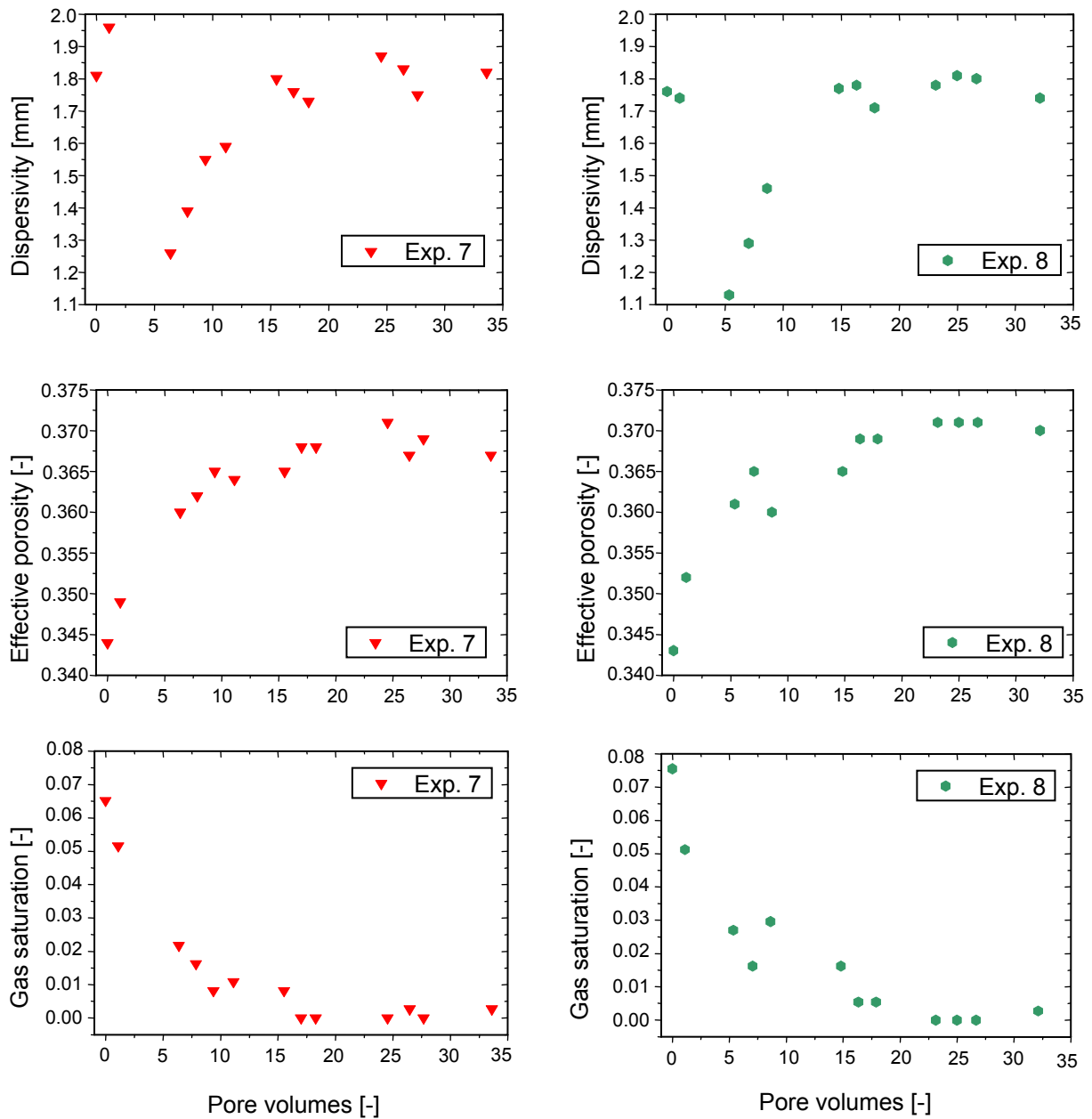


FIGURE 36: Longitudinal dispersivity, effective porosity and corresponding gas saturation determined by bromide tracer test during dissolution experiment 7 (red triangles) and 8 (green hexagons). Nitrogen was used as flushing gas.

In Figure 36 the longitudinal dispersivity, the effective porosity, and the gas saturations determined from the bromide tracer tests are presented for experiments 7 and 8. The dispersivity curves show a clear minimum at the beginning of the dissolution experiments (after approximately 5 pore volumes were exchanged) similar to experiments 3 and 4. After

this minimum the dispersivity increases continuously till the end of the experiment. For the maximum longitudinal dispersivity (determined at complete water saturation) a value of $1.8 \text{ mm} \pm 0.05 \text{ mm}$ was determined for both experiments.

The effective porosity and the corresponding gas saturations clearly reflect the results of the hydraulic conductivity curves. The progression of the effective porosity shows a steep increase followed by a gently inclined curve progression. Then a plateau is reached, at which the values scatter around a maximum value, indicating complete water saturation. The maximum effective porosity for experiment 7 was 0.368 ± 0.002 . For experiment 8, a value of 0.371 ± 0.001 was determined. The gas saturations computed from the effective porosity show a reverse progression.

5.2.2 Experiments at a Water Flow Velocity of 4 m/d

In Table 9 the main experimental results are listed for experiments 9 and 10.

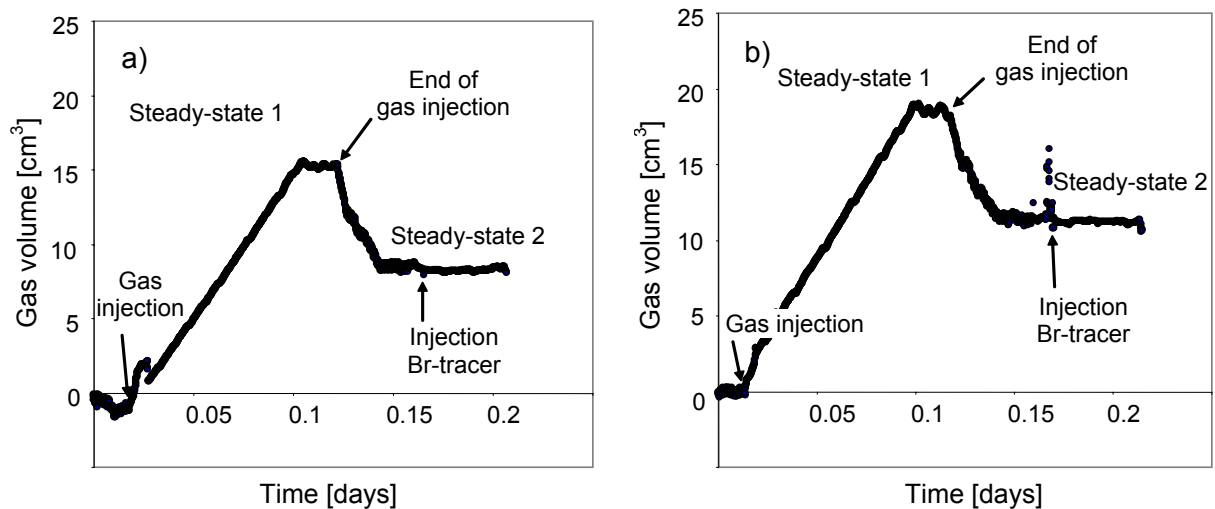


FIGURE 37: Gas volume in the column determined by gravimetric measurements before the start of the dissolution experiment for a) experiment 9 and b) experiment 10. The water flow rate for experiment 9 was $0.40 \text{ cm}^3/\text{min}$ and the gas flow rate was $0.11 \text{ cm}^3/\text{min}$. For experiment 10 a water flow rate of $0.41 \text{ cm}^3/\text{min}$ was applied and a gas flow rate of $0.20 \text{ cm}^3/\text{min}$. In both experiments nitrogen was used as flushing gas and a bromide tracer test was conducted at the second steady-state condition.

The changes in gas volume in the column calculated from gravimetric measurements before the start of the dissolution experiment are displayed in Figure 37 for the two experiments conducted at a flow velocity of 4 m/d. Both data sets were corrected by the bromide tracer mass as well as for the balance drift. The gas injection started after approximately 0.013 days

and 0.017 days for experiments 9 and 10, respectively. After 0.106 days the first steady-state flow condition with dynamical gas saturation was established for experiment 9. The gas volume inserted into the column amounted to approximately 15.5 cm³ at that time. For experiment 10, the first steady-state condition with a dynamical gas volume of about 19 cm³ was reached after 0.099 days. Again, the reduction of the water flow rate resulted in a simultaneous reduction of the gas flow rate. The gravimetrically measured gas flow from the column determined after the gas breakthrough was 0.11 cm³/min for experiment 9 and 0.20 cm³/min for experiment 10 (Table 9).

TABLE 9: Parameters and results of experiments 9 and 10 (nitrogen as flushing gas).

Parameter	Experiment 9	Experiment 10
Q_w [cm ³ /min]	0.40 ± 0.01	0.41 ± 0.01
Q_g [cm ³ /min] ¹	0.11	0.20
q_w [m/d]	1.59 ± 0.04	1.63 ± 0.06
u_w^{\max} [m/d] ²	4.2 ± 0.1	4.3 ± 0.2
$p_{\text{hyd,out}}$ [kPa] ³	7.1 ± 0.06	7.0 ± 0.06
p_{atm} [kPa] ⁴	102.6 ± 0.2	101.6 ± 0.4
T [°C] ⁵	12.1 ± 1	11.5 ± 1
Min. hydraulic conductivity [m/s] ⁶	-	-
Max. hydraulic conductivity [m/s] ⁷	-	-
Min. effective porosity [%] ⁸	34.7 ± 0.3	35.0 ± 0.3
Max. effective porosity [%] ⁹	37.6 ± 0.2	37.6 ± 0.2
Max. longitudinal dispersivity [mm] ⁹	1.7 ± 0.2	1.8 ± 0.1
Max. $S_{g,\text{grav}}$ [%] ¹⁰	6.5 ± 0.2	8.9 ± 0.4
Max. $S_{g,\text{tracer}}$ [%] ¹¹	7.7 ± 1.4	6.9 ± 1.4
$C_{O_2,w}$ [mg/l] ¹²	58.8 ± 1.04	56.9 ± 0.89
$C_{O_2,w}^{\text{ini}}$ [mg/l] ¹³	2.4	2.3

¹ gas flow rate during gas injection determined gravimetrically at the column outlet

² water flow velocity at complete water saturation calculated with the tot. porosity ($\phi_{\text{tot}} = 0.376$)

³ artificially applied hydrostatic pressure at column outflow

⁴ average atmospheric pressure during dissolution experiment

⁵ average temperature during dissolution experiment

⁶ determined by pressure measurements at maximum residual gas saturation

⁷ determined by pressure measurements at complete water saturation

⁸ determined by bromide tracer tests at maximum residual gas saturation

⁹ determined by bromide tracer tests at complete water saturation

¹⁰ maximum residual gas saturation determined by gravimetric measurements

¹¹ maximum residual gas saturation determined by bromide tracer tests

¹² oxygen concentration in the water phase at the begin of the dissolution experiment

¹³ oxygen concentration in flushing solution

For both experiments, the first steady-state flow condition was sustained for 25 minutes, before the gas injection was stopped. The second steady-state condition with the residual gas

saturation was reached after 0.144 d for experiment 9 and 0.143 d for experiment 10. A bromide tracer was injected at maximum residual gas saturation (second steady-state flow condition) for both experiments. Due to the low water flow velocities applied in these two experiments, the time for complete bromide tracer breakthrough was quite long. Therefore, the dissolution experiment was started before the tracer curve was entirely recorded at the column outflow. The data for the analysis of the bromide tracer performed at maximum residual gas saturation was partly taken from the measurements of the dissolution experiment. Consequently, the bromide tracer curve consists of the bromide concentrations measured before and during the dissolution experiment. That way, the residual gas saturation could again be determined by two different methods for both experiments.

For experiment 9 a residual gas volume of $8.3 \text{ cm}^3 \pm 0.16 \text{ cm}^3$ was determined from the gravimetric measurements, which corresponds to a maximum residual gas saturation of 0.065 ± 0.002 . The bromide tracer test conducted at maximum residual gas saturation resulted in an effective porosity of 0.347 ± 0.003 , the gas saturation computed from the tracer test was 0.077 ± 0.014 . For experiment 10, the residual gas volume was $11.3 \text{ cm}^3 \pm 0.44 \text{ cm}^3$, resulting in a gas saturation of 0.089 ± 0.004 . The bromide tracer test yielded an effective porosity of 0.35 ± 0.003 for the time, on which the maximum residual gas saturation was prevailed in the column. The gas saturation computed from the tracer test was 0.069 ± 0.014 (Table 9).

Figure 38 shows the dissolved oxygen concentration curves recorded at the column outlet for experiments 9 and 10. From the gravimetric measurements a water flow velocity of $4.2 \text{ m/d} \pm 0.1 \text{ m/d}$ was determined for experiment 9 and $4.3 \text{ m/d} \pm 0.2 \text{ m/d}$ for experiment 10 (Table 9).

The progression of the dissolved oxygen concentration curves for experiments 9 and 10 is similar to the progression of the curves performed with nitrogen as flushing gas at a flow velocity of 17 and 9 m/d. At the beginning of the dissolution experiment the average oxygen concentration measured for experiment 9 was $58.8 \text{ mg/l} \pm 1.04 \text{ mg/l}$ and $56.9 \text{ mg/l} \pm 0.89 \text{ mg/l}$ for experiment 10. After approximately 3.5 saturated pore volumes were exchanged, the effluent dissolved oxygen concentration shows a steep decline and reaches concentrations identical to that in the flushing solution (feed concentration; about 2.35 mg/l) after the exchange of approximately 4 pore volumes. Consequently, after this time the residual oxygen gas phase was completely dissolved.

As mentioned in Chapter 4.3.3, for the experiments conducted at a flow velocity of 4 m/d the pressure measurements in the column cap were not stable enough as a result of the increased interference. Therefore, the hydraulic conductivity measurements could not be displayed for experiments 9 and 10. Nevertheless, as shown in the previous results, the effective porosity

and the corresponding gas saturations reflect the results of the hydraulic conductivity curves quite well and can be taken as an indicator for the trend of the normalized hydraulic conductivity. The results of the bromide tracer tests conducted during the dissolution experiments 9 and 10 are shown in Figure 39.

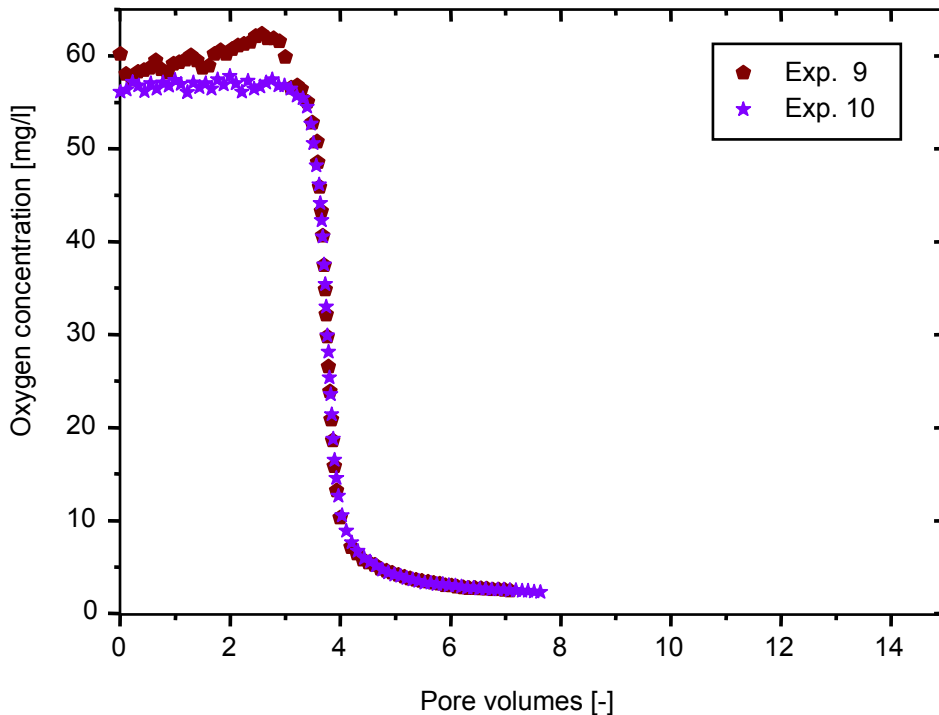


FIGURE 38: Dissolved oxygen concentration versus saturated pore volumes recorded at the column outlet during the dissolution of the injected oxygen gas phase for experiment 9 (brown pentagons) and 10 (lilac stars). The water flow velocity determined from the gravimetric measurements was 4.2 m/d for experiment 9 and 4.3 m/d for experiment 10. In both experiments nitrogen was used as flushing gas.

Regarding the effective porosity, a two-stage increase of the curve during the dissolution experiment is indicated quite well. Whereas the steep increase at the beginning of the dissolution experiment cannot be followed entirely due to the low frequency of data points at that part of the curve, the following gently inclined curve progression as well as the plateau for the complete water saturation is clearly pronounced. The maximum effective porosity was reached for both experiments after approximately 22.5 pore volumes were exchanged and amounted to 0.376 ± 0.002 . The gas saturations computed from the effective porosity show a reverse progression.

The minimum of the dispersivity curves at the beginning of the dissolution experiments (after the exchange of approximately 5 pore volumes) is even more distinct than in experiments 7 and 8. In the subsequent progression the dispersivities increase continuously until they reach

their maximum values at approximately 15 saturated pore volumes were exchanged. For the maximum longitudinal dispersivity (determined at complete water saturation) a value of $1.7 \text{ mm} \pm 0.2 \text{ mm}$ was determined for experiment 9 and a value of $1.8 \text{ mm} \pm 0.12 \text{ mm}$ was determined for experiment 10.

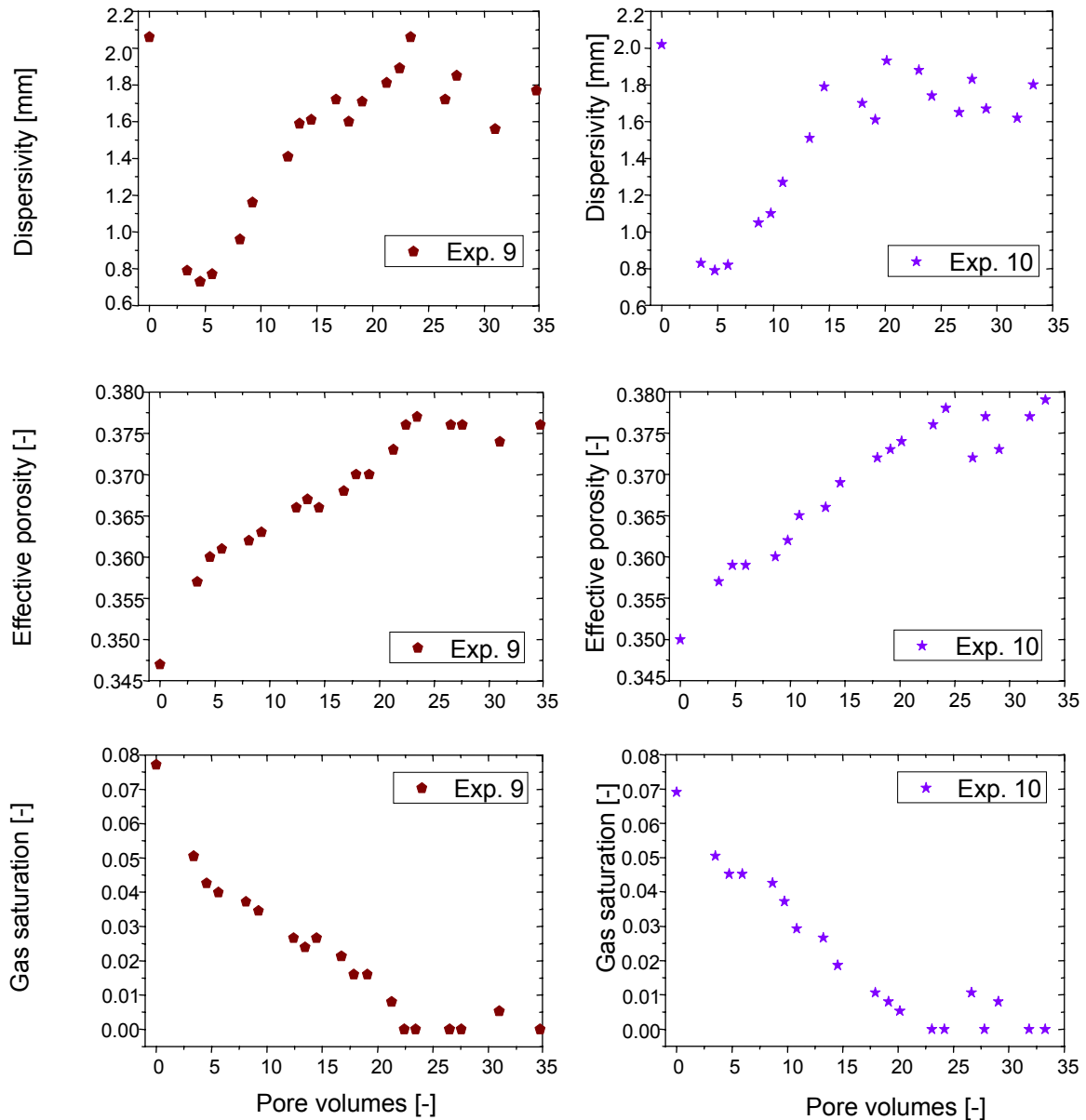


FIGURE 39: Longitudinal dispersivity, effective porosity and corresponding gas saturation determined by bromide tracer test during dissolution experiment 9 (brown pentagons) and 10 (lilac stars). Nitrogen was used as flushing gas.

5.3 Discussion of the Experimental Results

In Table 10 the most important results of the experiments are listed.

TABLE 10: Summary of parameters and results for all experiments.

Parameter	Exp. 1	Exp. 2	Exp. 3	Exp. 4	Exp. 5	Exp. 6	Exp. 7	Exp. 8	Exp. 9	Exp. 10
Flushing gas	He	He	N ₂	N ₂	Ar	Ar	N ₂	N ₂	N ₂	N ₂
U_w^{\max} [m/d] ¹	17	17	17	17	17	16	9	9	4	4
$S_{g,grav}^{\max}$ [%] ²	8.2	7.5	7.7	8.3	8.5	7.8	8.6	7.6	6.5	8.9
$C_{O_2,w}^{\exp}$ [mg/l] ³	57.5	56.9	58.1	58.3	57.8	61.3	58.9	58.4	58.8	56.9
$C_{O_2,w}^{\text{theor}}$ [mg/l] ⁴	57.4	57.1	57.7	57.2	57.3	56.8	57.5	57.4	57.1	57.2
K_f^{\max} [m/s] ⁵ ($\cdot 10^{-4}$)	2.12	2.18	1.84	1.88	2.06	1.71	1.87	1.78	-	-
ϕ_{eff}^{\max} [%] ⁶	37.8	37.1	37.2	37.6	37.6	36.7	36.8	37.1	37.6	37.6
α_l^{\max} [mm] ⁷	2.7	2.7	2.7	2.8	2.7	2.3	1.8	1.8	1.7	1.8
$K_f^{(S_g=\max)}/K_f^{(S_g=0)}$ ⁸	0.54	0.52	0.66	0.59	0.56	0.66	0.46	0.61	-	-

¹ water flow velocity at complete water saturation calculated with the tot. porosity ($\phi_{\text{tot}} = 0.376$)

² maximum residual gas saturation determined by gravimetric measurements

³ experimentally determined O₂-conc. in the water phase at the begin of the dissolution experiment

⁴ theoretical O₂-conc. in the water phase at the begin of the dissolution experiment

⁵ maximum hydraulic conductivity determined by pressure measurements at complete water saturation

⁶ maximum effective porosity determined by bromide tracer tests at complete water saturation

⁷ maximum longitudinal dispersivity determined by bromide tracer tests at complete water saturation

⁸ relative hydraulic conductivity

The same sand filled column was used in all ten experiments and the sediment was dynamically compressed in the column. Therefore, the possibility of grain rearrangements during and in between the single experiments can be excluded, which is confirmed by the good reproducibility of the curves performed at similar initial conditions.

One of the main questions of this work was what amount of gas could be captured in the pore space during direct oxygen injection. This question was answered by computing the experimental maximum gas saturations from two independent methods: From gravimetric measurements and from bromide tracer tests. In general, the values determined from the gravimetric measurements showed clearly smaller standard deviations than the values calculated from the bromide tracer tests. The corrections of the balance drift and the injected bromide tracer mass (see Chapter 4.3.1) resulted in an averaged standard deviation of 3.5 % for the maximum gas saturation computed from the gravimetric measurements, whereas the averaged standard deviation for the maximum residual gas saturation determined from

bromide tracer tests at the second steady-state condition was about 16.4 %. This high standard deviation is a result of error propagation, since the parameters determining the maximum gas saturation could not be measured directly via the bromide tracer tests (see Appendix 4). Furthermore, the maximum gas saturations could not be determined from bromide tracer tests for all experiments, since for experiments 1, 2 and 4 no bromide tracer test was performed at maximum residual gas saturation. Therefore, the maximum gas saturation determined from the gravimetric measurements will be considered in the following. Moreover, those values were taken as input parameter for the model application.

Regarding the gas injection, all ten experiments were performed under similar conditions, except for the water and gas flow rate. From the gravimetric measurements an average maximum residual gas saturation of 0.08 with a standard deviation of 8.7 % was determined for all ten experiments. No dependency of the achievable maximum gas saturation from the water and gas flow rate applied in the experiments was observed. The obtained values are smaller than the values attained in column experiments from Fry et al. (1997). Fry et al. performed a direct gas injection in fine, medium and coarse sand under high injection pressures and high gas flow rates and reported a gas saturation of 0.14 to 0.17. However, the sediment was not dynamically compressed in those experiments, leading to the assumption that the high gas saturations were achieved due to grain rearrangements during gas injection. In column experiments conducted by Weber (2000) a uniform gas saturation of 0.02 was determined for a punctiform direct gas injection in fine, medium and coarse sand. The residual gas saturation was increased in those experiments when gas was injected laminar over the entire column inlet, with a gas saturation of 0.03 and 0.06 being achieved for fine and medium sand, respectively. However, the column used in his experiments had a much greater diameter and volume (column diameter: 23.6 cm, column volume: 21872 cm³), therefore the gas and water flow cannot be considered as being one-dimensional as in the experiments performed in this work. The specific evaluation of all these data leads to the conclusion that the resulting maximum residual gas saturations achieved by the various authors (including this study) cannot be directly compared because all the studies had different column dimensions and experimental set ups as well as different gas injection rates.

Considering the time needed for the complete dissolution of the trapped oxygen gas phase in the column and the resulting effluent dissolved oxygen concentrations, quite similar results were obtained for all ten experiments. The dissolution of the trapped oxygen gas phase depended mainly on the residual gas saturation achieved in the single experiments. According to the data obtained from the gravimetric measurements, the variation in the maximum

residual gas saturation was relatively small. The dissolution of the trapped oxygen gas phase lasted until approximately 3.5 to 4 pore volumes were exchanged for all experiments regardless of the flow velocity. Differences arose mainly from the influence of different dissolved gases in the water phase. In Figure 40 the progression of the dissolved oxygen concentration curves are compared for the experiments performed with nitrogen as the flushing gas for different water flow velocities. The oxygen curves align quite well, however, there is a small offset between the curves of the experiments conducted at 9 and 4 m/d. This offset can be a result of the velocity dependency of the mass transfer (see Chapter 3.1.2.2).

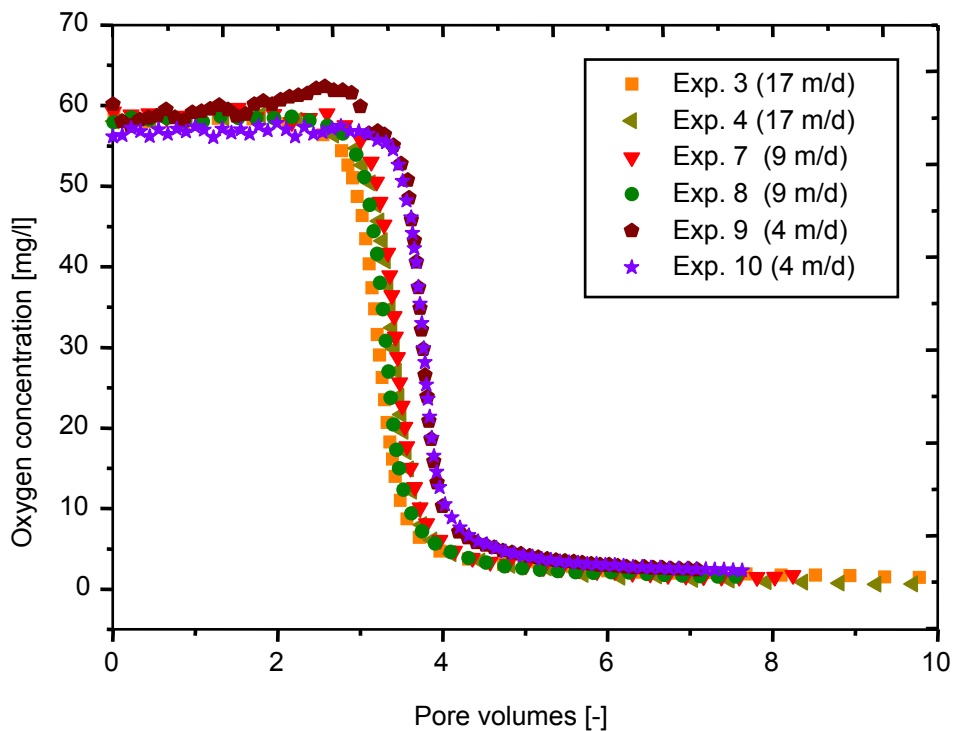


FIGURE 40: Effluent dissolved oxygen concentration curves for the experiments performed with nitrogen as flushing gas (water flow velocities are given in the legend).

The dissolved oxygen concentrations measured in the outflow of the column depended on the actual air pressure, the hydrostatic pressure applied on the column outlet, and the temperature. An average value of 58.3 mg/l with a standard deviation of 2.2 % was measured as maximum effluent dissolved oxygen concentration for all ten experiments. The experimentally determined values agree well with the theoretical values calculated for the particular pressure and temperature (Table 10), indicating that the water leaving the column was oxygen saturated. This leads to the assumption that the gas phase was in equilibrium with the water phase for the main part of the dissolution process for all ten experiments. That is the reason

why the dissolved oxygen concentrations at the column outlet stayed at saturated values until the dissolution front reached the column end. After the oxygen gas phase was completely dissolved, the effluent dissolved oxygen concentrations curves show a relatively steep decline and reach feed concentrations.

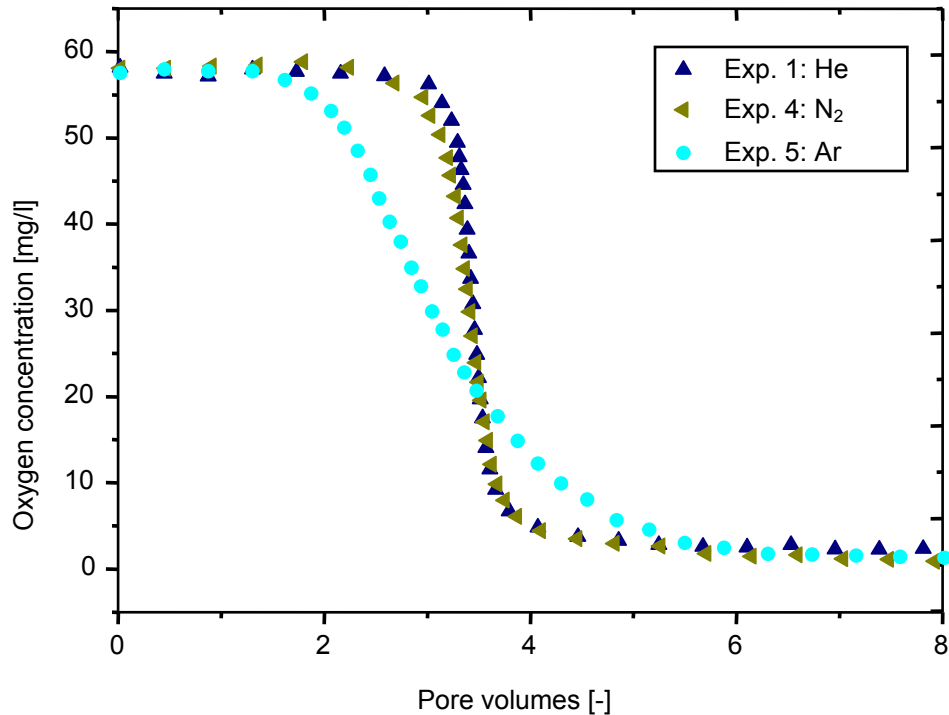


FIGURE 41: Effluent dissolved oxygen concentration versus saturated pore volumes for experiment 1 (dark blue triangles), experiment 4 (light green triangles) and experiment 5 (light blue dots) (flushing gases used to produce the low oxygen solution are given in the legend).

The effect of various gases (argon, nitrogen, helium) already dissolved in the mobile water phase on the dissolution process was investigated in test series 1 for a flow velocity of approximately 17 m/d. To allow a better comparison of the results, one oxygen curve for each flushing gas is presented in Figure 41. Experiments 1, 4, and 5 were chosen, since they exhibit the most similar maximum residual gas saturations determined by gravimetric measurements. The Figure shows clearly that the flushing solutions used in the experiments had a different effect on the dissolution process of the trapped oxygen gas phase. When helium and nitrogen were used as flushing gases, the dissolution curves show a similar progression, whereas the use of argon exhibits qualitatively different dissolution behaviour. The dissolved oxygen concentration curve in experiment 5 shows a relatively flat decline and the complete dissolution of the oxygen gas phase lasted longer compared to experiments 1 and 4. With

helium and nitrogen as flushing gas, the oxygen gas phase dissolved faster and the curves show a steeper decline.

As stated beforehand, not only the oxygen from the gas bubble is transferred to the water phase, but the dissolved flushing gases are transferred into the gas phase as well whereby the partial pressure of oxygen in the gas bubble is changed. That in turn interferes with the continuing dissolution process of the trapped gas phase. The different properties of the flushing gases lead to a diverse influence on the gas dissolution. As described in Chapter 3, the mass transfer of each gas depends mainly on the diffusion of the gas through the water surrounding the gas bubble. Each gas has a different temperature-dependent diffusion coefficient in water (see Table 11). The mass transfer also depends on the concentration gradient between the gas and water phase. The concentration gradient in the experiments performed in this work was given by the initial conditions. The flushing solutions were saturated with the different gases at atmospheric pressure. Depending on its solubility in water, the concentration of the gas and thus the total quantity in the water varies for the different gases (Table 11).

TABLE 11: Physico-chemical properties for oxygen and flushing gases.

Gas	Diffusion coefficient in water (10 °C) [cm ² /s]	Dimensionless Henry's law constant ¹ (10 °C) [-]	C _w for pure gas ² (10 °C, 1 atm) [mmol/l]
He ³	5.7 · 10 ⁻⁵	107.1	0.40
Ar ⁴	1.6 · 10 ⁻⁵	23.1	1.87
O ₂ ⁵	1.6 · 10 ⁻⁵	27.6	1.71
N ₂ ⁶	1.3 · 10 ⁻⁵	50.8	0.85

¹ values for all gases taken from CRC-Handbook, 1998

² maximum soluble concentration of pure gas in water

³ diffusion coefficient and C_w for He taken from Jähne et al., 1987.

⁴ diffusion coefficient and C_w for Ar taken from Oshumi & Horibe, 1984

⁵ diffusion coefficient and C_w for O₂ taken from Boudreau, 1997

⁶ diffusion coefficient and C_w for N₂ taken from Hayduk & Laudie, 1974

Considering helium for example, it is transferred faster into the gaseous phase than oxygen is dissolved in the aqueous phase due to its higher diffusion coefficient. Nevertheless, the influence of the helium transfer on the dissolution of oxygen is almost negligible compared to the other flushing gases. This is a result of the solubility-controlled changes in the relative gas composition of the trapped gas phase. Helium has a much lower abundance in the water phase because of its low aqueous solubility (approximately 0.40 mmol/l). Therefore, the amount of helium transferred to the gas phase is relative small in contrast to the amount of oxygen in the

gas phase. Compared to helium, oxygen can be dissolved in water in almost fourfold quantity, meaning that only a quarter of the oxygen, leaving the gas phase, is replaced by helium. Hence there will be a significant volume decrease in the gas bubbles and the relative contribution of oxygen to the gas composition remains higher than that of helium. Consequently, the dissolution process proceeds under higher oxygen partial pressure, therefore significantly faster.

Nitrogen has a slightly smaller diffusion coefficient than oxygen (Table 11). It is transferred more slowly into the gaseous phase than oxygen is transferred into the water phase. Moreover, the solubility of nitrogen in water is less than half compared to oxygen. However, the influence on the dissolution of oxygen is stronger as when using helium as flushing gas, since the solubility of nitrogen is approximately two times larger than that of helium. Subsequently, a larger amount of nitrogen degasses into the gas bubbles.

Argon possesses the same diffusion coefficient in water than oxygen (Table 11) and has nearly the same solubility in water. Hence, argon is available in distinctly higher quantity compared to helium and nitrogen. It has thus the strongest effect on the dissolution of oxygen of all three flushing gases used in this work. The partial pressure in the gas bubble changes substantially through the transfer of argon into the bubble. The number of argon moles, that transfer from the water into the gas phase is similar to the number of oxygen moles leaving the gas bubble. Therefore, the gas volume remains almost constant, leading to a decrease in the partial pressure of oxygen and thus to a slower dissolution process.

Due to the experimental set up, the phase transfer from the gas into the water phase is slightly favoured in the column experiments performed in this work. The oxygen gas has to overcome a certain pressure during the gas injection (hydrostatic and capillary pressure), resulting in an elevated pressure ratio in the gas bubbles, whereas the flushing solution is equilibrated at atmospheric pressure.

The effect of different dissolved gases on the dissolution of oxygen gas in water was also investigated by Bae et al. (1995). However, they compared a two-component system (oxygen/nitrogen) with a multi-component system (oxygen/air). Therefore, a comparison with the experiments performed in this work – considering only two-component systems – is difficult. Bae et al. (1995) also examined the influence of different dissolved nitrogen concentrations on the oxygen dissolution process. They describe a decreasing oxygen dissolution with an increase in the dissolved nitrogen concentrations. The flushing solutions used in this work were saturated with the different gases, consequently, the oxygen dissolution observed in the experiments performed can be considered as the minimal

achievable oxygen dissolution. When using flushing solutions with a lower partial pressure of gases, an increasing oxygen dissolution can be expected according to the experiments conducted by Bae et al. (1995).

In all experiments the trapped oxygen gas phase was dissolved completely. However, from the hydraulic conductivity measurements as well as from the gas saturation data calculated from the bromide tracer test it could be noted that for the experiments where nitrogen and argon was used as flushing gas the time to reach maximal hydraulic conductivity i.e. complete water saturation was significantly larger than the time needed for complete oxygen removal. There was still a certain amount of gas in the column after the entire dissolution of the trapped oxygen gas phase. This residual gas phase consisted of the flushing gas that was transferred from the water phase into the gas bubbles during the dissolution of the oxygen gas phase. In Figure 42 an example of the normalized hydraulic conductivity is shown for one experiment for each flushing solution (experiments 1, 4, and 5).

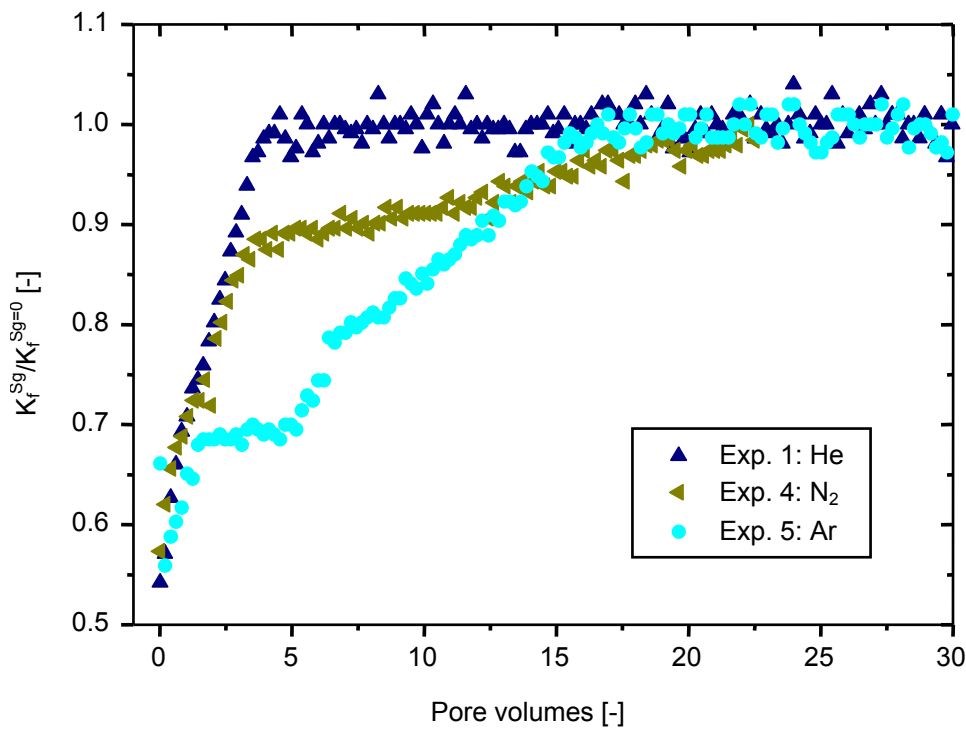


FIGURE 42: Normalized hydraulic conductivity versus saturated pore volumes for experiment 1 (dark blue triangles), experiment 4 (light green triangles) and experiment 5 (light blue dots) (flushing gases used to produce the low oxygen solution are given in the legend). The water flow velocity determined from the gravimetric measurements was 17 m/d for all three experiments.

For the experiments conducted with helium as flushing gas, complete water saturation was obtained after the oxygen gas phase was completely dissolved (Figure 42, experiment 1). As

expected, the transfer of helium into the gas bubbles was very small due to the low abundance of dissolved helium in the water phase. The gas volume was not increased distinctly through the influence of helium. The dissolution of the oxygen gas phase was therefore the dominant process.

The larger amount of nitrogen transferred into the gas bubbles during the dissolution of the oxygen gas phase resulted in a two-stage increase of the hydraulic conductivity curve (Figure 42, experiment 4). When the oxygen gas phase was completely dissolved, there was still a certain amount of gas in the column, which consisted of pure nitrogen. From the bromide tracer test a residual gas saturation of approximately 0.03 was calculated for experiment 4 when oxygen was entirely dissolved. This nitrogen gas phase dissolved much slower in the bypassing water than did the oxygen gas phase as a consequence of the much smaller concentration gradient and the lower solubility of nitrogen.

In the experiment where argon was used to produce the low oxygen solution (Figure 42, experiment 5), a two-stage rise of the hydraulic conductivity curve is observable during the dissolution experiment as well. Since the amount of argon transferred from the water into the gas phase was similar to the amount of oxygen leaving the gas bubble, the residual gas volume in the column decreased only a little during the entire removal of oxygen. The residual gas saturation in the column at the time the trapped oxygen gas phase was completely dissolved was much higher for the experiments performed with argon than in the experiments conducted with nitrogen as the flushing gas as can be seen by the fact that the second stage of the hydraulic conductivity curve rise starts at far lower values compared to the experiments with nitrogen. This residual argon gas phase dissolved slower in the bypassing water than the oxygen gas phase, but faster compared to the residual nitrogen gas phase in experiment 4 due to the higher solubility of argon in water compared to nitrogen.

In each experiment the trapped flushing gas phase was dissolved completely after a certain time. For helium after 3.5 pore volumes were exchanged, for argon after exchanging 17 pore volumes and for nitrogen after the exchange of 22.5 pore volumes. The entire dissolution of the gas phase can be explained by the higher pressure acting on the gas bubbles (hydrostatic and capillary pressure) resulting in a small concentration gradient. Because of the permanent supply of water that is saturated under atmospheric pressure and thus under-saturated with respect to the gas bubbles, a continuous mass transfer from the trapped gas bubbles into the water took place.

Since the sediment and experimental set up was the same in all ten experiments, a similar maximum hydraulic conductivity should be expected. The average maximum hydraulic

conductivity measured at complete water saturation was $1.93 \cdot 10^{-4}$ m/s with a standard deviation of 8.8 %. This deviation is a result of varying uncertainties during the pressure measurements of the single experiments caused by automatic temperature regulation of the constant temperature room and small gas bubbles trapped at the pressure sensor. Nevertheless, the hydraulic conductivity values give a good approximation of the true value. From the grain size distribution a nearly twofold greater value was calculated for the hydraulic conductivity for the sediment used in the column ($3.75 \cdot 10^{-4}$ m/s). It has to be noted though, that the set up specific parameters like the compactness of the packing and homogeneities of the mounting are not considered in the hydraulic conductivity determined empirically after Hazen from the grain size distribution. Moreover, the experimentally determined hydraulic conductivities characterize not only the built-in sand, but also the complete water filled system.

For the maximum effective porosity an averaged value of 0.373 ± 0.004 was determined for all ten experiments from the bromide tracer tests at complete water saturation. The total porosity determined from the sediment properties and the column dimensions was 0.376 ± 0.003 . The maximum effective and the total porosity are in good agreement, proving that almost the entire pore volume of the column is accessible for water and gas flow during the experiments.

A final issue of this work was addressing the influence of the trapped gas phase on the hydraulic conductivity. As stated in Chapter 2.4, the hydraulic conductivity will be reduced with the emplacement of a trapped gas phase into porous media. In the experiments the relative hydraulic conductivity $K_f^{(Sg=\max)}/K_f^{(Sg=0)}$ varied between 0.66 – 0.46 at a residual gas saturation of 7 – 9 % of the pore space.

The bromide tracer tests conducted primary to gain information on the saturation state of the column provided additional information on the longitudinal dispersivities of the column during the dissolution experiments. Except for experiments 1 and 2, where no distinct trend is apparent, the dispersivity curves exhibit a minimum at the beginning of the dissolution experiment, which is more pronounced for lower velocities. Similar observations in column experiments were made by Donaldson et al. (1997). They describe a decrease in their computed values of dispersivity with increasing volume of trapped gas. Donaldson et al. (1997) explain this decrease in dispersivities by the assumption that the presence of trapped gas reduces the effective pore size distribution in the column because the gas bubbles would occupy the larger pores. A more uniform distribution of pore sizes would create a more uniform distribution in pore scale velocity and a decreased dispersivity.

The maximum longitudinal dispersivities determined at complete water saturation before and after gas dissolution show a distinct dependency on the water flow velocity. The computed values of the second test series conducted at reduced water flow velocities differ by about 1 mm to the ones of the experiments 1 to 6 conducted at a velocity of 17 m/d, though the experimental conditions were similar. According to a classification of the longitudinal dispersion coefficient established by Sahimi (1995), the experiments of this work (with Peclet numbers between 10 and 20) should be described by a power-law regime ($5 < Pe < 300$). In this regime convection dominates dispersion, but the effect of diffusion cannot be neglected. According to Koch & Brady (1985) this regime is called boundary-layer dispersion.

6. Model Results

The applicability of the new developed kinetic multi-component model (variable volume model VVM), which takes into account a changing gas phase volume (Geistlinger et al., 2005), was tested by comparing the measured oxygen concentrations from the experiments with data of the model simulation. The VVM calculates the alteration of the gas volume with time during the dissolution of the trapped gas phase. The kinetic model also considers the behavior of a dissolved gas compound in the water phase partitioning into the gas phase. As mentioned in Chapter 3.1.2.2, the VVM accounts for a velocity-dependent mass transfer coefficient. The numerical solution of the VVM was compared to the semi-analytical solution developed by Cirpka & Kitanidis (2001) based on a local equilibrium approach.

6.1 Sensitivity Analysis

Since it is important to know the sensitive parameters of the VVM for inverse modeling, a sensitivity analysis was carried out prior to the numerical description of the experiments and the comparison to the local equilibrium approach. Therefore, the parameters to be considered varied within the error range of the following measured quantities considering experiment 3 as example: maximum residual gas saturation detected by gravimetric measurements $S_{g,grav}^{max} = 0.077 \pm 0.003$, longitudinal dispersivity $\alpha_l = 2.7 \text{ mm} \pm 0.2 \text{ mm}$, water flux $q_w = 6.25 \text{ m/d} \pm 0.08 \text{ m/d}$, maximum hydraulic conductivity $K_f^{max} = 1.84 \cdot 10^{-4} \text{ m/s} \pm 3.41 \cdot 10^{-6} \text{ m/s}$, van Genuchten parameter $n = 3.43 \pm 1$. These values together with the gas bubble radius $r_b = d_{50} = 0.3 \text{ mm}$ and a capillary pressure of zero are denoted as mean values in the following. First, the dissolved oxygen curve was calculated for the mean values with the VVM (thick black line in Figure 43). Afterwards, one parameter was changed at a time and the others held constant. In this manner, the sensitivity of the numerically calculated dissolved oxygen curve to the single parameters was tested (Figure 43). The variation of the single parameters used to calculate the resulting dissolved oxygen curve is indicated in the legend of Figure 43. Besides the dissolved oxygen curves where S_g , q_w and r_b were varied, all other curves overlay the dissolved oxygen curve calculated with the mean values. Consequently, only the maximum residual gas saturation, the water flux and the bubble radius are sensitive parameters within the corresponding error range. A dependency of the progression of the dissolved oxygen concentration curves on the water flux was also detected for the experimental elution curves and was assumed to be a result of the velocity dependency of the mass transfer (see Chapter 5.3). Whereas a variation of the gas saturation and the water flux causes only a parallel curve

shift, a variation of the gas bubble radius influences the curve slope. The smaller the gas bubble radius, the steeper is the curve slope. Therefore, the gas bubble radius is the only sensitive parameter regarding the mass transfer coefficient.

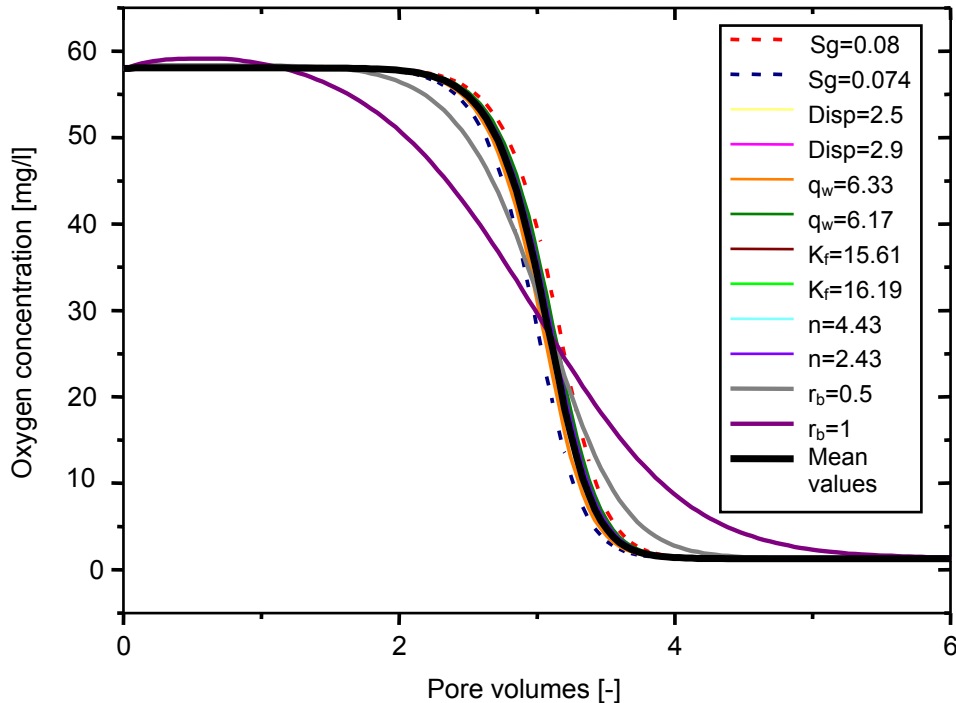


FIGURE 43: Sensitivity analysis for the oxygen concentration curve considering experiment 3 as example. The varied parameters are given in the legend. Besides the dissolved oxygen curves where S_g (dashed red and dark blue line), q_w (thin orange and green line) and r_b (grey and purple lines) was varied, all other curves overlay the dissolved oxygen curve calculated with the mean values (thick black line).

The gas bubble radius was fitted to the oxygen dissolution curve of experiment 3. The best fitting results were achieved for a bubble radius of 0.3 mm. This value corresponds to the medium grain diameter d_{50} . It is assumed that the d_{50} value yields this good agreement by chance and has no deeper physical reason. According to the assumption that the same sediment should lead to the same medium gas bubble radius, the gas bubble radius determined from experiment 3 was used for all ten experiments. The residual maximum gas saturation was approximated by the experimental data determined by gravimetric measurements and was assumed to be uniformly distributed. The water flux was also approximated by the experimental data. These free parameters were adjusted such that the model results agree best with the experimental data.

Regarding the parameters insensitive to the numerically calculated dissolved oxygen curve, the transport parameters like the longitudinal dispersivity were taken from the particular

experiment (determined by bromide tracer tests) (see Table 10). Moreover, an averaged maximum hydraulic conductivity value of $1.93 \cdot 10^{-4}$ m/s measured at complete water saturation and a van Genuchten parameter of 3.43 derived from the experimental $K_f(t)$ - and $S_g(t)$ - curve were used.

A set of fixed initial parameters used for the numerical simulation was also taken from the experiments and includes sediment parameters like the maximum effective porosity (determined by bromide tracer tests), geometrical data of the column like column length and diameter, and data concerning the thermodynamics like temperature and actual atmospheric pressure. Moreover, the physical and chemical parameters of the relevant gases like the dimensionless Henry's law constant and the diffusion coefficient as well as parameters concerning the water phase like the kinematic viscosity and the density of water are implemented in the model. The pressure distribution over the column was calculated from the pressure measured at the column outlet. Therefore the kinetic model displays the actual non-uniform pressure distribution in the column.

The same parameter set applied in the VVM was used for the local equilibrium model.

6.2 Comparison of Measured Data and Model Results

The experimental parameters, which were used as fitting parameters in the kinetic multi-component model, as well as the theoretical parameters derived by inverse modeling are summarized in Table 12.

TABLE 12: Experimental fitting parameters and theoretical parameters derived by inverse modeling.

Experiment	Flushing gas	$S_g^{\text{exp } 1}$ [%]	$S_g^{\text{num } 2}$ [%]	$q_w^{\text{exp } 3}$ [m/d]	$q_w^{\text{num } 2}$ [m/d]
1	He	8.2	8.5	6.29	6.19
2	He	7.5	8.7	6.37	6.30
3	N ₂	7.7	8.3	6.25	6.20
4	N ₂	8.3	8.8	6.56	6.47
5	Ar	8.5	8.2	6.34	6.40
6	Ar	7.8	8.1	6.15	6.10
7	N ₂	8.6	9.2	3.19	3.15
8	N ₂	7.6	8.5	3.19	3.15
9	N ₂	6.5	9.6	1.59	1.55
10	N ₂	8.9	9.6	1.63	1.55

¹ maximum residual gas saturation determined experimentally by gravimetric measurements

² determined by inverse modeling with the help of the VVM

³ experimentally determined water flux

In Figure 44 a) to e) the comparison between the kinetic theory, the local equilibrium theory and the experimental data is shown for one experiment per flushing solution and water flow velocity, respectively. The experimental results are displayed as data points, the simulated data as lines. In accordance to the experimental results, the same experiments were chosen for comparison as in the experimental discussion (see Chapter 5.3) regarding the flushing solution (experiments 1, 4, and 5). For the experiments at lower water flow velocities, experiments 7 and 10 were chosen.

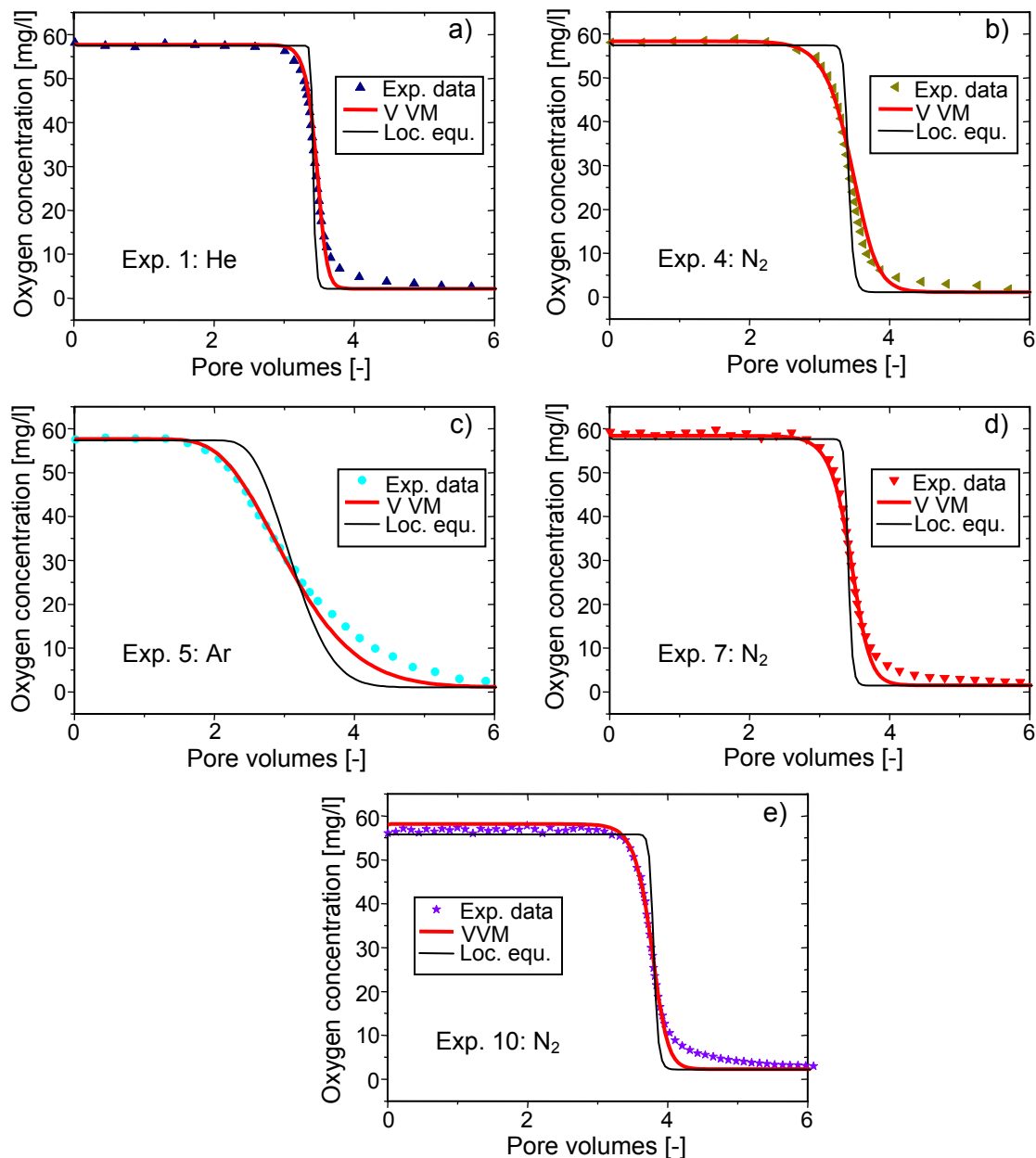


FIGURE 44: Comparison between experimental data (data points), kinetic theory (thick red line) and local equilibrium theory (thin black line). a) Experiment 1 (helium as flushing gas, water flow velocity: 17 m/d), b) experiment 4 (nitrogen as flushing gas, water flow velocity: 17 m/d), c) experiment 5 (argon as flushing gas, water flow velocity: 17 m/d), d) experiment 7 (nitrogen as flushing gas, water flow velocity: 9 m/d), e) experiment 10 (nitrogen as flushing gas, water flow velocity: 4 m/d).

For the experiments performed with different flushing gases to produce the low oxygen solution (helium, nitrogen and argon), the VVM results and the measured oxygen concentrations agree very well (Figure 44 a) to c)). The kinetic model reflects reasonably well the primary plateau like part, the decrease in the oxygen concentration and finally the transition to the low concentration part that equals the initial oxygen concentration in the flushing solution. However, there are small deviations in the long-tailing behaviour for all three experiments. The local equilibrium curves, calculated using the operator-splitting method proposed by Cirpka & Kitanidis (2001), also describe the experimental oxygen concentrations curves quite well, but show stronger deviations at the slope of the oxygen concentration curves compared to the kinetic multi-component model. For all three experiments performed with different flushing gases the local equilibrium curves show a steeper decline in the oxygen concentration.

Comparing the data of the VVM with the experimental data for the experiments with nitrogen as flushing gas conducted at lower velocities, again a good agreement can be seen (Figure 44 d) and e)). The model displays correctly the small offset between the curves of the experiments conducted at 9 and 4 m/d (see Chapter 5.3). The deviations at the lower tailing of the curves are more pronounced though. The local equilibrium curves again show a steeper decline in the oxygen concentration.

6.3 Discussion of the Model Results

The VVM is able to correctly describe both the dissolution of the oxygen gas phase in the water phase and the transfer of the already dissolved gases into the gas phase. This is an advantage over conventional one-component models, which can only consider the dissolution of the oxygen gas phase (Donaldson et al., 1997; Fry et al., 1995). The good agreement between the overall concentration profile predicted by the VVM and the measured data for all velocities supports the applied Sherwood number parameterization and the hypothesis that the dissolution process of a multi-component gas phase can be described by well-known physico-chemical parameters, like diffusion coefficient and dimensionless Henry's law constant.

The small deviation between the VVM and the experimental curves at the lower tailing of the curves are considered to be mainly due to diffusion-limited mass transfer. It is caused by a slower deliverance of oxygen from gas bubbles, which have a larger distance to the main flow paths. After entrapment of the gas bubbles in the column, the gas bubbles close to the main flow paths will be dissolved quickly and the dissolved oxygen is transported due to advection, whereas a small part of the gas bubbles, trapped at a greater distance from the flow paths due

to small inhomogeneities in the sediment will be dissolved more slowly and the oxygen is transported via diffusion. The model does not consider these gas bubbles since it assumes a homogeneous distribution of gas bubbles and flow through the column. Altogether this oxygen, which is dissolved more slowly, contributes to a small percentage to the total oxygen mass trapped in the column.

Moreover, a memory effect of the optode, which was also observed in the oxygen calibration curves (Appendix 5.2), could to a smaller proportion contribute to the delay as well. This memory effect is caused by diffusion of oxygen into the polymer of the flow through cell during flow with high oxygen concentrations. After the oxygen gas in the column is completely dissolved and low oxygen concentrations are reached in the water phase, the oxygen that was stored in the polymer is slowly diffusing into the water, leading to a slightly higher oxygen concentration than calculated by the model.

The average maximum residual gas saturation for all ten experiments determined by inverse modeling is 0.088 with a standard deviation of 6.3 %. This value lies in the range of the average maximum residual gas saturation of 0.08 determined experimentally by gravimetric measurements. Regarding the single experiments, the gas saturations determined by inverse modeling are slightly higher than the gas saturations determined experimentally by gravimetric measurements (Table 12). As mentioned before, the theoretical gas saturations are determined by fitting the model curve to the experimental data. The kinetic model considers the gas bubble radius to be constant over the whole column. In fact, the gas bubbles in the column will have a slightly variable size and some of the gas bubbles will have a greater radius than the radius used as fitting parameter in the model. Thereby, the dissolution of the gas phase will be slightly slower at the same experimental gas saturation due to the smaller gas-water interfacial area (see Chapter 2.1). Consequently, fitting the model to the experimental data leads to a higher theoretical gas saturation. Nevertheless, the theoretically determined gas saturations are in good coincidence with the experimentally determined ones. Therefore, the approximations made by the kinetic model regarding the bubble radius can be considered to be appropriate.

Concerning the local equilibrium approach it has to be considered that this approach is only valid for the cases where equilibrium is reached between the gas and water phase, which means at very slow groundwater flow conditions together with high concentration gradients (fast mass transfer) (see Chapter 3.1.1). The Damkohler number Da , which represents the ratio of hydraulic residence time to the mass transfer reaction time (Geistlinger et al., 2005),

can be used to estimate the degree of non-equilibrium between the gas and water phase for the experiments conducted in this work:

$$Da = \frac{k \cdot L}{u_w} \quad (52)$$

(L [m]: characteristic length). According to Brusseau (1992), a value of Da greater than 10 indicates that equilibrium is close to being attained under homogeneous conditions (constant rate constant and velocity). At early stages of the dissolution experiment, the gas phase extends over the whole column. Consequently, the characteristic length is given by the column length. Corresponding Da-values lie between 10 and 20. Therefore, the local-equilibrium approach should be valid. This explains the good agreement of the local equilibrium curves and the experimental curves at the beginning of the dissolution experiment. As the dissolution front moves through the column, the characteristic length and thus Da decreases. Therefore, the local equilibrium model curves deviate significantly from the experimental data in the later stage of the dissolution experiment. Nevertheless, the local equilibrium approach describes the most important features of the dissolution process for a multi-component gas phase, for example the changing gas volume and the correct partial gas pressures. Therefore, it can be used as a first approximation for parameter estimation of multi-component gas phases.

6.4 Additional Model Calculations

The calibrated kinetic multi-component model can provide a deeper understanding of the dissolution process of oxygen within the column in the presence of the different flushing gases. It can be used to predict the spatial distribution of the physical quantities, which cannot be obtained by experimental data, for example the spatial distribution of the gas saturation within the column and the dissolution of a single gas bubble at a certain position in the column. In the following, the same data set based on the experimental data is used for model calculations for all three dissolved gases used in the experiments. The parameter set is given in Table 13. Moreover, for the model calculations a column configuration like in the experiments was simulated (vertical position of the column, water flow from bottom to top). With the help of the VVM, processes in the column can be discussed on the gas bubble level. In Figure 45 the numerically calculated gas saturation over the column length L after 0.1 days (exchange of 1.82 pore volumes) is shown for all three flushing gases in comparison. Regarding the dissolution of the oxygen gas bubbles and assuming a homogeneous distribution of the gas bubbles over the entire column, two dissolution fronts can be

distinguished, running from inlet ($L = 0$ m) to outlet ($L = 0.942$ m) of the column. These dissolution fronts separate the column into three regions.

TABLE 13: Parameter set for theoretical calculations with the kinetic model.

Parameter	Value
u_w^{\max} [m/d] ¹	17
p_{atm} [kPa] ²	1017
Max. hydraulic conductivity ³ [$\cdot 10^{-4}$ m/s]	1.93
Max. effective porosity ⁴ [-]	0.373
Max. longitudinal dispersivity ⁵ [mm]	2.7
S_g^{\max} ⁶ [%]	8.0

¹ average water flow velocity at complete water saturation (exp. 1-6)

² average atmospheric pressure (exp. 1-10)

³ average maximum hydraulic conductivity determined by pressure measurements at complete water saturation (exp. 1-10)

⁴ average maximum eff. porosity determined by bromide tracer tests (Exp. 1-10)

⁵ average maximum longitudinal dispersivity determined by bromide tracer tests (exp. 1-6)

⁶ average maximum residual gas saturation determined by gravimetric measurements

The first dissolution front at approximately 0.6 m marks the transition from the pure oxygen gas phase to oxygen depleted gas phase. In the region at the column outlet downstream of the first dissolution front, the gas phase contains only oxygen. It is notably, that the gas saturation at the column top exceeds the initial gas saturation of 0.08 (illustrated through the thin horizontal line) for all three flushing gases. This is a result of the pressure decrease within the vertical positioned column. The water flowing upward through the column dissolves oxygen at the lower part of the column. There is a permanent supply of water with a low dissolved oxygen content into the column inlet, consequently the dissolution of the oxygen gas bubbles will be fast at the bottom of the column. In the middle of the column the water is enriched with oxygen by the previous uptake and the dissolution process will slow down due to the decreased concentration gradient between water and gas phase. When the water – saturated with oxygen – reaches the upper part of the column, the pressure decreases and the water is oversaturated with respect to the pressure acting at the top of the column. Consequently, part of the dissolved oxygen degases leading to an increase in the gas saturation, exceeding the initial value. The second dissolution front at $L = 0.1$ m denotes the entire dissolution of the gas phase, meaning there is no gas phase present in the column upstream of the second dissolution front, neither oxygen nor flushing gas. In the region between the two fronts, a gas phase still exists, containing nearly no oxygen, but mainly flushing gas, which partitioned from the water into the gas phase.

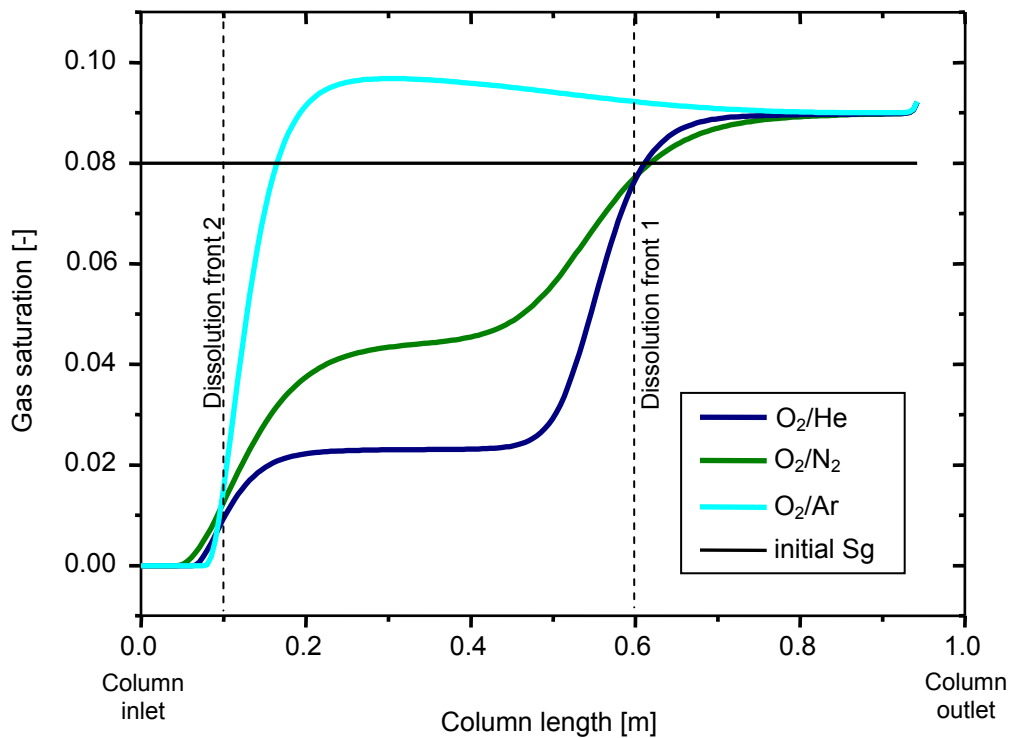


FIGURE 45: Gas saturation within the column at time $t = 0.1$ days (exchange of 1.82 pore volumes) predicted by the VVM for different flushing gases. The initial gas saturation of 0.08 is illustrated through the thin horizontal line.

In agreement with the experimental results, the three numerically determined gas saturation curves exhibit a different influence of the already dissolved gases (helium, nitrogen, argon) on the gas dissolution within the column (Figure 45). Whereas the gas saturation is decreasing for helium and nitrogen due to the lower transfer of the flushing gases into the gas phase compared to the dissolution of oxygen, in the case where argon is used as flushing gas the transfer of argon into the gas phase slightly exceeds the dissolution of oxygen, therefore the gas saturation increases in the region between the two dissolution fronts.

Figure 46 shows the gas saturation over the column length after 0.2 days (exchange of 3.64 pore volumes) for all three flushing gases. At this time the oxygen gas phase can be considered to be nearly completely dissolved by comparison to the experiments of test series 1 conducted at similar flow velocities (Figure 41, Chapter 5.3). Consequently, the gas phase remaining in the column after complete oxygen depletion consists exclusively of flushing gas. In the case where helium and nitrogen are used as dissolved gas, the gas saturation falls below the initial gas saturation, whereas in the case where argon was used as dissolved gas a significant enhancement of the gas saturation can be observed. The experimental hydraulic conductivity data (Figure 23, Chapter 5.1.1) indicated that in the

experiments with helium as flushing gas complete water saturation was reached at entire dissolution of the oxygen gas. The model data in Figure 46 in contrast shows that there is still a certain amount of helium gas in the upper part of the column after complete dissolution of the oxygen gas. This can be explained by the error range of the experimental hydraulic conductivity data. It is assumed that the small residual amount of helium gas in the column falls into this error range and could not be detected experimentally.

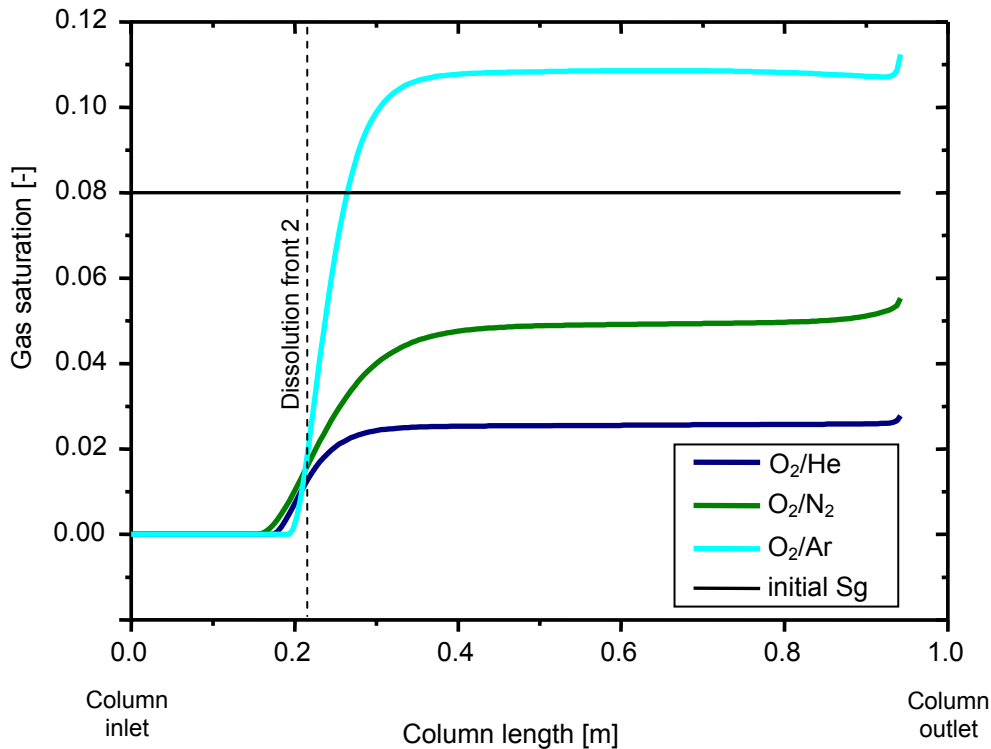


FIGURE 46: Gas saturation within the column at time $t = 0.2$ days (exchange of 3.64 pore volumes) predicted by the VVM for different flushing gases. The initial gas saturation of 0.08 is illustrated through the thin horizontal line.

Finally the dissolution of a gas bubble near the column inlet ($L = 0.1$ m) calculated from the VVM is shown in Figure 47 for all three two-component gas phases. Regarding a single gas bubble, the same dissolution behavior as reflected in the dissolution of the entire gas phase over the column can be observed. An oxygen gas bubble dissolving in a flushing solution containing helium shows a first steep decrease in the bubble radius from 0.3 to 0.2 mm due to the approximately four times greater transfer of oxygen into the water phase. Though helium is transferred faster to the gas bubble than oxygen is dissolved, the relative contribution of helium to the gas composition remains much lower compared to oxygen due to its lower abundance in the water phase. Nevertheless, the partial pressure of oxygen in the gaseous

phase changes when helium is transferred into the gas bubble leading to the following much slower decrease in the bubble radius as well as the slow dissolution of the much less soluble helium in the water passing by. After 0.125 days (exchange of 2.27 pore volumes) the gas bubble is completely dissolved.

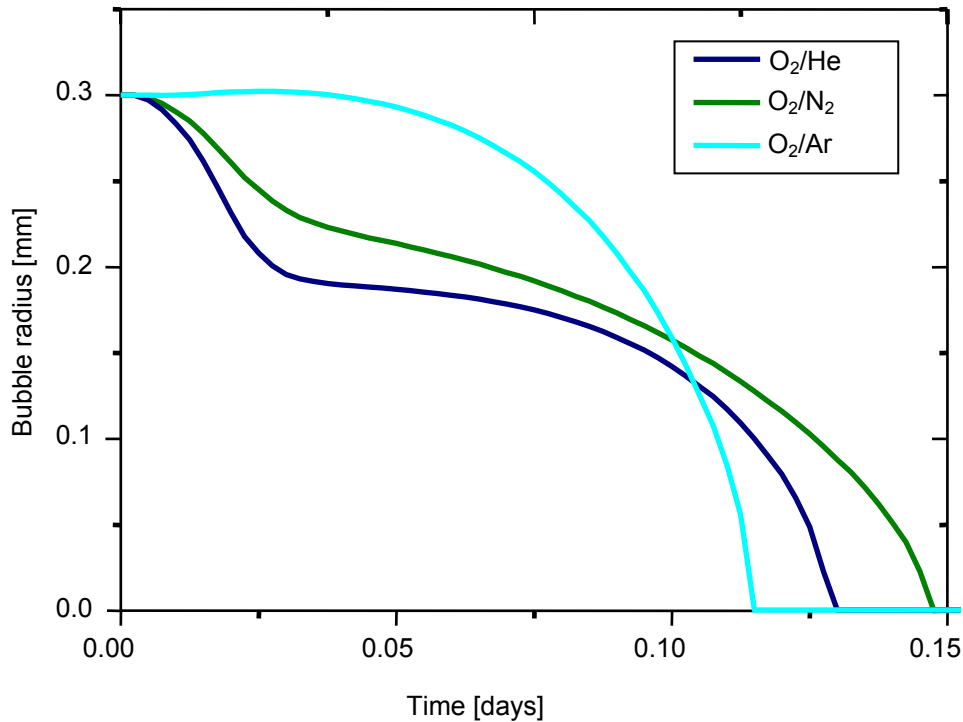


FIGURE 47: Dissolution of a gas bubble near the column inlet ($L = 0.1$ m) predicted by the VVM: Bubble radius versus time for three different two-component gas phases.

When nitrogen is used to produce the oxygen free flushing solution, the gas bubble shows a less steep first decrease in the bubble radius as with helium as flushing gas caused by the faster transfer of nitrogen into the gas bubble compared to helium. However, the transfer of oxygen into the water phase is still about two times faster than the partitioning of nitrogen into the gas bubble, leading to a decrease of the gas bubble radius from 0.3 to approximately 0.22 mm. The following dissolution of nitrogen in the water phase is slower compared to helium in spite of its larger solubility due to the larger amount of nitrogen that partitioned into the gas bubble during the dissolution of the oxygen. After 0.15 days (exchange of 2.73 pore volumes) the bubble is completely dissolved.

The dissolution of an oxygen gas bubble in an argon-saturated solution in contrast shows a different progression. Since argon has a higher diffusion coefficient in water and is available in somewhat higher quantity than oxygen, the number of argon moles transferring from the

water into the gas phase is slightly greater than the number of oxygen moles leaving the gas bubble. Consequently, the bubble radius is slightly increasing. After the oxygen is completely dissolved in the water phase, the bubble radius decreases until after approximately 0.11 days (exchange of 2 pore volumes) the bubble is dissolved. The argon gas is shown to dissolve faster in the water phase compared to helium and nitrogen because of its higher solubility in water.

7. Summary and Conclusions

The most important phenomena of the behaviour of oxygen in the aquifer, particularly the interphase mass transfer between a trapped oxygen gas phase and a mobile water phase containing varying dissolved gases have been addressed both experimentally and theoretically in this work.

Experimentally, a novel column design was created to conduct laboratory column experiments under near aquifer conditions. A significant achievement was a dynamical compression of the sediment inside the column resulting in an artificial application of a sediment overburden of about 11 m (dry sediment). In this manner, a stable grain structure was achieved avoiding the formation of preferential flow paths. As fixed boundary conditions, a constant water flow was established at the column entrance and a fixed hydrostatic pressure of approximately 7 kPa was applied at the column exit in order to prevent gas accumulation at the column outlet and simulate a certain depth in a saturated aquifer. The performance of the experiments in a constant temperature room at 10 °C quite closely reflected the general temperature conditions in natural aquifers.

Altogether, ten dissolution experiments were performed. Thereby, a direct gas injection of pure oxygen gas was performed to investigate the dissolution of a trapped oxygen gas phase. In the first test series, the different effects of various dissolved gases (helium, nitrogen and argon) in the mobile water phase on the oxygen dissolution process were monitored at a water flow velocity of 17 m/d. In the second test series, experiments were conducted with only nitrogen as the flushing gas at water flow velocities of 9 and 4 m/d. The saturation state of the column was determined by three independent methods: By gravimetric measurements, by consecutive bromide tracer tests, and by hydraulic conductivity measurements.

An average maximum residual gas saturation of 0.08 with a standard deviation of 8.7 % was determined for all ten experiments. No dependency of the achievable maximum gas saturation from the water and gas flow rate applied was observed in the experiments. The residual gas saturation values determined by the gravimetric measurements showed less variation and clearly smaller standard deviations compared to the values calculated from bromide tracer tests. The dissolution of the trapped oxygen gas phase lasted until approximately 3.5 to 4 pore volumes were exchanged for all experiments regardless of the flow velocity. Differences arose mainly from the influence of different dissolved gases in the water phase. The maximum obtainable oxygen concentrations in the outflow had a mean of 58.3 mg/l with a standard deviation of 2.2 % for all ten experiments.

The different dissolved gases (helium, nitrogen and argon) used in the experiments had a different effect on the dissolution process of the trapped oxygen gas phase due to their temperature-dependent diffusion coefficient in water and their concentration, and thus the total quantity in the water phase. The concentration of the dissolved gases depended on the initial conditions of the experiments. The flushing solutions were saturated with different gases and due to their solubility in water, the concentration of the gases and therefore the total amount of the dissolved gas in water varied. The higher the initial amount of the gas in the water, the greater was the influence on the dissolution of the trapped oxygen gas phase. Argon had the strongest effect on the dissolution of the trapped oxygen gas phase of all three flushing gases due to its higher abundance in the water phase compared to nitrogen and helium.

In all experiments the trapped oxygen gas phase dissolved completely. However, from the hydraulic conductivity measurements as well as from the gas saturation data calculated from the bromide tracer test it could be noted that there was still a certain amount of gas in the column after the complete dissolution of the trapped oxygen gas phase for the experiments performed with nitrogen and argon as flushing gases. This residual gas phase consisted of the flushing gas that was transferred from the water phase during the dissolution of the oxygen gas phase. This gas phase dissolved likewise completely, but the dissolution of this gas phase took longer compared to the dissolution of the oxygen gas phase since the concentration gradient was much lower. The trapped flushing gas phase was dissolved completely after the exchange of 17 pore volumes for argon and after exchanging 22.5 pore volumes for nitrogen. A reduction of the hydraulic conductivity of 34 – 54 % compared to the hydraulic conductivity at complete water saturation was measured at a gas saturation of 7 – 9 % of the pore space. The average maximum hydraulic conductivity measured at complete water saturation was $1.93 \cdot 10^{-4}$ m/s with a standard deviation of 8.8 %.

From the bromide tracer tests conducted consecutively during the dissolution of the oxygen gas phase, an averaged value of 0.373 ± 0.004 was determined for the maximum effective porosity at complete water saturation for all ten experiments. Moreover, the bromide tracer tests provided additionally information on the longitudinal dispersivity of the column during the dissolution experiments. The dispersivity curves exhibited a minimum at the beginning of the dissolution experiment, which was more pronounced for lower velocities. This decrease is assumed to be a result of the presence of trapped gas bubbles narrowing the effective pore size distribution in the column by occupying the larger pores. A more uniform distribution of pore sizes results in a more uniform distribution in pore scale velocity and a decreased

dispersivity. Furthermore, the maximum longitudinal dispersivities determined at complete water saturation before and after gas dissolution showed a distinct velocity dependency. The computed values of the second test series conducted at reduced water flow velocities differed by about 1 mm to the ones of the experiments 1 to 6 conducted at a velocity of 17 m/d, though the experimental conditions were similar.

A newly developed kinetic multi-component model (variable volume model VVM) was used to describe the experiments and was validated through integral information. The VVM considers the behavior of a dissolved gas compound in the water phase partitioning into the gas phase as well as a velocity-dependent mass transfer coefficient. The numerical solution of the VVM was compared to a semi-analytical solution of a model based on a local equilibrium approach.

The VVM consistently reproduced the experimental oxygen concentration curves for the experiments performed with different dissolved gases as well as for the experiments conducted at different water flow velocities. The VVM correctly described both the dissolution of the oxygen gas phase in the water phase and the transfer of the already dissolved gases into the gas phase. The average maximum residual gas saturation for all ten experiments determined by inverse modeling was 0.088 with a standard deviation of 6.3 %.

The local equilibrium model showed good agreement with the experimental curves as well. However, the local equilibrium model curves showed stronger deviations at the slope of the oxygen concentration curves compared to the kinetic multi-component model. For all experiments performed with different flushing gases and at different water flow velocities the local equilibrium curves showed a steeper decline in the oxygen concentration. Nevertheless, the local equilibrium approach described the most important features of the dissolution process for a multi-component gas phase, for example the changing gas volume and the correct partial gas pressures, and can be used as a first approximation for parameter estimation of multi-component gas phases.

The calibrated VVM was used for further model calculations with a data set based on the experimental data to make predictions of the spatial distribution of the gas saturation within the column and the dissolution of a single gas bubble at a certain position in the column, and thereby provide a deeper understanding of the dissolution process of an trapped oxygen gas phase within the column in the presence of the different flushing gases.

Two dissolution fronts running from inlet to outlet of the column could be distinguished, separating the column into three regions. In the first region close to the column outflow a pure oxygen gas phase existed that exceeded the initial gas saturation in the column due to the

pressure decrease over the column. In the second region behind the first dissolution front a gas phase containing nearly no oxygen, but mainly flushing gas degassed from the aqueous solution was present. In the last region behind the second front towards the column inlet finally, there was no gas phase left in the column, neither oxygen nor flushing gas. Therefore, the second front denoted the complete dissolution of the gas phase. Regarding a single gas bubble, the same dissolution behavior as reflected in the dissolution of the complete gas phase over the column was observed.

8. Outlook

The outcomes attained in this work on a laboratory scale will be taken into account for the performance of a field experiment. Within the framework of a project funded by the Bundesministerium für Wirtschaft und Arbeit (BMWA), the development and application of a model-supported feedback control for modular in situ gas injection systems is accomplished for a test site in Leuna, Saxony-Anhalt, mainly contaminated with BTEX and MTBE. The aim of this project is to investigate if natural occurring bioremediation processes can be enhanced by a controlled direct oxygen injection so that a complete degradation of the contaminants takes place. Thereby, the often observed problems during direct gas injections like blocking of flow paths, incomplete coverage of the reactive zone, insufficient oxygen supply or degassing into the unsaturated zone shall be avoided by the implementation of an efficient control mechanism.

On the test site a direct oxygen injection will be carried out over a novel construction of injection wells with several injection screens. The injection wells will be installed by direct push technology. The installation by direct push technology avoids the loosening of the ground in the vicinity of the injection well as observed with conventional drilling methods. Moreover, it allows a flexible vertical and lateral adjustment to the hydraulic and geologic conditions on site and hence permitting a spatially orientated access of discrete sediment horizons. Sediment boundaries can be used as hydraulic barriers against vertical gas flow and to increase the lateral extension of the gas phase. By an accurate dimensioning of the injection wells, a deliverance of oxygen meeting the stoichiometric requirements for complete contaminant degradation may be achieved.

The oxygen delivery will be controlled by injection intensity and interval based on an automated reactive transport model simulation for the injected oxygen. Thereby, a feedback control shall be obtained by calibrating and upgrading the model in the course of the remediation through intensive monitoring, including the in situ online detection of the dissolved oxygen concentration (Figure 48). The model used to support the control of the oxygen injection will comprise transport processes (advection, diffusion, dispersion), geochemical reaction processes and consumption by biological processes as well as the dissolution process of the gas phase and the release of dissolved contaminants from the source. To properly describe the mass transfer between the different phases, the VVM tested in this work shall be implemented in the reactive transport model. Thereby, the gas saturation achieved after a direct oxygen injection has to be determined properly, since it is a sensitive

parameter in the VVM as proved in the sensitivity analysis performed in Chapter 6.1. The maximum gas saturation will thereby depend on the grain size distribution and heterogeneity of the sediment in the field and can be determined for instance by partitioning tracer tests using nonreactive and nonpolar gases like neon, krypton or sulphur hexafluoride (Vulava et al., 2002). The flow velocity proved to be a sensitive parameter as well, and can be determined by tests with conservative dissolved tracers as well as pump tests. With these tests also the longitudinal dispersivity and the maximum effective porosity can be determined. For the gas bubble radius, the medium grain diameter d_{50} , which can be determined by dry grain size distribution analyses, can be used as a first approximation.

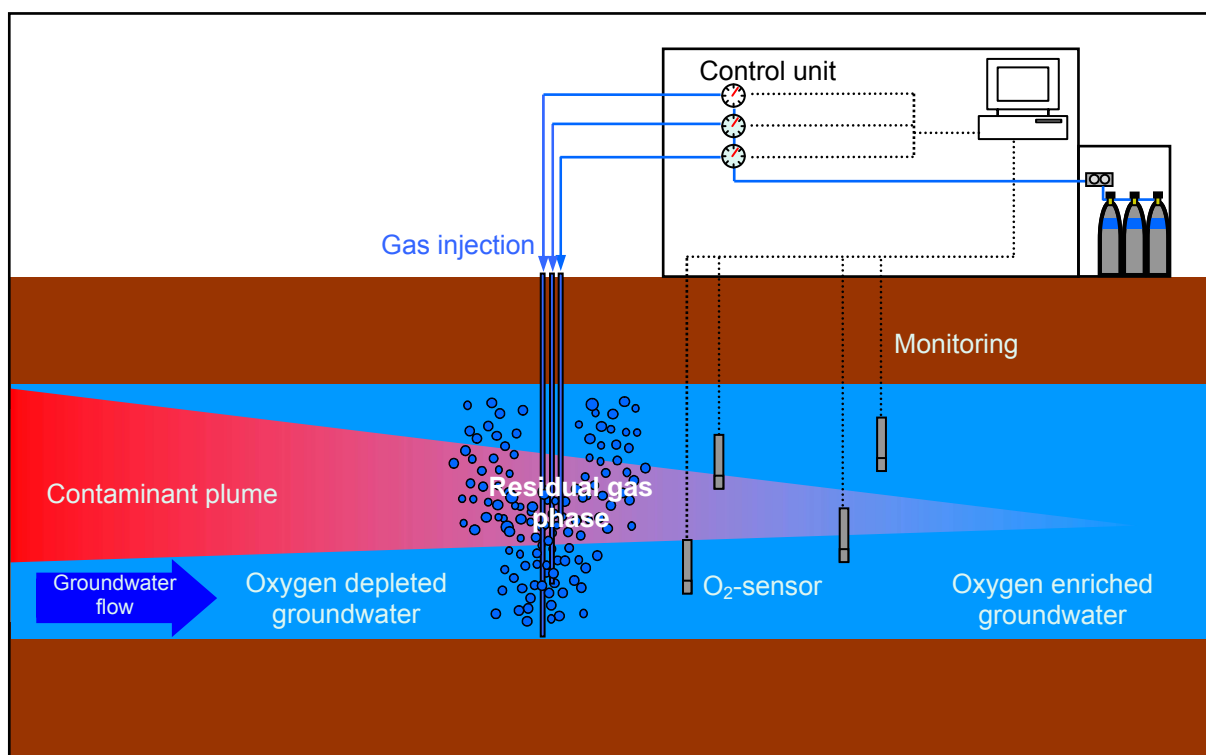


FIGURE 48: Principle of controlled direct gas injection (lateral view).

Further conclusions of the results of this work regarding the application and optimization of a direct oxygen injection in the field concern the presence of already dissolved gases in the bypassing groundwater. The experiments performed clearly showed that dissolved gases present in the water phase can have different effects on the dissolution of a trapped oxygen gas phase. Possible dissolved gaseous compounds in groundwater that might be considered are nitrogen, oxygen, methane and carbon dioxide some of which may be produced from microbial activity (Bae et al., 1995). The characteristic of the dissolution process depends strongly on the

temperature-dependent diffusion coefficient in water and the initial dissolved concentration of the gases involved. If the dissolved gases are present at high concentrations and possess a high diffusion coefficient, then the time needed for complete dissolution increases. Consequently, the quantity of relevant gases already dissolved in the water phase has to be determined at the test site as well as their physical and chemical parameters like the dimensionless Henry's law constant and the diffusion coefficient.

Another consideration of practical relevance gained from the results of this work is that impulse injection has to take into account the time for complete gas phase dissolution, because the dissolved gases are transferred into the gas phase during the dissolution of the oxygen gas phase and then dissolve much slower in the water phase due to a lower concentration gradient. Nevertheless, the experimental data indicates that capillary forces enhance the long-term dissolution process, and will therefore compete against hydraulic blocking. Anyhow, the new gas pulse should not be injected before almost entire dissolution of the gas phase, otherwise the oxygen partial pressure will be lowered for each subsequent injection, since it will be combined with present residual gas phases. To maintain a permanent delivery of oxygen in the reaction zone and to assure complete contaminant degradation, a thorough steering of the single injection wells has to be implemented.

The experimental results concerning the influence of a trapped oxygen gas phase on the hydraulic conductivity cannot be transferred to the field case directly. As a result of the high ratio of length to diameter of the column, the transport through the column can be considered as one-dimensional, whereas in the field the transport in the aquifer will be three-dimensional. In the column, the water is forced through the sediment containing the trapped gas phase due to a constant pumping rate, which results in large reductions in hydraulic conductivity. These large reductions will not be expected for the field experiments.

One important aspect regarding the direct oxygen injection that was not addressed by the laboratory experiments performed in this work is the geochemical impact, like oxygen consuming reactions and geochemical blocking by ferrihydrite precipitation. The injected oxygen finally dissolved in the water phase is not available for bioremediation only, but might be consumed through chemical oxygen reducing reactions like iron and manganese oxidation as well (Stumm & Morgan, 1996). In contaminated aquifers the conditions in the groundwater are often anoxic and therefore iron and manganese will be present as divalent ions (Fe^{2+} and Mn^{2+}). If oxygen is injected into the aquifer they are oxidized to the solid oxidation products of amorphous ferric oxyhydroxide $\text{FeOOH} \cdot \text{H}_2\text{O}$ (Sung & Morgan, 1980; Ralph & Stevenson, 1995), manganese dioxide MnO_2 and manganese oxyhydroxide MnOOH (Ellis et

al., 2000; Katsoyiannis & Zouboulis, 2004). In this case, the main oxygen consuming process is the rapid chemical oxidation of iron (Lovely, 2000), the abiotical oxidation of manganese with oxygen plays a minor role since it occurs very slowly (Diem & Stumm, 1984; Ellis et al., 2000; Katsoyiannis & Zouboulis, 2004). However, the manganese oxidation can be mediated biologically to some extent under aerobic conditions (Lovely, 2000). During the oxidation of Fe^{2+} and Mn^{2+} , minerals like iron hydroxides $\text{Fe}(\text{OH})_3$, ferrihydrates FeOOH and manganese dioxide MnO_2 are precipitated and can reduce the hydraulic conductivity. The impact of these additional reactions has to be considered in the reactive transport model used to predict the consumption of oxygen at a specific test site. Therefore, the chemical properties of the test site have to be determined.

Furthermore, the fate and transport of dissolved gases and contaminant compounds in the field are governed by small scale geological variations (Puls & Paul, 1997). The nature of heterogeneous porous media sometimes prevents full contact between microorganisms, contaminants, nutrients, and dissolved oxygen (Adams & Reddy, 2003). Hence, the implementation of a controlled direct oxygen injection calls for thorough investigation of the geological and hydraulic situation at the test site that control groundwater flow and solute transport.

References

- Adams, J. A.; Reddy, K. R. (1997): *The effect of grain size distribution on air sparging efficiency*. In: *In situ and on-site bioremediation*, Alleman, B. C.; Leeson, A., Eds.; Batelle Press: Columbus, Ohio; pp. 165-172.
- Adams, J. A.; Reddy, K. R. (1999): *Laboratory study of air sparging of TCE-Contaminated saturated soils and ground water*. *Ground Water Monit. Rem.*, 19 (3), 182-190.
- Adams, J. A.; Reddy, K. R. (2003): *Extent of benzene biodegradation in saturated soil column during air sparging*. *Ground Water Monit. Rem.*, 23 (3), 85-94.
- Aelion, C. M.; Kirtland, B. C. (2000): *Physical versus biological hydrocarbon removal during air sparging and soil vapor extraction*. *Environ. Sci. Technol.*, 34 (15), 3167-3173.
- Aeschbach-Hertig, W.; Peeters, F.; Beyerle, U.; Kipfer, R. (2000): *Palaeotemperature reconstruction from noble gases in ground water taking into account equilibration with entrapped air*. *Nature*, 405 (6790), 1040-1044.
- Atlas, R. M. (1991): *Bioremediation of fossil fuel contaminated soils*. In: *In Situ Bioreclamation. Applications and Investigations for Hydrocarbon and Contaminated Site Remediation*, Hinchey, R. E.; Olfenbuttel, R. F., Eds.; Butterworth-Heinemann: Stoneham; pp. 14-32.
- Bae, J.; Semprini, L.; McCarty, P. L. (1995): *Apparatus for Down-well Oxygen Transfer into Contaminated Aquifers*. *Journal of Environmental Engineering-Asce*, 121 (8), 565-570.
- Barenschee, E. R.; Bochem, P.; Helmling, O.; Weppen, P. (1991): *Effectiveness and Kinetics of Hydrogen Peroxide and Nitrate-Enhanced Biodegradation of Hydrocarbons*. In: *In Situ Bioreclamation. Applications and Investigations for Hydrocarbon and Contaminated Site Remediation*, Hinchey, R. E.; Olfenbuttel, R. F., Eds.; Butterworth-Heinemann: Stoneham; pp. 103-124.
- Barker, J. F.; Patrick, G. C.; Major, D. (1987): *Natural Attenuation of Aromatic Hydrocarbons in a Shallow Sand Aquifer*. *Ground Water Monit. Review*, 7, 64-71.

- Baveye, P.; Vandevivere, P.; Hoyle, B. L.; DeLeo, P. C.; de Lozada, D. S. (1998): *Environmental impact and mechanisms of the biological clogging of saturated soils and aquifer materials*. Critical Reviews in Environ. Sci. Technol., 28 (2), 123-191.
- Bear, J. (1972): *Dynamics of Fluids in Porous Media*. Dover Publications, Inc.: New York.
- Beek, B. (2001): *The Handbook of Environmental Chemistry Vol. 2 Part K: Biodegradation and Persistence*. Springer-Verlag: Berlin.
- Bird, R. B.; Stewart, W. E.; Lightfoot, E. N. (1960): *Transport phenomena*. John Wiley: New York.
- Borden, R. C.; Bedient, P. B. (1986): *Transport of Dissolved Hydrocarbons Influenced by Oxygen-Limited Biodegradation: 1. Theoretical Development*. Water Resour. Res., 22 (13), 1973-1982.
- Boudreau, B. P. (1997): *Diagenetic Models and their Implementation*. Springer-Verlag: Berlin.
- Brooks, M. C.; Wise, W. R.; Annable, M.D. (1999): *Fundamental changes in situ air sparging flow patterns*. Ground Water Monit. Rem., 19 (2), 105-113.
- Bruce, C. L.; Amerson, I. L.; Johnson, R. L.; Johnson, P. C. (2001): *Use of an SF₆-Based Diagnostic Tool for Assessing Air Distributions and Oxygen Transfer Rates during IAS Operation*. Bioremediation Journal, 5 (4), 337-347.
- Brusseau, M. L. (1992): *Rate-Limited Mass-Transfer and Transport of Organic Solutes in Porous-Media That Contain Immobile Immiscible Organic Liquid*. Water Resour. Res., 28 (1), 33-45.
- Busch, K. F.; Luckner, L.; Tiemer, K. (1993): *Lehrbuch der Hydrogeologie, Band 3: Geohydraulik*. Gebrüder Borntraeger: Berlin.
- Campbell, J. A.; Hanratty, T. J. (1982): *Mass Transfer between a Turbulent Fluid and a Solid Boundary: Linear Theory*. AIChE Journal, 28 (6), 988-993.
- Carsel, F. C.; Parrish, R. S. (1988): *Developing Joint Probability Distributions of Soil Water Retention Characteristics*. Water Resour. Res., 24, 755-769.

- Carter, S. R. (1998): *Oxygen Injection: A Promising Approach for MTBE Biodegradation*. Soil & Groundwater Cleanup; July.
- Chapelle, F. H. (2001): *Ground-Water Microbiology and Geochemistry*. 2nd ed., Wiley: New York.
- Chatzis, I.; Morrow, N. R.; Lim, H. T. (1983): *Magnitude and detailed structure of residual oil saturation*. SPEJ Soc. Pet. Eng. J., 23 (2), 311-326.
- Chiang, C. Y.; Salanitro, J. P.; Chai, E. Y.; Colthart, J. D.; Klein, C. L. (1989): *Aerobic Biodegradation of Benzene, Toluene, and Xylene in a Sandy Aquifer-Data Analysis and Computer Modeling*. Ground Water, 27 (6), 823-834.
- Christiansen, J. E. (1944): *Effects of entrapped air upon the permeability of soils*. Soil Sci., 58 (5), 355-365.
- Cirpka, O. A.; Kitanidis, P. K. (2001): *Transport of volatile compounds in porous media in the presence of a trapped gas phase*. J. Contam. Hydrol., 49 (3-4), 263-285.
- Clayton, W. S. (1998): *A field and laboratory investigation of air fingering during air sparging*. Ground Water Monit. Rem., 18 (3), 134-145.
- Crank, J. (1975): *The mathematics of diffusion*. Oxford University Press: New York.
- CRC-Handbook of Chemistry and Physics (1998), 78th ed., CRC Press: New York.
- Cunningham, J. A.; Rahme, H.; Hopkins, G. D.; Lebron, C.; Reinhard, M. (2001): *Enhanced in situ bioremediation of BTEX contaminated groundwater by combined injection of nitrate and sulfate*. Environ. Sci. Technol., 35 (8), 1663-1670.
- Cussler, E. L. (1997): *Diffusion Mass Transfer in Fluid Systems*. Cambridge University Press: Cambridge.
- Dankwerts, P. V. (1951): *Significance of liquid-film coefficients in gas absorption*. Ind. Eng. Chem., 43 (6), 1460-1467.
- Diem, D.; Stumm, W. (1984): *Is dissolved Mn^{2+} being oxidized by O_2 in absence of Mn-bacteria or surface catalysts?* Geochim. Cosmochim. Acta, 48 (7), 1571-1573.

-
- Donaldson, J. H.; Istok, J. D.; Humphrey, M. D.; O'Reilly, K. T.; Hawelka, C. A.; Mohr, D. H. (1997): *Development and testing of a kinetic model for oxygen transport in porous media in the presence of trapped gas*. *Ground Water*, 35 (2), 270-279.
- Dullien, F. A. L. (1992): *Porous Media, Fluid Transport and Pore Structure*. Academic Press: San Diego.
- Elder, C. R.; Benson, C. H. (1999): *Air channel formation, size, spacing, and tortuosity during air sparging*. *Ground Water Monit. Rem.*, 19 (3), 171-181.
- Ellis, D.; Bouchard, C.; Lantagne, G. (2000): *Removal of iron and manganese from groundwater by oxidation and microfiltration*. *Desalination*, 130 (3), 255-264.
- Faybishenko, B. A. (1995): *Hydraulic behavior of quasi-saturated soils in the presence of entrapped air: Laboratory experiments*. *Water Resour. Res.*, 31 (10), 2421-2435.
- Fetter, C.W. (1993): *Contaminant Hydrogeology*. Prentice-Hall, Inc.: Upper Saddle River, New Jersey.
- Fields, K.; Gibbs, J.; Condit, W. (2002): *Air Sparging: A Project Manager's Guide*. Batelle Press: Columbus, Ohio.
- Finneran, K. T.; Lovley, D. R. (2001): *Anaerobic degradation of methyl tert-butyl ether (MTBE) and tert-butyl alcohol (TBA)*. *Environ. Sci. Technol.*, 35 (9), 1785-1790.
- Fritsche, W. (1990): *Mikrobiologie*. Fischer Verlag: Jena.
- Fry, V. A.; Istok, J. D.; O'Reilly, K. T. (1996): *Effect of trapped gas on dissolved oxygen transport - Implications for in situ bioremediation*. *Ground Water*, 34 (2), 200-210.
- Fry, V. A.; Istok, J. D.; Semprini, L.; O'Reilly, K. T.; Buscheck, T. E. (1995): *Retardation of dissolved oxygen due a trapped gas phase in porous media*. *Ground Water*, 33 (3), 391-398.
- Fry, V. A.; Selker, J. S.; Gorelick, S. M. (1997): *Experimental investigations for trapping oxygen gas in saturated porous media for in situ bioremediation*. *Water Resour. Res.*, 33 (12), 2687-2696.

Geistlinger H.; Beckmann, A.; Lazik, D. (2005): *Mass Transfer between a Multi-Component trapped Gas Phase and a mobile Water Phase: Experiment and Theory*. Water Resour. Res., in press.

Geistlinger, H.; Lazik, D.; Beckmann, A., Eisermann, D.; Krauss, G.; Mayer, U. (2003): *Experimental and theoretical investigations of oxygen phase transfer: Reactive transport modeling of an in situ oxygen bubble wall*. Proc. GeoProc 2002, March 4-7, Bremen, Germany, VCH-Wiley publication, 19-36.

Gulliver, J. S. (1990): *Introduction to Air-Water Mass Transfer*. In: *Air-Water Mass Transfer*, Wilhelms, S. C.; Gulliver, J. S., Eds.; American Society of Civil Engineers: New York.

Gupta, S. K.; Lau, L. S.; Moravcik, P. S. (1994): *Ground-Water Tracing with Injected Helium*. Ground Water, 32 (1), 96-102.

Haggerty, R.; Gorelick, S. M. (1995): *Multiple-rate mass transfer for modeling diffusion and surface reactions in media with pore-scale heterogeneity*. Water Resour. Res., 31 (10), 2383-2400.

Hayduk, W.; Laudie, H. (1974): *Prediction of diffusion coefficients for non-electrolytes in dilute aqueous solutions*. AIChE J., 20, 611-615.

Hecht, H.; Kölling, A. (2001): *A low-cost optode-array measuring system based on 1 mm plastic optical fibers - new technique for in situ detection and quantification of pyrite weathering processes*. Sensors and Actuators B-Chemical, 81 (1), 76-82.

Hoepfel, R. E.; Hinchey, R. E.; Arthur, M. F. (1991): *Bioventing of soils contaminated with petroleum hydrocarbons*. J. Indust. Microbio., 8, 141-146.

Holocher, J.; Peeters, F.; Aeschbach-Hertig, W.; Kinzelbach, W.; Kipfer, R. (2003): *Kinetic Model of Gas Bubble Dissolution in Groundwater and Its Implication for the Dissolved Gas Composition*. Environ. Sci. Technol., 37 (7), 1337-1343.

Holst, G.; Glud, R. N.; Kuhl, M.; Klimant, I. (1997): *A microoptode array for fine-scale measurement of oxygen distribution*. Sensors and Actuators B-Chemical, 38 (1-3), 122-129.

Huling, S. G.; Bledsoe, B. E.; White, M. V. (1991): *The feasibility of utilizing hydrogen peroxide as a source of oxygen in bioremediation*. In: *In Situ Bioreclamation. Applications*

and Investigations for Hydrocarbon and Contaminated Site Remediation, Hinchee, R. E.; Olfenbittel, R. F., Eds.; Butterworth-Heinemann: Stoneham; pp. 83-102.

Jähne, B.; Heinz, G.; Dietrich, W. (1987): *Measurement of the diffusion coefficients of sparingly soluble gases in water*. J. Geophys. Res., 92 (C10), 10767-10776.

Ji, W.; Dahmani, A.; Ahlfeld, D.P.; Lin, J.D.; Hill, E. (1993): *Laboratory Study of Air Sparging: Air Flow Visualization*. Ground Water Monit. Rem., 13 (4), 115-126.

Johnson, P. C. (1998): *Assessment of the contributions of volatilization and biodegradation to in situ air sparging performance*. Environ. Sci. Technol., 32 (2), 276-281.

Johnson, R. L.; Johnson, P. C.; McWhorter, D. B.; Hinchee, R. E.; Goodman, I. (1993): *An overview of in situ air sparging*. Ground Water Monit. Rem., 13 (4), 127-135.

Katsoyiannis, I. A.; Zouboulis, A. I. (2004): *Biological treatment of Mn(II) and Fe(II) containing groundwater: kinetic considerations and product characterization*. Water Res., 38 (7), 1922-1932.

Kim, H.; Rao, P. S. C.; Annable, M. D. (1997): *Determination of effective air-water interfacial area in partially saturated porous media using surfactant adsorption*. Water Resour. Res., 33 (12), 2705-2711.

Koch, D. L.; Brady, J. F. (1985): *Dispersion in fixed-beds*. J. Fluid Mech., 154, 399-427.

Koenigsberg, S.; Sandefur, C. (2001): *Application of Oxygen Release Compound: A Six-Year Review*. In: *Proceedings of the Sixth International In Situ and On-Site Bioremediation Symposium (San Diego, June 4-7, 2001)*, Magar, V. S.; Leeson, A., Eds.; Vol. 6 (10), Battelle: Columbus, Ohio.

Lazik, D. (1998): *Modified set-up for column experiments to improve the comparability of water-rock interaction data: Column cap and hydraulic control system*. In: *Water-rock interaction: proceedings of the 9th International Symposium on Water-rock interaction*, Arehart, G. B., Ed.; Balkema: Rotterdam; pp. 847-850.

Lazik, D.; Geistlinger, H.; Krauss, G.; Beckmann, A., Schirmer, M. (2002): *Untersuchungen zum Strömungsverhalten und zur Lösungskinetik von Gasen im Mehrphasensystem Aquifer*. Grundwasser, 3 (7), 146-155.

- Lee, M. D.; Raymond, R. L. (1991): *Case History of the Application of Hydrogen Peroxide as an Oxygen Source for In Situ Bioreclamation*. In: *In Situ Bioreclamation. Applications and Investigations for Hydrocarbon and Contaminated Site Remediation*, Hinchee, R. E.; Olfenbittel, R. F., Eds.; Butterworth-Heinemann: Stoneham; pp. 429-436.
- Levenspiel, O. (1972): *Chemical reaction engineering*. John Wiley: New York.
- Levich, V. (1962): *Physicochemical hydrodynamics*. Prentice Hall: Englewood Cliffs, New Jersey.
- Lovely, D. R. (2000): *Environmental microbe-metal interactions*. ASM Press: Washington, D.C..
- Luckner, L. (2001): *Wirkung von Gasen auf den reaktiven Stofftransport im Mehrphasensystem Untergrund*. *Grundwasser*, 6 (4), 155-162.
- Luckner, L.; Ehbrecht, H.; Rößner, U. (2001): *In-situ-Reinigung kontaminierter anoxischer Grundwasserleiter durch sauerstoffangereichertes Infiltrationswasser*. *Wasser Abwasser*, 142 (11), 774-781.
- Luckner, L.; Schestakow, W. M. (1991): *Migration Processes in the Soil and Groundwater Zone*. Lewis Publisher: Michigan.
- Luckner, L.; van Genuchten, M. T.; Nielsen, D. R. (1989): *A Consistent Set of Parametric Models for the Two-Phase Flow of Immiscible Fluids in the Subsurface*. *Water Resour. Res.*, 25, 2187-2193.
- MacDonald, J. A. (2000): *Evaluating natural attenuation for groundwater cleanup*. *Environ. Sci. Technol.*, 34 (15), 346A-353A.
- MacEwen, S. J.; Fadullon, F.; Hayes, D. (2001): *Evaluation of Aerobic and Anaerobic Degradation of Pentachlorophenol in Groundwater*. In: *Proceedings of the Sixth International In Situ and On-Site Bioremediation Symposium (San Diego, June 4-7, 2001)*, Magar, V. S.; Leeson, A., Eds.; Vol. 6 (3), Battelle: Columbus, Ohio.
- Madigan, M. T.; Martinko, J. M.; Parker, J. (2000): *Brock Biology of Microorganisms*. 9th ed., Prentice-Hall, Inc.: Upper Saddle River, New Jersey.

- Miller, C. T.; Poirier-McNeill, M. M.; Mayer, A. S. (1990): *Dissolution of Trapped Nonaqueous Phase Liquids: Mass Transfer Characteristics*. Water Resour. Res., 26 (11), 2783-2796.
- Morrow, N.R.; Songkran, B. (1981): *Effect of viscous and buoyancy forces on nonwetting phase trapping in porous media*. In: *Surface Phenomena in Enhanced Oil Recovery*, Shah, D.O., ed.; Plenum: New York, pp. 387-411.
- National Research Council (1993): *In Situ Bioremediation: When Does It Work?* National Academy Press: Washington, DC.
- Nedelchev, S. (2003): *Correction of the penetration theory applied for prediction of mass transfer coefficients in a high-pressure bubble column operated with gasoline and toluene*. J. Chem. Eng. Jpn., 36 (5), 630-633.
- Norris, R. D.; Hincbee, R. E.; Brown, R.; McCarty, P. L.; Semprini, L.; Wilson, J. T.; Kampbell, D. H.; Reinhard, M.; Bouwer, E. J.; Borden, R. C.; Vogel, T. M.; Thomas, J. M.; Ward, C. H. (1994): *Handbook of bioremediation*. Lewis Publishers: Boca Raton.
- Nyer, E. K.; Davis, J. S.; King, I. (2002) Oxygen revisited. Ground Water Monit. Rem., 22 (3), 44-49.
- Nyer, E. K.; Kidd, D. F.; Palmer, P. L.; Crossman, T. L.; Fam, S.; Johns II, F. J.; Boettcher, G.; Suthersan, S. S. (1996): *In situ treatment technology*. Lewis Publishers: Boca Raton.
- Ohsumi, T.; Horibe, Y. (1984): *Diffusivity of He and Ar in deep-sea sediments*. Earth Planet. Sci. Letters, 70 (1), 61-68.
- Pardieck, D. L.; Bouwer, E. J.; Stone, A. T. (1992): *Hydrogen peroxide use to increase oxidant capacity for in situ bioremediation of contaminated soils and aquifers*. J. Contam. Hydrol., 9 (3), 221-242.
- Peck, A. J. (1969): *Entrapment, stability and persistence of air bubbles in soil water*. Aust. J. Soil Res., 7, 79-90.
- Peterson, J. W.; Lepczyk, P. A.; Lake, K.L. (1999): *Effect of sediment size on area of influence during groundwater remediation by air sparging: A laboratory approach*. Environmental Geology, 38 (1), 1-6.

- Peterson, J. W.; Murray, K. S. (2003): *Grain-size heterogeneity and subsurface stratification in air sparging of dissolved-phase contamination: Laboratory experiments-field implications*. Environ. Eng. Geoscience, 9 (1), 71-82.
- Peterson, J. W.; Murray, K. S.; Tulu, Y. I.; Peuler, B. D.; Wilkens, D. A. (2001): *Airflow geometry in air sparging of fine-grained sands*. Hydrogeology Journal, 9 (2), 168-176.
- Powers, S. E.; Loureiro, L. M.; Abriola, L. M.; Weber, W. J. (1991): *Theoretical Study of the Significance of Nonequilibrium Dissolution of Nonaqueous Phase Liquids in Subsurface Systems*. Water Resour. Res., 27 (4), 463-477.
- Press, W. H.; Teukolsky, S. A.; Vetterling, W. T; Flannery, B. P. (1992): *Numerical Recipes in C*. 2nd ed., University Press: Cambridge.
- Prosen, B. J.; Korreck, W. M.; Armstrong, J. M. (1991): *Design and Preliminary Performance Results of a Full-Scale Bioremediation System Utilizing an On-Site Oxygen Generator System*. In: *In Situ Bioreclamation. Applications and Investigations for Hydrocarbon and Contaminated Site Remediation*, Hinchee, R. E.; Olfenbuttel, R. F., Eds.; Butterworth-Heinemann: Stoneham; pp. 523-528.
- Puls, R. W.; Paul, C. J. (1997): *Multi-layer sampling in conventional monitoring wells for improved estimation of vertical contaminant distributions and mass*. J. Cont. Hydrol., 25 (1-2), 85-111.
- Ralph, D. E.; Stevenson, J. M. (1995): *The role of bacteria in well clogging*. Water Res., 29 (1), 365-369.
- Reineke, W. (2001): *Aerobic and anaerobic biodegradation potentials of microorganisms*. In: *The Handbook of Environmental Chemistry Vol. 2 Part K: Biodegradation and Persistence*, Beek, B., Ed.; Springer-Verlag: Berlin; pp. 1-161.
- Roberts, P. V.; Hopkins, G. D.; Mackay, D. M.; Semprini, L. (1990): *A field evaluation of in-situ biodegradation of chlorinated ethenes: Part I, Methodology and field site characterization*. Ground Water, 28 (4), 591-604.
- Romkes, S. J. P.; Dautzenberg, F. M.; Van den Bleek, C. M.; Calis, H. P. A. (2003): *CFD modelling and experimental validation of particle-to-fluid mass and heat transfer in a packed bed at very low channel to particle diameter ratio*. Chem. Eng. Sci., 96 (1-3), 3-13.

- Sahimi, M. (1995): *Flow and Transport in Porous Media and Fractured Rock*. VCH Verlagsgesellschaft mbH: Weinheim.
- Schirmer, M. (2001): *Assessment and Implementation of In Situ Groundwater Remediation Approaches*. Habilitation, University of Tübingen.
- Schwarzenbach, R. P.; Gschwend, P. M.; Imboden, D. M. (2002): *Environmental Organic Chemistry*. 2nd ed., John Wiley & Sons Inc.: New York.
- Semprini, L.; Roberts, P. V.; Hopkins, G. D.; McCarty, P. L. (1990): *A field evaluation of in-situ biodegradation of chlorinated ethenes: Part 2, results of biostimulation and biotransformation experiments*. *Ground Water*, 28 (5), 715-727.
- Stumm, W.; Morgan, J. J. (1996): *Aquatic Chemistry*. 3rd ed., John Wiley & Sons, Inc.: New York.
- Sung, W.; Morgan, J. J. (1980): *Kinetics and Product of Ferrous Iron Oxygenation in Aqueous Systems*. *Environ. Sci. Technol.*, 14 (5), 561-568.
- Teutsch, G.; Gratwohl, P.; Schiedek, T. (1997): *Literaturstudie zum natürlichen Rückhalt/Abbau von Schadstoffen im Grundwasser*. Handbuch Altlasten und Grundwasserschadensfälle, 12, Zentraler Fachdienst Wasser-Boden-Abfall bei der Landesanstalt für Umweltschutz Baden-Württemberg.
- Thomas, J. M.; Ward, C. H. (1989): *In situ bioremediation of organic contaminants in the subsurface*. *Environ. Sci. Technol.*, 23 (7), 760-766.
- Treybal, R. E. (1980): *Mass-transfer operations*. 3rd ed., McGraw Hill: Boston, Massachusetts.
- Vulava, V. M.; Perry, E. B.; Romanek, C. S.; Seaman, J. C. (2002): *Dissolved gases as partitioning tracers for determination of hydrogeological parameters*. *Environ. Sci. Technol.*, 36 (2), 254-262.
- Wardlaw, N. C. (1982): *The effects of geometry, wettability, viscosity and interfacial tension on trapping in single pore-throat pairs*. *J. Can. Petrol. Tech.*, 21 (3), 21-27.
- Weber, L. (2000): *Labortechnische Untersuchung zum vertikalen Gastransport in Grundwasserleitern*, Diplomarbeit, TU Dresden.

Wilson, R. D.; Mackay, D. M. (2002): *Diffusive Oxygen Emitters for Enhancement of Aerobic In Situ Treatment*. Ground Water Monit. Rem., 22 (2), 88-98.

Wilson, R. D.; Mackay, D. M.; Cherry, J. A. (1997): *Arrays of unpumped wells for plume migration control by semi-passive in situ remediation*. Ground Water Monit. Rem., 17 (3), 185-193.

Zheng, C.; Bennett, G. D. (2002): *Applied Contaminant Transport Modeling*. 2nd ed., Wiley-Interscience: New York.

Acknowledgement

I would like to thank my advisor Prof. Dr. Helmut Geistlinger for his support and guidance during this work. To him as well as to Prof. Dr. Broder Merkel I owe thanks for the critical review of the thesis manuscript. Thanks are due to Dr. Detlef Lazik for his assistance during the experiments and his helpful suggestions.

Special thanks go to Prof. Dr. Kevin Biggar from the University of Alberta and Prof. Dr. Ulrich Mayer from the University of British Columbia for their support and the hospitality during my working stays in Canada.

Particularly I owe thanks to Prof. Dr. Mario Schirmer for his continuous support. Moreover, it is due to him, PD Dr. Marion Martienssen, Dr. Matthias Gerhardt and Mark Zittwitz that I got the opportunity to continue my studies on gas dissolution within the OXYWALL project and test the results of my thesis in the field.

Without the assistance and the many helpful advices from my colleagues at the Umweltforschungszentrum Halle this work would not have been possible. Special thanks go to Anke Bittkau, Norbert Betzl, Norbert Geisler and Deepak Jain.

Thanks to my Canadian cousins Cindy, Natalie and Jill Bruntjen for helping me at my struggle with the English language.

Finally, I would like to thank my family and my friends for always encouraging and motivating me. Without your assistance it would have been much more difficult.

Annika Beckmann

Appendix

Appendix 1: Henry's Law Constant

Appendix 2: Dry Grain Size Distribution Analyses

Appendix 2.1: Dry Grain Size Distribution Analysis 1

Appendix 2.2: Dry Grain Size Distribution Analysis 2

Appendix 3: Drawings of the Column Cap

Appendix 3.1: Drawing of the Column Cap, Sectional View (Front)

Appendix 3.2: Drawing of the Column Cap, Sectional View (Top, Cutting Plane Level 1)

Appendix 3.3: Drawing of the Column Cap, Sectional View (Top, Cutting Plane Level 2)

Appendix 4: Error Analysis for the Calculation of the Maximum Residual Gas Saturation

Appendix 5: Oxygen Measurements

Appendix 5.1: Determination of the Oxygen Concentration Using a Modified Stern-Volmer Equation (after FIBOX Instruction Manual, PreSens GmbH)

Appendix 5.2: Calibration of the Oxygen Sensor (Optode) (Exemplarily for Exp. 3)

Appendix 6: Calibration of the Pressure Transducers (Exemplarily for Exp. 3)

Appendix 7: Calibration of the Bromide Electrodes (Exemplarily for Exp. 3)

Appendix 8: Calibration of the Four-Channel Peristaltic Pump

Appendix 1: Henry's Law Constant

The Henry's law constant K_H is the gas to water partitioning coefficient. It relates the solubility of a gas i in water to the pressure of the gas i over the water according to Henry's law:

$$K_{H_i} = \frac{C_i}{p_i} \quad (A1)$$

K_{H_i} = Henry's law constant of the gas i [mol/l kPa]

C_i = Concentration of the gas i in water [mol/l]

p_i = partial pressure of the gas i [kPa]

In this work the dimensionless form of the Henry's law constant H is used predominantly. The dimensionless form is simply the ratio of the chemical concentration in gas to that in water:

$$H_i = \frac{C_{i,g}}{C_{i,w}} \quad (A2)$$

H_i = dimensionless Henry's law constant of the gas i [-]

$C_{i,g}$ = Concentration of the gas i in the gas phase [mg/l]

$C_{i,w}$ = Concentration of the gas i in water [mg/l]

The dimensionless form can be converted to the dimensional form using the equation below:

$$H_i = \frac{1}{K_{H_i} \cdot R_g \cdot T} \quad (A3)$$

R_g = universal gas constant [kPa l/mol K]

T = absolute temperature [K]

Appendix 2: Dry Grain Size Distribution Analyses

Appendix 2.1: Dry Grain Size Distribution Analysis 1

Date of testing: 2004-01-08

Sample No.: 1

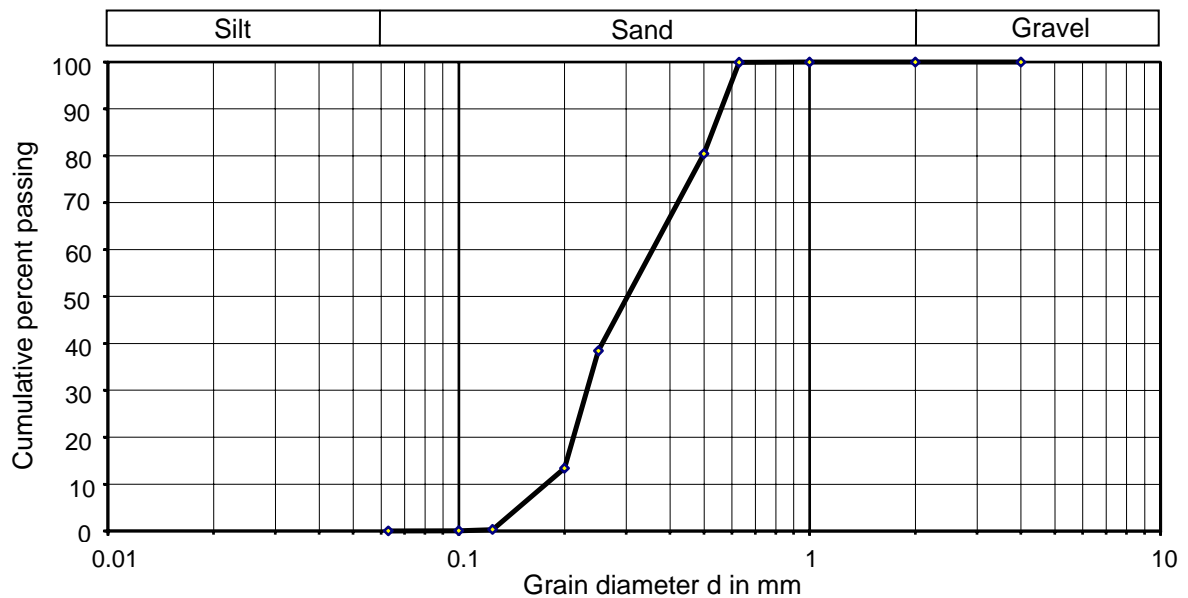
Weight of dry sample [g]: 570.76

Diameter [mm]	Weight retained [g]	Weight passing [g]	% passing	Cumulative % passing
4		0.01	0	100
2	0.01	0.03	0.01	100
1	0.03	0.17	0.03	99.99
0.63	0.17	111.53	19.54	99.96
0.5	111.53	239.87	42.03	80.42
0.25	239.87	142.73	25.01	38.39
0.2	142.73	74.65	13.08	13.38
0.125	74.65	1.37	0.24	0.3
0.1	1.37	0.22	0.04	0.06
0.063	0.22	0.14	0.02	0.02
Pan	0.14			

Total: 570.72 g

Loss: 0.04 g

Grain size distribution curve
Sample 1



$$d_{10} = 0.18$$

$$d_{50} = 0.30$$

$$d_{60} = 0.36$$

$$U = d_{60}/d_{10} = 2$$

$$K_f = C_H \cdot d_{10}^2 = 3.75 \cdot 10^{-4} \text{ m/s}$$

$$C_H = (0.7 + 0.03 \cdot T)/86.4 = 0.0116 \quad (\text{for an aquifer typical temperature of } 10 \text{ }^\circ\text{C})$$

Appendix 2.2: Dry Grain Size Distribution Analysis 2

Date of testing: 2004-01-08

Sample No.: 2

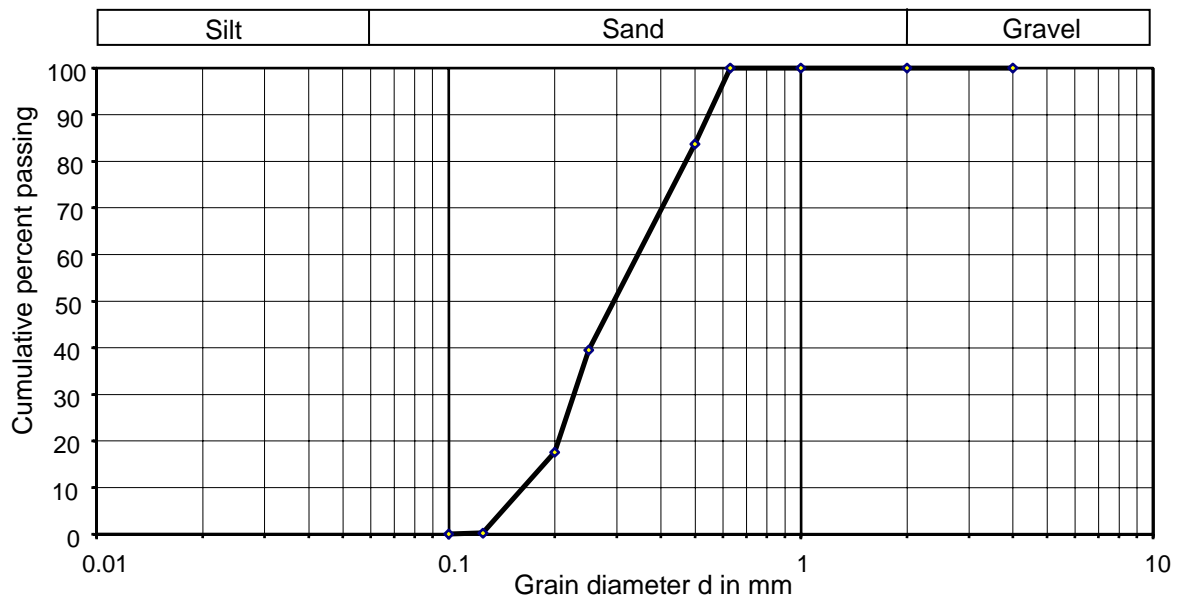
Weight of dry sample [g]: 266.83

Diameter [mm]	Weight retained [g]	Weight passing [g]	% passing	Cumulative % passing
4		0	0	100
2	0	0	0	100
1	0	0.04	0.01	99.99
0.63	0.04	43.44	16.29	99.98
0.5	43.44	117.83	44.17	83.69
0.25	117.83	58.47	21.92	39.52
0.2	58.47	46.25	17.34	17.60
0.125	46.25	0.54	0.20	0.26
0.1	0.54	0.09	0.03	0.06
0.063	0.09	0.08	0.03	0.03
Pan	0.08			

Total: 266.74 g

Loss: 0.09 g

Grain size distribution curve
Sample 2



$$d_{10} = 0.18$$

$$d_{50} = 0.29$$

$$d_{60} = 0.35$$

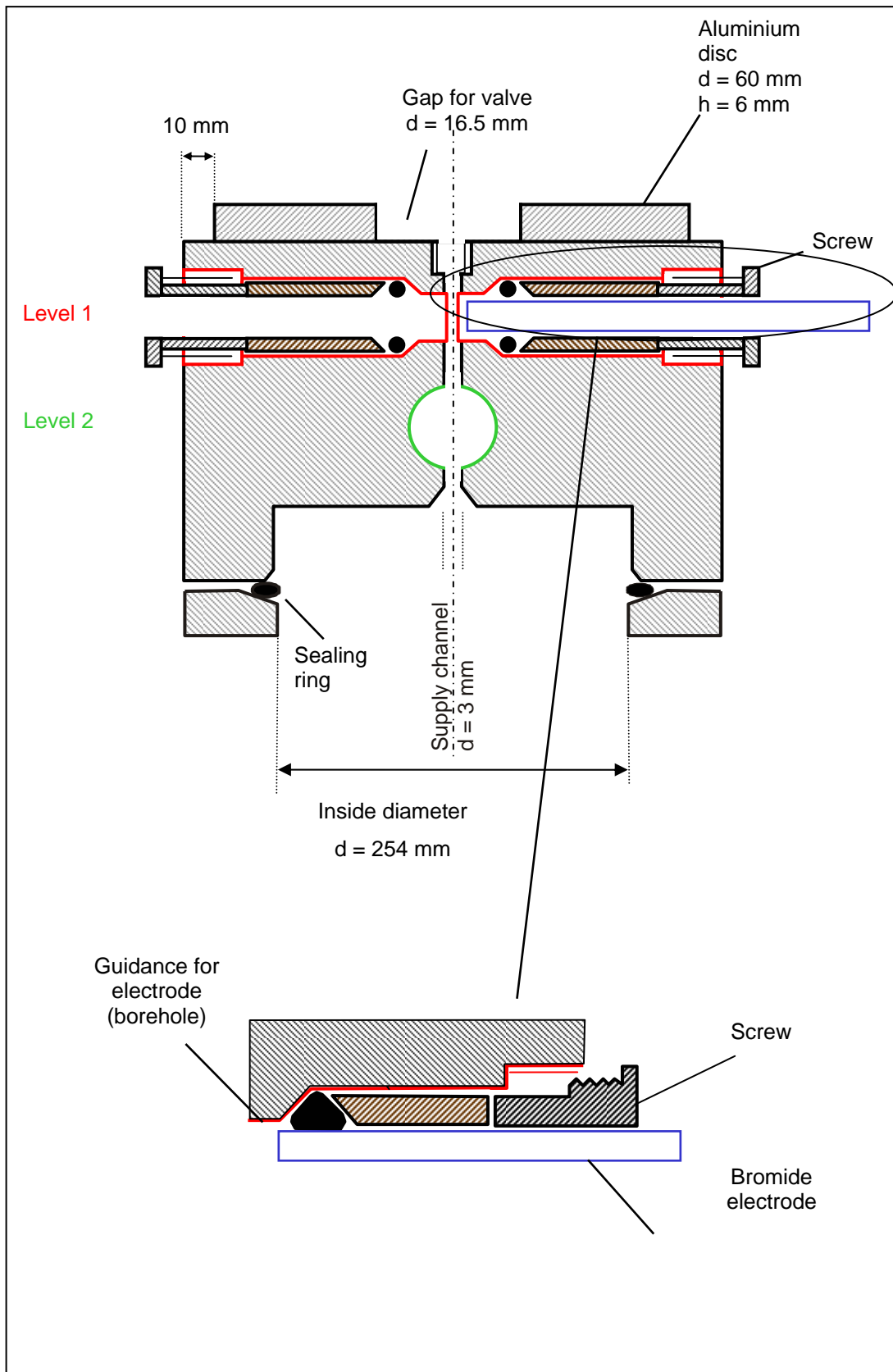
$$U = d_{60}/d_{10} = 1.94$$

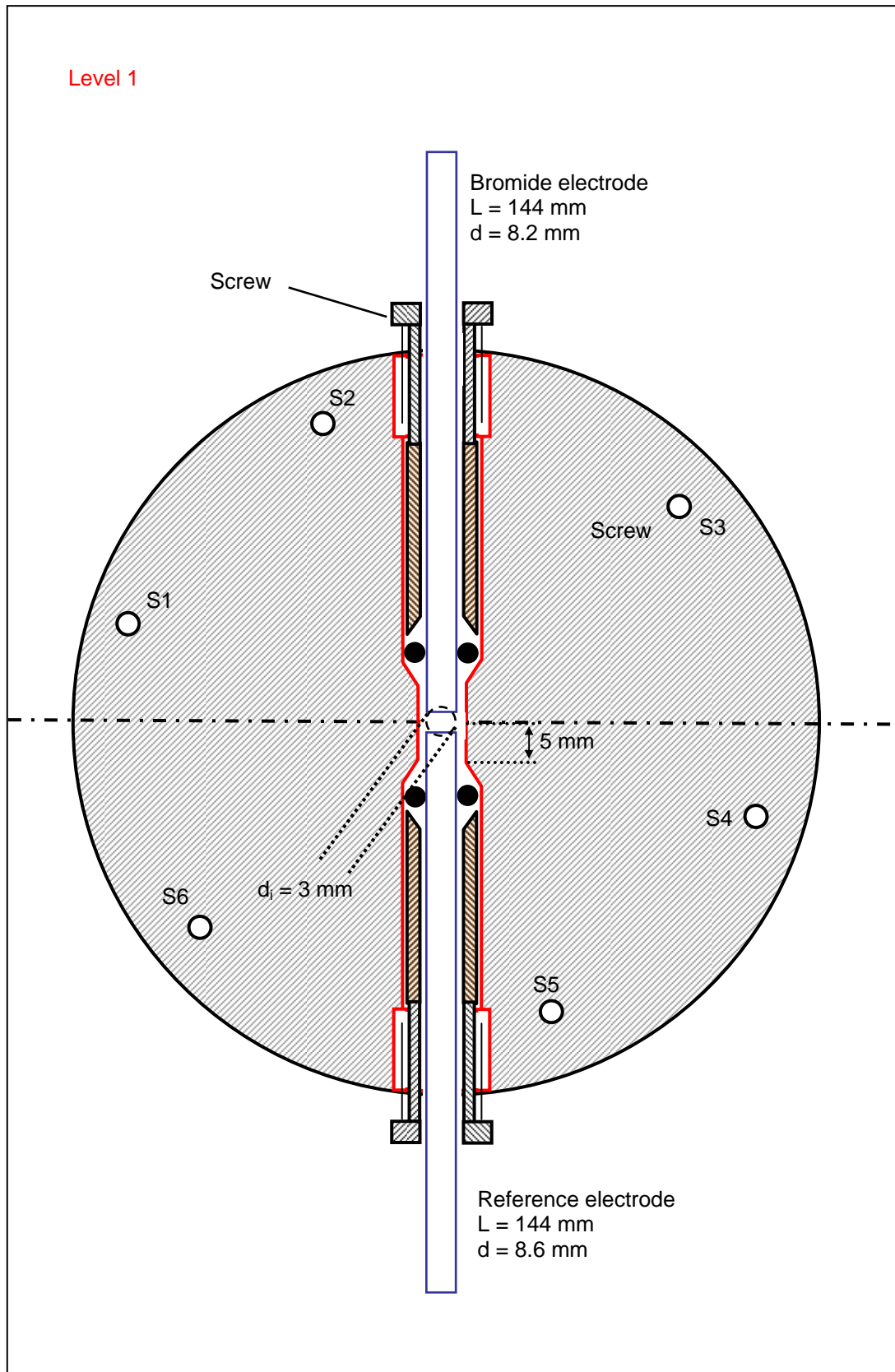
$$K_f = C_H \cdot d_{10}^2 = 3.75 \cdot 10^{-4} \text{ m/s}$$

$$C_H = (0.7 + 0.03 \cdot T)/86.4 = 0.0116 \quad (\text{for an aquifer typical temperature of } 10 \text{ }^\circ\text{C})$$

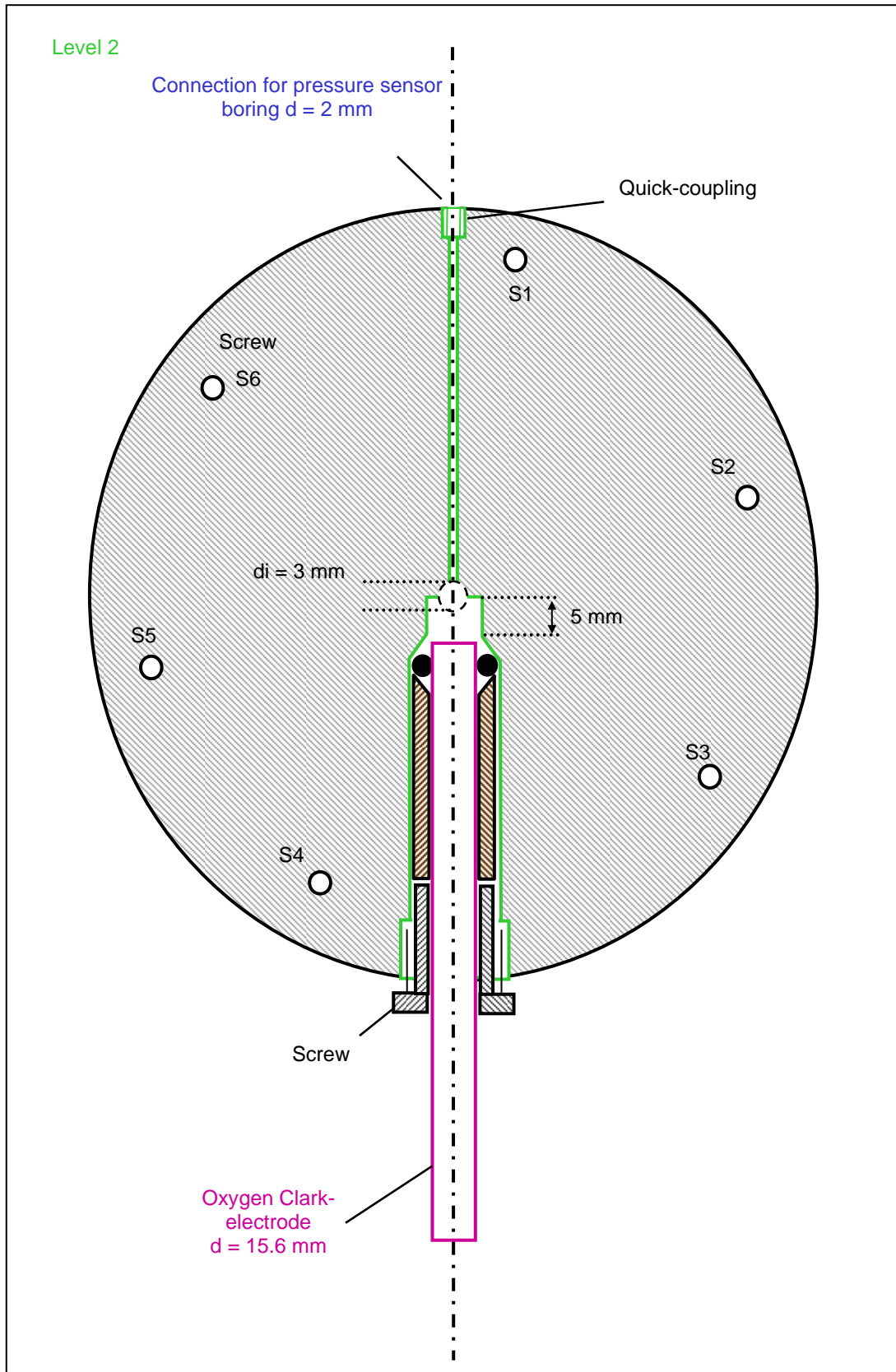
Appendix 3: Drawings of the Column Cap

Appendix 3.1: Drawing of the Column Cap, Sectional View (Front)



Appendix 3.2: Drawing of the Column Cap, Sectional View (Top, Cutting Plane Level 1)

Appendix 3.3: Drawing of the Column Cap, Sectional View (Top, Cutting Plane Level 2)



Appendix 4: Error Analysis for the Calculation of the Maximum Residual Gas Saturation

The error analysis for the calculation of the maximum residual gas saturation is displayed for experiment 3 exemplarily using the error propagation method according to Gauss. The experimental maximum gas saturations were computed by two independent methods: from gravimetric measurements and from bromide tracer tests. To allow a direct comparison of the uncertainties of the gas saturation determined by the two different methods, the standard deviations are shown as relative errors in the following.

Gravimetrically Determined Maximum Residual Gas Saturation

The gravimetric measurements of the gas volume were used to determine the maximum residual gas saturation in the column at the end of the gas injection for each experiment using the following equation:

$$S_g^{\max} = \frac{V_g^{\max}}{V_{p,\text{tot}}}, \quad (\text{A4})$$

where V_g^{\max} [cm³] is the average maximum residual gas volume in the column determined directly over the gravimetric measurements. $V_{p,\text{tot}}$ [cm³] is the total pore volume, which was computed from the total porosity ϕ_{tot} and the column volume V_{col} (determined after the experiments via weighting) by:

$$V_{p,\text{tot}} = V_{\text{col}} \cdot \phi_{\text{tot}}. \quad (\text{A5})$$

Measured average maximum residual gas volume V_g^{\max} :	9.8 cm ³
Standard deviation V_g^{\max} :	2.6 %
Measured column volume V_{col} :	338.95 cm ³
Standard deviation V_{col} :	0.15 %
Total porosity ϕ_{tot} (calculated from column dimensions):	0.376
Standard deviation ϕ_{tot} :	0.8 %
Calculated total pore volume $V_{p,\text{tot}}$:	127.45 cm ³
Calculated standard deviation $V_{p,\text{tot}}$:	0.94 %
Gravimetrically determined maximum residual gas saturation S_g^{\max} :	0.077
Calculated standard deviation S_g^{\max} :	3.9 %

Maximum Residual Gas Saturation Determined by Bromide Tracer Tests

Since the flow field inside the column can be considered as being very homogeneous, immobile water phases can be neglected. Consequently, the effective porosity ϕ_{eff} determined by the bromide tracer tests describes the fractional volume of water filled pore space and gives information about the particular gas phase content. By a bromide tracer test conducted at the time when the column exhibits the maximum residual gas saturation, the minimal effective porosity $\phi_{\text{eff}}^{\text{min}}$ can be determined and the maximum volumetric gas content θ_g^{max} can be computed by:

$$\theta_g^{\text{max}} = \phi_{\text{eff}}^{\text{max}} - \phi_{\text{eff}}^{\text{min}} . \quad (\text{A6})$$

The maximum effective porosity $\phi_{\text{eff}}^{\text{max}}$ can be determined by the bromide tracer test performed at complete water saturation. From the maximum volumetric gas content the maximum residual gas volume V_g^{max} in the column can be calculated by the following equation:

$$V_g^{\text{max}} = \theta_g^{\text{max}} \cdot V_{\text{col}} . \quad (\text{A7})$$

Then the gas saturation S_g can be calculated using Equation (A4). Thereby, the total pore volume $V_{p,\text{tot}}$ was calculated for each experiment using maximum effective porosity $\phi_{\text{eff}}^{\text{max}}$ determined by bromide tracer tests:

$$V_{p,\text{tot}} = V_{\text{col}} \cdot \phi_{\text{eff}}^{\text{max}} . \quad (\text{A8})$$

Maximum effective porosity $\phi_{\text{eff}}^{\text{max}}$ determined by Br-tracer test:	0.372
Standard deviation $\phi_{\text{eff}}^{\text{max}}$:	0.8 %
Minimum effective porosity $\phi_{\text{eff}}^{\text{min}}$ determined by Br-tracer test:	0.337
Standard deviation $\phi_{\text{eff}}^{\text{min}}$:	0.6 %
Calculated maximum gas phase content θ_g^{max} :	0.035
Calculated standard deviation θ_g^{max} :	14.3 %
Measured column volume V_{col} :	338.95 cm ³
Standard deviation V_{col} :	0.15 %
Calculated maximum residual gas volume V_g^{max} :	11.86 cm ³
Calculated standard deviation V_g^{max} :	14.4 %
Calculated total pore volume $V_{p,\text{tot}}$:	126.09 cm ³
Calculated standard deviation $V_{p,\text{tot}}$:	0.95 %
Maximum residual gas saturation S_g^{max} determined by Br-tracer test:	0.094
Calculated standard deviation S_g^{max} :	14.9 %

In general, the standard deviations for the gas saturations determined by gravimetric measurements are smaller than the standard deviations for the gas saturations determined by bromide tracer tests. This is due to the fact that both parameters determining the maximum gas saturation could not be measured directly via the bromide tracer tests. For the bromide tracer tests the error propagation for the gas saturation is governed by the larger value of the associated standard deviation of the maximum gas phase content.

Appendix 5: Oxygen Measurements

Appendix 5.1: Determination of the Oxygen Concentration Using a Modified Stern-Volmer Equation (after FIBOX Instruction Manual, PreSens GmbH)

The Stern-Volmer equation displays a linear correlation between $\tan\Phi_0/\tan\Phi$ or τ_0/τ and the oxygen concentration $[O_2]$:

$$\frac{\tan \Phi_0}{\tan \Phi} = \frac{\tau_{1,0}}{\tau_1} = 1 + K_{SV} \cdot [O_2]. \quad (A9)$$

- Φ_0 phase angle of oxygen-free water
- Φ measured phase angle
- $\tau_{1,0}$ luminescence decay time of oxygen-free water
- τ_1 measured luminescence decay time
- K_{SV} Stern-Volmer constant
- $[O_2]$ oxygen content in %-air-saturation

The Stern-Volmer plots of the optode show a distinct non-linearity in their response behaviour. This non-linear response behaviour can be described with a modified Stern-Volmer equation:

$$\frac{\tan \Phi_0}{\tan \Phi} = \left(\frac{f_1}{1 + K_{SV1} \cdot [O_2]} + \frac{1 - f_1}{1 + K_{SV2} \cdot [O_2]} \right)^{-1}. \quad (A10)$$

This model is based on the assumption that the indicator is distributed in the polymer matrix at two different sites and each fraction (f_1 , $1-f_1$) shows a different quenching constant (K_{SV1} , K_{SV2}). For practical use this model is not very convenient since it has too many parameters which have to be calibrated. Therefore, a simplified model based on equation 2 can be used. In this model, K_{SV2} is set to be $x \cdot K_{SV1}$. f_1 was determined to be 0.808 and x was determined to be $1/29.87$. The correlation coefficient R^2 of this fit was higher than 0.9999.

$$\frac{\tan \Phi_0}{\tan \Phi} = \left(\frac{0.808}{1 + K_{SV1} \cdot [O_2]} + \frac{0.192}{1 + \frac{1}{29.87} \cdot K_{SV1} \cdot [O_2]} \right)^{-1} \quad (A11)$$

The oxygen content in %-air-saturation can be calculated according to Equation (A12):

$$[\text{O}_2] = \frac{-B + \sqrt{B^2 - 4 \cdot A \cdot C}}{2 \cdot A}, \quad (\text{A12})$$

with the coefficients:

$$A = \frac{\tan \Phi}{\tan \Phi_0} \cdot x \cdot K_{\text{SV}}^2, \quad (\text{A13})$$

$$B = \frac{\tan \Phi}{\tan \Phi_0} \cdot K_{\text{SV}} + \frac{\tan \Phi}{\tan \Phi_0} \cdot x \cdot K_{\text{SV}} - f_1 \cdot x \cdot K_{\text{SV}} - K_{\text{SV}} + f_1 \cdot K_{\text{SV}}, \quad (\text{A14})$$

$$C = \frac{\tan \Phi}{\tan \Phi_0} - 1. \quad (\text{A15})$$

Appendix 5.2: Calibration of the Oxygen Sensor (Optode) (Exemplarily for Exp. 3)

The calibration of the optode was performed in the flow-through cell with the help of a calibration assistant of the Fibox software and the calibration curve calculated internally in the Fibox oxygen meter. A conventional two-point calibration in oxygen-free water and air-saturated water had to be used. The oxygen-free water was prepared by using sodium dithionit ($\text{Na}_2\text{S}_2\text{O}_4$). The oxygen meter relates the measured phase angles to the oxygen content.

Two-Point Calibration

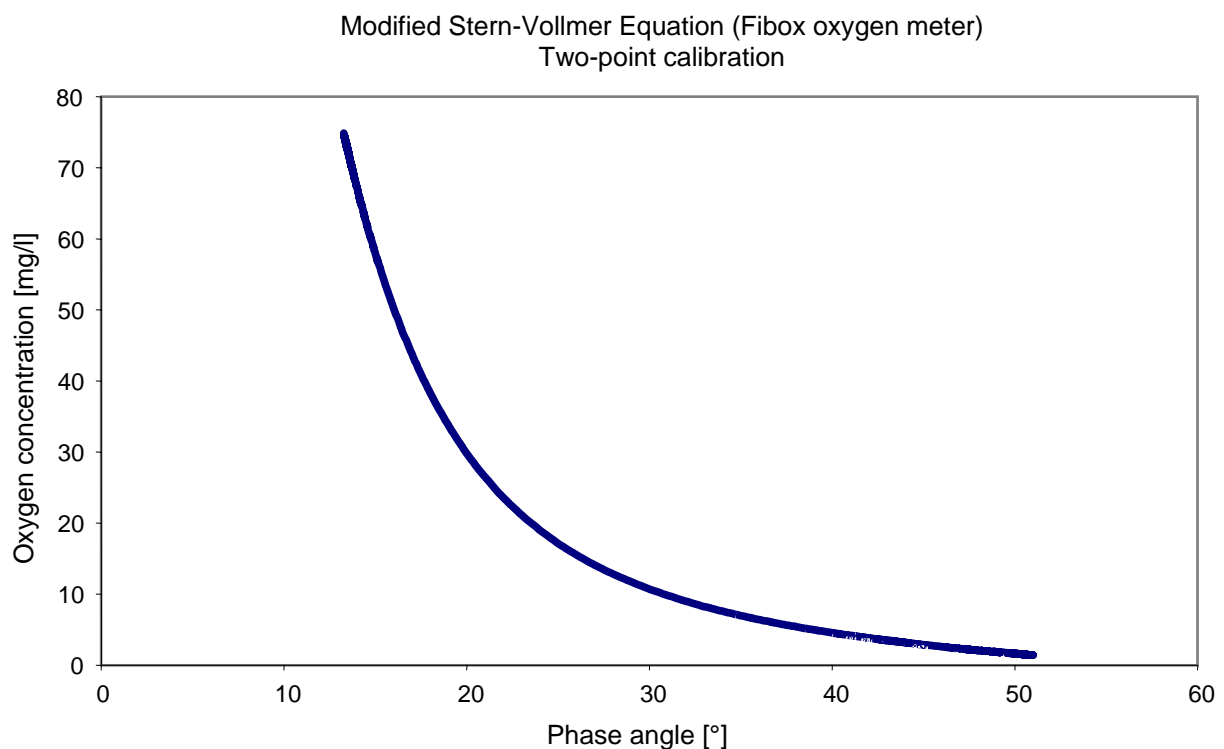
Calibration date: 2003-05-27

Temperature: 12°C Air pressure: 1024 mbar

Calibration value 1 (oxygen free water): phase angle = 58.99°

Calibration value 2 (air saturated water): phase angle = 29.34°

In the following figure the dissolved oxygen concentrations recorded at the column outlet during the dissolution of the injected oxygen gas phase (the actual dissolution experiment) is displayed against the measured phase angles exemplarily for experiment 3. The dissolved oxygen concentrations were calculated with the modified Stern-Volmer Equation implemented in the oxygen meter based on the two-point calibration.



The dissolved oxygen concentration achievable at atmospheric pressure at a temperature of 10 °C is approximately 55 mg/l (oxygen saturated water). Regarding the modified Stern-Volmer Equation implemented in the oxygen meter based on the two-point calibration, an oxygen concentration of 55 mg/l correlates to a phase angle of 15.37°.

Since concentrations at high oxygen levels were the sensitive area for the experiments, the optode was carefully re-calibrated for high concentrations. Therefore, a three-point calibration in oxygen-free, air-saturated and oxygen saturated water was performed with the sensor in the flow-through cell. For each experiment three calibration curves were recorded before the start of the dissolution experiment.

Three-Point Calibration

Calibration date: 2003-05-27

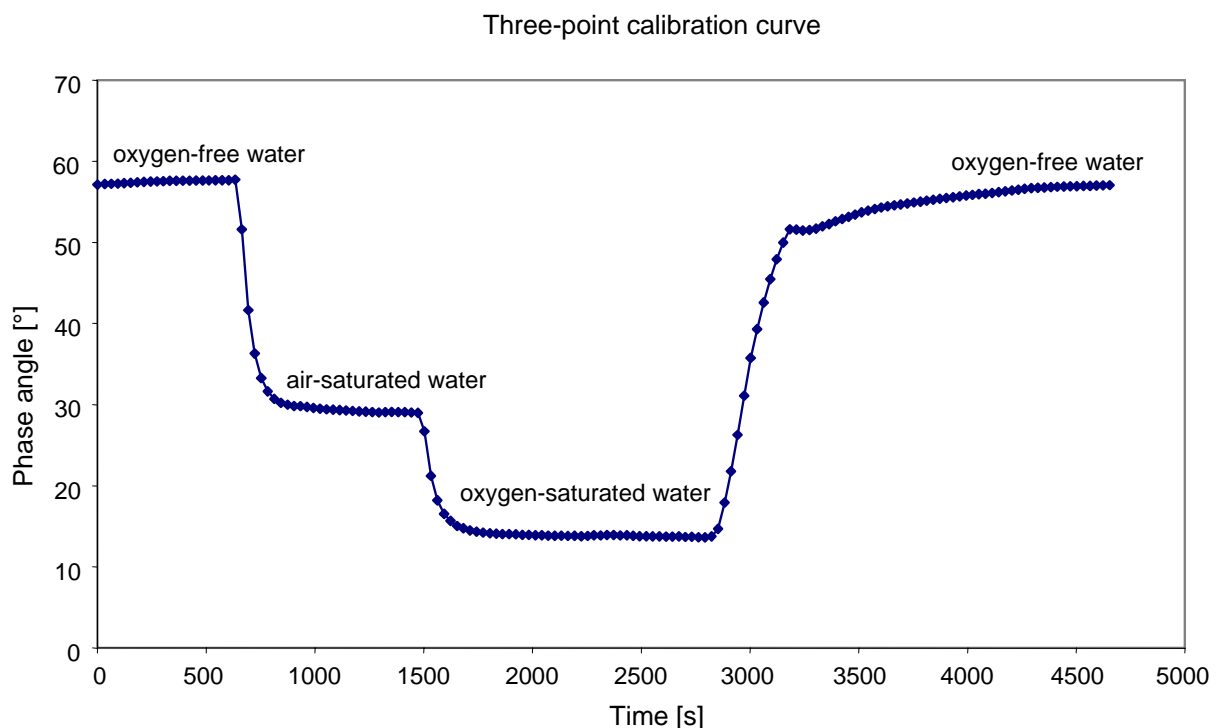
Temperature: 11°C Air pressure: 1023 mbar

Calibration value 1 (oxygen free water): phase angle = 57.7°

Calibration value 2 (air saturated water): phase angle = 29.04°

Calibration value 3 (oxygen saturated water): phase angle = 13.81°

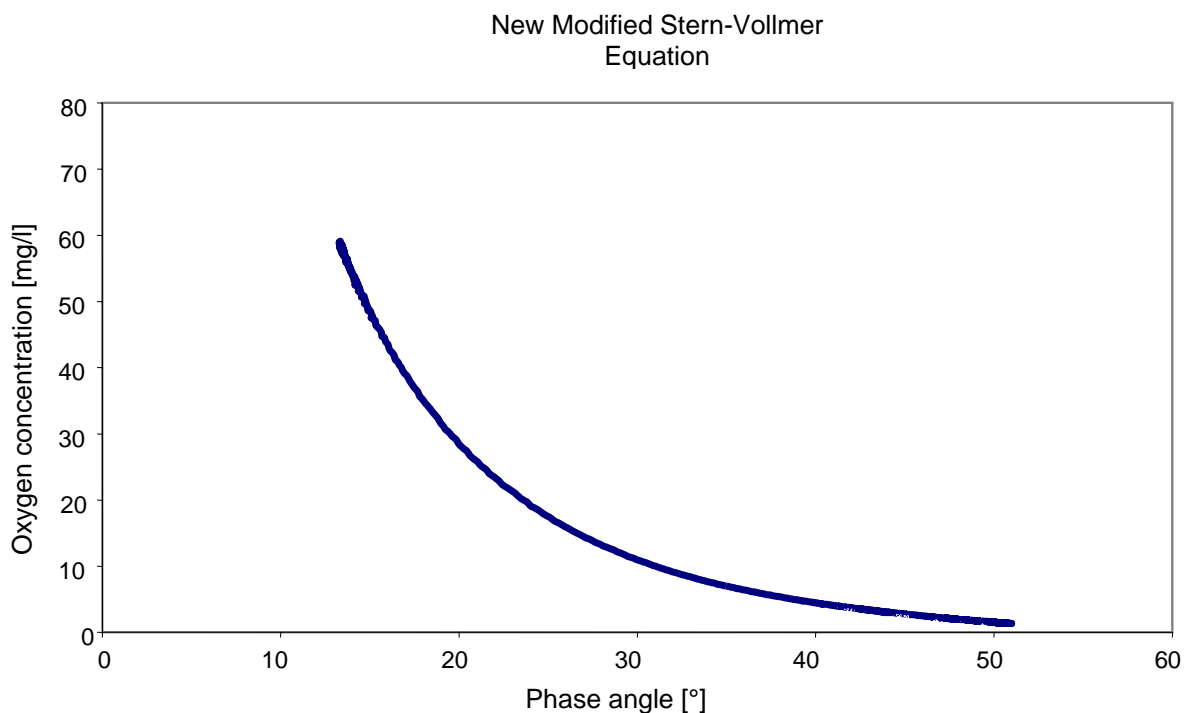
The following figure displays one of three calibration curves recorded for experiment 3.



The curve displays also a small memory effect of the optode. When switching from oxygen saturated water to oxygen free water, the measured phase angle needs a certain time to reach stable values. This is due to the fact that some oxygen was stored in the polymer of the flow through cell, which is slowly diffusing into the water delaying the time to reach the phase angles measured at oxygen free water.

Nevertheless, a new modified Stern-Volmer equation was determined with this three-point calibration and the phase angles measured during the experiments were correlated to the oxygen concentrations.

In the following figure the dissolved oxygen concentrations recorded at the column outlet during the dissolution of the injected oxygen gas phase (the actual dissolution experiment) is displayed against the measured phase angles exemplarily for experiment 3 again. This time, the dissolved oxygen concentrations were calculated with the new modified Stern-Volmer Equation based on the three-point calibration.



Regarding the new modified Stern-Volmer Equation based on the three-point calibration, an oxygen concentration of 55 mg/l correlates to a phase angle of 13.9°.

Error Analysis

To calculate the error of the optode measurements for the different Stern-Volmer Equations applied, the theoretical oxygen concentration achievable for the pressure at the column outlet and the temperature set for the experiment was calculated and compared to the measured oxygen concentration from the experiment (quasi steady state at the beginning of the dissolution experiment).

The error analysis is displayed for experiment 3 exemplarily:

Pressure at the column outlet:	108.7 kPa
Temperature:	11.2 °C
Theoretical oxygen concentration:	57.7 mg/l
Measured oxygen concentration (two-point calibration):	73.4 mg/l
Deviation at 100 % oxygen saturation (two-point calibration):	27 %
Measured oxygen concentration (three-point calibration):	58.1 mg/l
Deviation at 100 % oxygen saturation (three-point calibration):	0.7 %

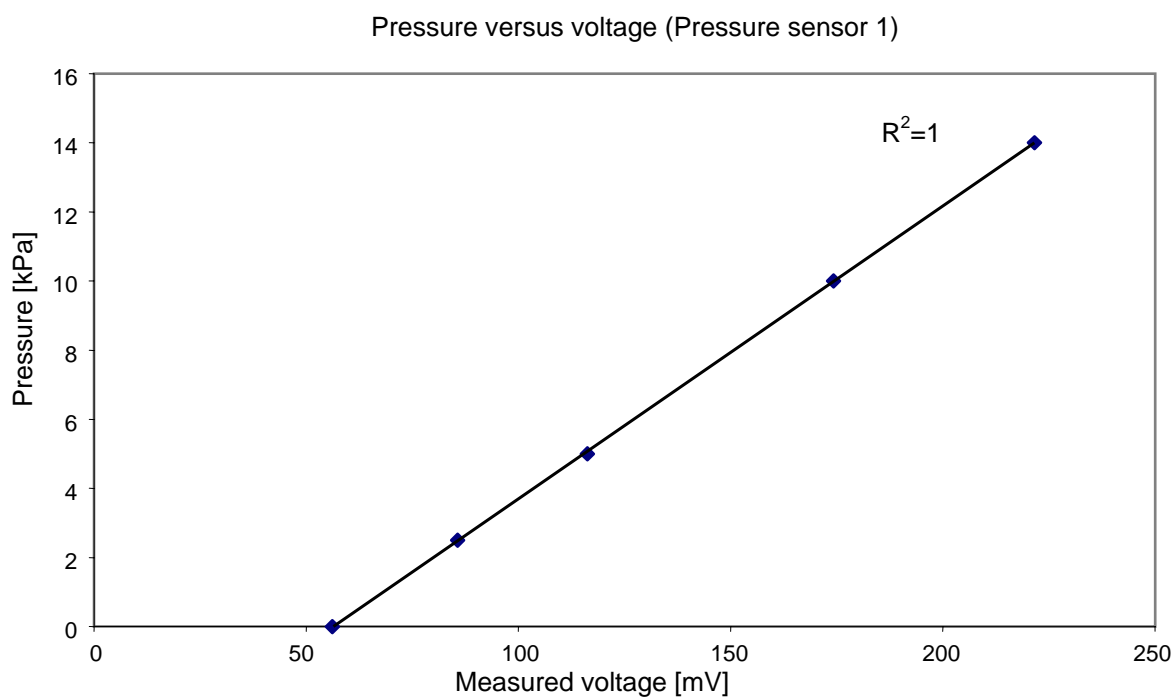
Appendix 6: Calibration of the Pressure Transducers (Exemplarily for Exp. 3)

The pressure transducers were calibrated before each experiment with the help of glass tube filled with water. The pressure transducer in the inlet of the column was calibrated at five different pressures; the pressure sensor in the outlet of the column was calibrated at four different pressures.

Pressure Sensor 1 (Column Inlet)

Calibration date: 2003-05-26

Pressure [cmH ₂ O]	Pressure [kPa]	Measurement 1 [mV]	Measurement 2 [mV]	Measurement 3 [mV]	Average value
0	0	57	56.7	54.9	56.2
25	2.5	86.4	85.1	85.7	85.73
50	5	115.7	117.7	115.3	116.23
100	10	174.5	173.5	174.7	174.23
140	14	222.3	221.9	220.6	221.6

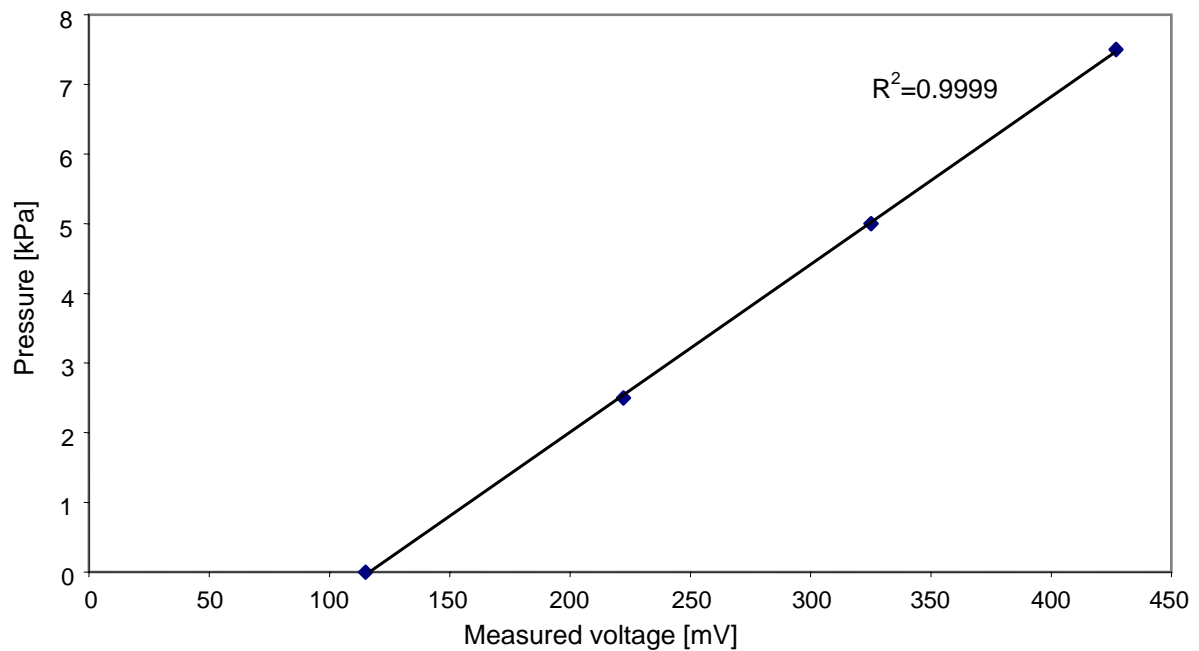


Pressure Sensor 2 (Column Outlet)

Calibration date: 2003-05-26

Pressure [cmH ₂ O]	Pressure [kPa]	Measurement 1 [mV]	Measurement 2 [mV]	Measurement 3 [mV]	Average value
0	0	113	113	119	115
25	2.5	220.6	225.1	220.8	222.17
50	5	321.8	328.3	325.3	325.13
75	7.5	427.8	425.3	427.7	426.93

Pressure versus voltage (Pressure sensor 2)



The water pressure measurements in the column in- and outlet were used to calculate the averaged hydraulic conductivity K_f before gas injection and during the dissolution of the gas phase.

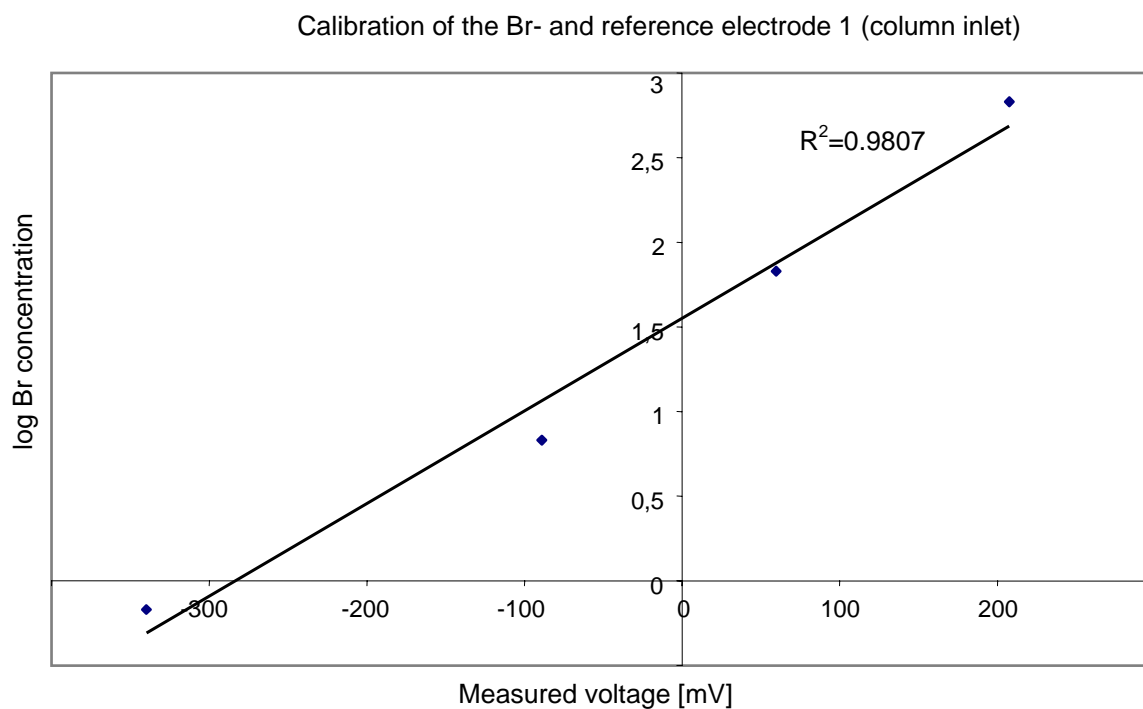
Appendix 7: Calibration of the Bromide Electrodes (Exemplarily for Exp. 3)

Before each experiment the bromide ion-selective electrodes and the reference electrodes were pre-conditioned by immersing them in 1000 ppm standard solution for approximately one day. Afterwards, the electrodes were attached in the column caps and a four-point calibration was conducted under flow conditions similar to that of the experiment.

Bromide Electrode 1 (Column Inlet)

Calibration date: 2003-05-28

Br concentration [mg/l]	Log Br concentration	Measurement 1 [mV]	Measurement 2 [mV]	Average value
671.5	2.83	208.65	206.56	207.61
67.15	1.83	54.2	65.12	59.66
6.72	0.83	-90.01	-87.9	-88.96
0.67	-0.17	-334.94	-344.51	-339.73

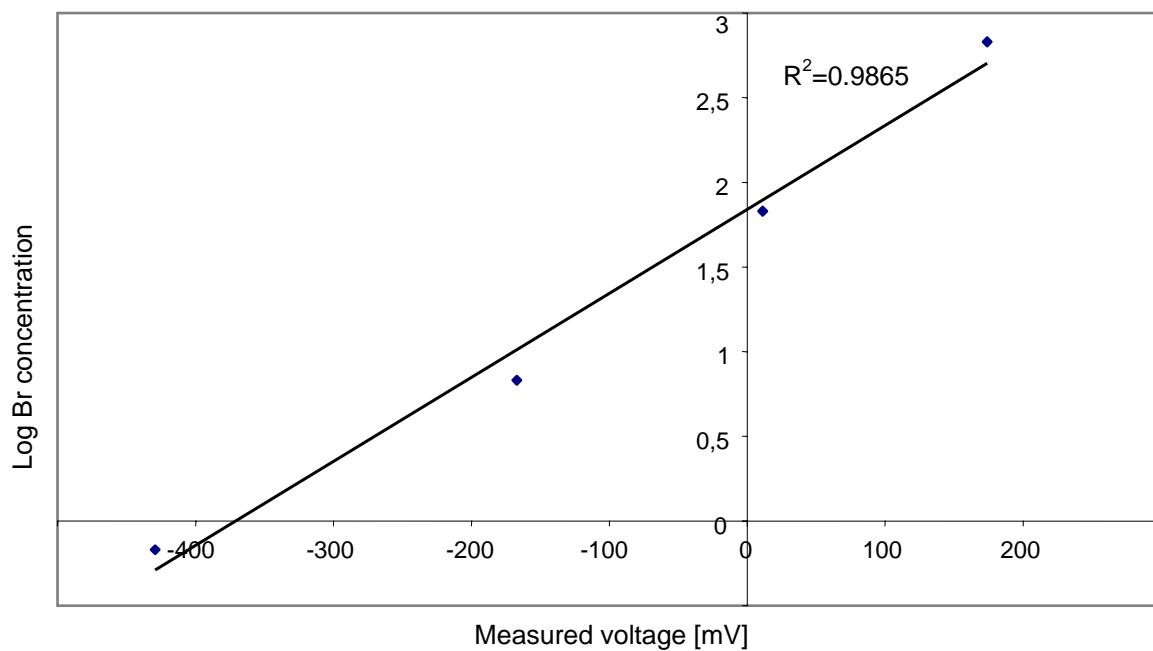


Bromide Electrode 2 (Column Outlet)

Calibration date: 2003-05-28

Br concentration [mg/l]	Log Br concentration	Measurement 1 [mV]	Measurement 2 [mV]	Average value
671.5	2.83	174.52	173.68	174.1
67.15	1.83	0.73	21.9	11.32
6.72	0.83	-168.58	-165.42	-167
0.67	-0.17	-422.86	-435.62	-429.24

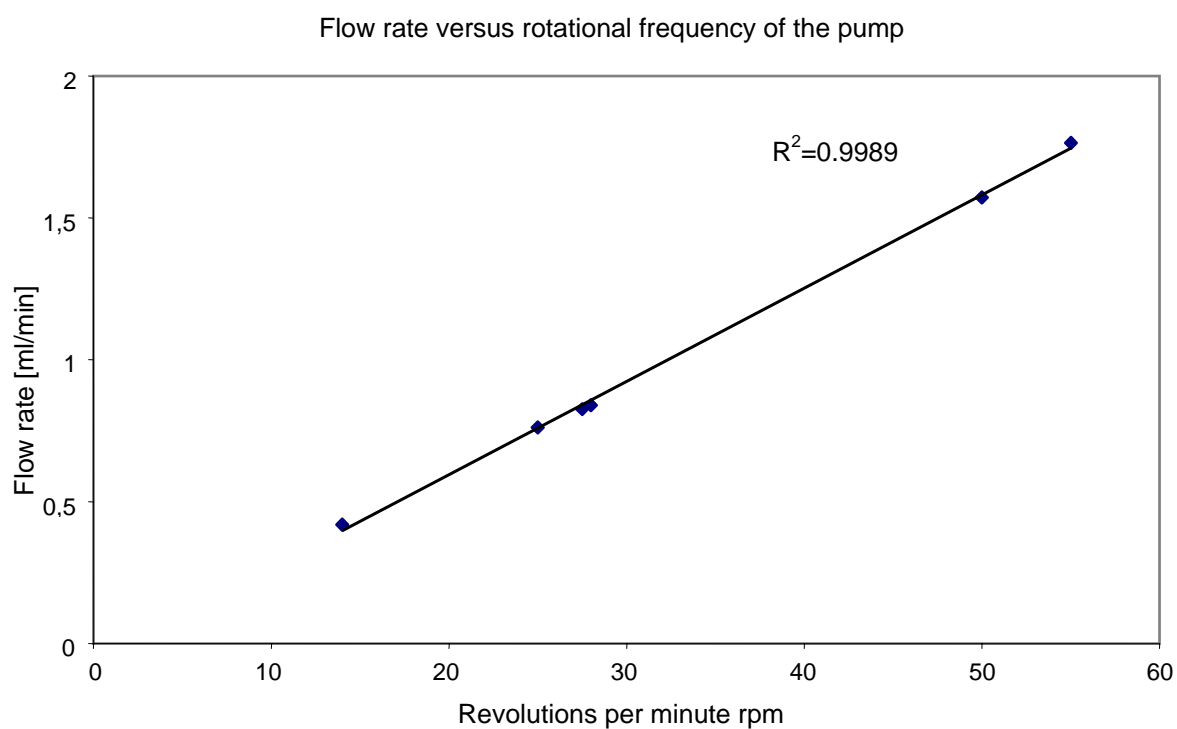
Calibration of the Br- and reference electrode 2 (column outlet)



Appendix 8: Calibration of the Four-Channel Peristaltic Pump

During the experiments the test solutions were pumped into the column with the help of a four-channel peristaltic pump with gastight Viton tubes (inner diameter = 1.65 mm). In the forefront of the experiments a calibration curve was plotted to test the linearity of the flow rate relating to the rotational frequency of the pump.

Flow rate [ml/min]	rpm
0.419	14
0.762	25
0.826	27.5
0.840	28
1.572	50
1.764	55



Lebenslauf

Persönliche Angaben

Name: Beckmann
Vorname: Annika
Geburtsdatum: 14.01.1974
Geburtsort: Walsrode
Familienstand: ledig

Bildungsweg und wissenschaftlicher Werdegang

1980 – 1982 Grundschule Walsrode
1982 – 1984 Grundschule Hodenhagen
1984 – 1986 Orientierungsstufe Hodenhagen
1986 – 1993 Gymnasium Walsrode
05/1993 Abitur
05/1993 – 09/1993 angestellt bei der Stadt Fallingb. bostel
1994 – 2000 Studium der Geologie/Paläontologie an der Universität Hannover

03/2000 Diplom
Diplom-Kartierung: “Geologische Kartierung der nordwestlichen Umgebung der Stadt Zacatecas (Zacatecas, Mexiko)”
Diplomarbeit: “Beitrag zur Tektonik und Metamorphose der triassischen Zacatecas-Gruppe (Zacatecas, Mexiko)”
2000 – 2004 Promotionsstelle am Department Hydrogeologie in Halle/Saale, UFZ-Umweltforschungszentrum Leipzig-Halle

Seit 08/2004 angestellt bei der Firma Biopract GmbH, Berlin, im Rahmen eines vom Bundesministerium für Wirtschaft und Arbeit (BMWA) geförderten Forschungsprojektes zur Entwicklung und den Einsatz einer modellgestützten Feedback Steuerung für die Errichtung von modularen in situ Gasinjektionssystemen (OXYWALL)

Versicherung

Hiermit versichere ich, dass ich die vorliegende Arbeit ohne unzulässige Hilfe Dritter und ohne Benutzung anderer als der angegebenen Hilfsmittel angefertigt habe; die aus fremden Quellen direkt oder indirekt übernommenen Gedanken sind als solche kenntlich gemacht.

Bei der Auswahl und Auswertung des Materials sowie bei der Herstellung des Manuskripts habe ich Unterstützungsleistungen von folgenden Personen erhalten:

Prof. Dr. H. Geistlinger

Prof. Dr. B. Merkel

Weitere Personen waren an der Abfassung der vorliegenden Arbeit nicht beteiligt. Die Hilfe eines Promotionsberaters habe ich nicht in Anspruch genommen. Weitere Personen haben von mir keine geldwerten Leistungen für Arbeiten erhalten, die nicht als solche kenntlich gemacht worden sind.

Die Arbeit wurde bisher weder im Inland noch im Ausland in gleicher oder ähnlicher Form einer anderen Prüfungsbehörde vorgelegt.

Annika Beckmann

Halle, 31.08.2005

